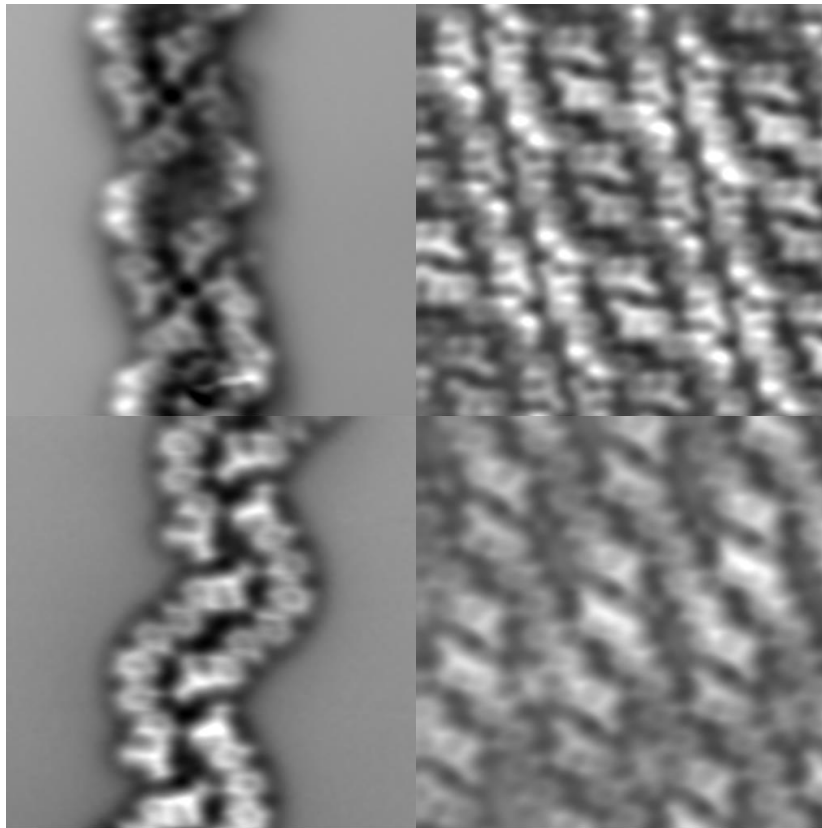# Structural and Electronic Properties of Thiophene-based Supramolecular Architectures on Metal Surfaces

A Combined STM and AFM Study

Doctoral Thesis

Zechao Yang

Structural and Electronic Properties of Thiophene-based Supramolecular Architectures on Metal Surfaces

A Combined STM and AFM Study

Doctoral Thesis

of

Zechao Yang

submitted to the
Department of Physics
of the
Freie Universität Berlin

10.09.2014

Diese Arbeit entstand in der Arbeitsgruppe von Prof. Dr. José Ignacio Pascual am Fachbereich Physik der Freien Universität Berlin.

Berlin, 10.09.2014

Erstgutachter: Prof. Dr. José Ignacio Pascual
Zweitgutachter: Prof. Dr. Wolfgang Kuch

Datum der Disputation: 31.10.2014

Kurzfassung

Die Funktionalität von organischen Schichten auf Metalloberflächen ist bestimmt von intermolekularen Wechselwirkungen und jenen zwischen Molekül und Oberfläche. In metallorganischen Strukturen sorgt die Metall-Liganden Hybridisierung für eine starke Modifizierung der Eigenschaften gegenüber dem freien Molekül. Diese Arbeit befasst sich mit dem Einfluss dieser Wechselwirkungen auf die Bildung von selbst-organisierenden Molekülstrukturen und die elektronischen Eigenschaften der resultierenden Nanostrukturen.

Unter Verwendung von Rastertunnel- und Rasterkraftmikroskopie (engl. STM und AFM) haben wir methyl-substituiertes Dicyanovinyl-quinquethiophene (DCV5T-Me$_2$) und Dicyanovinyl-hexathiophene (DCV6T) auf Au(111), Ag(111) und Cu(111) untersucht. Das Interesse an diesen Molekülen ist auf ihre potentielle Anwendung als hocheffiziente Photoabsorber in der organischen Photovoltaik zurückzuführen. Die strukturellen und elektronischen Eigenschaften an den organisch/organisch und organisch/metallischen Übergangsstellen werden hierbei mit sub-molekularer Auflösung untersucht.

Die Selbstorganisation von DCV5T-Me$_2$ auf Au(111) bei sub-Monolagen Bedeckung führt zu zwei verschiedenen koexistenten Strukturen: organische Inseln und metallorganische Ketten. Die Formation der ersteren ist bestimmt von intermolekularen Wasserstoffbrückenbindungen und elektrostatischen Wechselwirkungen, die zu einer Absenkung der unbesetzten molekularen Energieniveaus, bezogen auf einzelne Moleküle auf Au(111), führen. Die Ketten werden durch CN/Au-Adatom Koordination stabilisiert und deren Einfluss auf die molekularen Zustände zeigt sich als ortsspezifisch. Das ursprüngliche am niedrigsten unbesetzten Molekülorbital (LUMO) und das LUMO+1 hybridisieren durch eine Linearkombination molekularer Orbitale bei jenen Molekülen, die nur an ein Au Atom koordinieren und es kommt zu einer Neuordnung der unbesetzten Molekülorbitale. Weiterhin ordnet sich DCV5T-Me$_2$ mit steigender Bedeckung in der zweiten molekularen Monolage so an, wie in den einlagigen Inseln und ist dadurch entkoppelt vom Metallsubstrat. Dabei kann ein Vibrationszustand mit einer Energie von 180 mV beobachtet werden, der einer Streckmode der Kohlenstoff-Bindungen entspricht.

Um eine homogene Hybridstruktur zu erhalten wurde DCV5T-Me$_2$ mit anderen Stoffen zusammen auf die Au(111) Oberfläche gebracht. Durch gleichzeitiges Aufbringen von DCV5T-Me$_2$ und NaCl formten sich Ketten, stabilisiert durch Na-CN Bindungen und geprägt durch langreichweitige Coulomb-Abstoßung zwischen den Ketten. Im Gegenzug dazu bildete DCV5T-Me$_2$ mit anderen untersuchten Molekülen (C60, Coronen und TCNQ) aufgrund der starken intermolekularen Wechselwirkungen zwischen den DCV5T-Me$_2$ Molekülen und der Koordination zu Au-Adatomen keine geordneten Hybridstrukturen.

Auch in Abhängigkeit vom verwendeten Substrat verändern sich die Eigenschaften von DCV5T-Me$_2$. Eine starre Absenkung der unbesetzten Orbitale wird aufgrund der kleineren Austrittsarbeit beim Wechsel auf ein Ag(111) Substrat beobachtet. Auf Cu(111) dagegen sorgt die stärkere Wechselwirkung zwischen Molekül und Oberfläche zu einer Eliminierung der molekularen Zustände an der Grenzfläche.

DCV6T zeigt aufgrund seiner hohen intramolekularen Flexibilität andere Eigenschaften als DCV5T-Me$_2$. Zusätzlich zur Formation von Au/DCV6T Ketten und organischen Inseln bilden sich auf Au(111) selbst-geordnete, rein organische Ketten. Die Anordnung der Moleküle in organischen Inseln ist hierbei die energetisch günstigste Konfiguration. Die Bildung von organischen Ketten ist aufgrund der intermolekularen Wechselwirkungen weniger günstig, wie es auch in der "Induced-fit therory" beschrieben wird. Gleichzeitiges Aufbringen von Co Atomen mit DCV6T auf Au(111) sorgt für die Entstehung von metallorganischen Ketten. Die Co-CN Koordination kann durch zwei energetisch tieferliegende Zustände bei positiver Spannung identifiziert werden, jedoch. Durch andere Hybridisierungsmechanismen weisen diese Co-koordinierten Moleküle jedoch eine von den Au-CN bindenden Molekülen abweichende elektronische Struktur auf.

Abstract

The functionality of organic layers on metal substrates is determined by intermolecular and molecule-surface interactions. In a metal-organic complex, the metal-ligand hybridization induces drastic modification to the free molecular features. This thesis deals with the role these interactions play in the formation of molecular assemblies and the evolution of electronic properties in the resulting nanostructures.

By using combined scanning tunneling microscopy (STM) and atomic force microscopy (AFM), we have investigated methyl-substituted dicyanovinyl-quinquethiophenes (DCV5T-Me_2) and dicyanovinyl-hexathiophenes (DCV6T), on Au(111), Ag(111) and Cu(111). The interest in these molecules stems from their potential use as highly efficient photoabsorbers in organic photovoltaics. Structural and electronic properties at their organic/organic and organic/metal interfaces are characterized with sub-molecular resolution.

Self-assembly of DCV5T-Me_2 on Au(111) at sub-monolayer coverage results in two different structures simultaneously: organic islands and metal-organic chains. The organic islands are formed by intermolecular hydrogen bonding and electrostatic interaction that rigidly shift down the energy level of unoccupied states with respect to the single molecules on the metal surface. The chains are stabilized by CN/Au-adatom coordination, whose influence on the molecular states is site-specific. In particular, the original lowest unoccupied molecular orbital (LUMO) and LUMO+1 mix by linear combination at the molecule coordinated to only one Au atom at one side, which leads to a redistribution of the unoccupied orbitals compared with the free molecular orbital structure. With increase of the coverage, DCV5T-Me_2 packs in a similar way in the second layer with that in the organic islands and is decoupled from the metal substrate. There, a vibrational state with energy of 180 mV is observed, corresponding to carbon bonds stretching.

To fabricate a homogenous hybrid structure, DCV5T-Me_2 is co-deposited onto Au(111) with other components. After co-deposition of NaCl and DCV5T-Me_2, chains with Na-CN bonds are formed, mediated by a long-range inter-chain Coulomb repulsion. In contrast, co-deposition of DCV5T-Me_2 and other types of molecules (C_{60}, coronene and TCNQ) can not result in ordered hybrid systems, inhibited by strong intermolecular interactions and coordination between cyano groups and Au adatoms.

Properties of DCV5T-Me_2 evolve with the change of substrates. A rigid energetic downshift of unoccupied orbitals on Ag(111) with respect to on Au(111) is induced by the lower work function of Ag(111). Differently, DCV5T-Me_2 chemically adsorbs on Cu(111) with strong molecule/surface hybridization that eliminates the molecular states at the interface.

DCV6T shows different assembly behaviors than DCV5T-Me_2 due to its larger flexibility. In addition to Au/DCV6T chains and organic islands, it also self-assembles into organic chains on Au(111). Molecules in organic islands adopt the energy minimum configuration. Whereas, organic chains include molecules with energetically unfavorable geometry, caused by intermolecular interactions and interpreted by the "induced fit theory". Co-deposition of Co atoms with DCV6T on Au(111) leads to chains with Co-CN coordination inducing states localized at the molecular end-groups. There molecules exhibit different electronic structures than those bonding with Au atoms due to different hybridization mechanism.

Contents

Introduction

Over the past decades, rapid progresses have been made in electronics based on inorganic semiconductors. However, limitations arise with the miniaturization of the size of devices. It is challenging to produce a volume of nanoscale devices by using traditional top-down methods [1]. On the other hand, a new door is open. Already at the early time of 1960, Richard Feynman envisioned the idea of *"arrange the atoms one by one the way we want them"* [2].

However, it is still time consuming for large scale fabrication by manipulating individual atoms. Instead, another bottom-up method, the self-assembly [3], can be used. In this approach, organic molecules can form extended and ordered nanostructures through intermolecular van der Waals forces [4], hydrogen-bonds [5] and even covalent bonds [6, 7]. Moreover, coordination bonding allows for combination of molecules with metal atoms in well-defined networks [8], which offers fascinating perspectives for electronic and magnetic devices [9].

The molecular self-assembly is usually facilitated by the lock-and-key effect [10, 11, 12], which is that designed lateral interactions guide the connection of functional groups without perturbation to molecular configuration [13]. It may be possible that the configuration of a flexible molecule changes when the molecular chemical environment is altered by intermolecular interactions [14], as in the induced fit effect [10, 11, 12]. A microscopic understanding of the molecular geometry upon assembly on surfaces is crucial for the design and application of organic electronics. Low temperature atomic force microscopy (LT-AFM) [15] is an ideal instrument for this purpose, which can resolve the molecular chemical structure with atomic resolution in real space [16, 17].

Electronic properties of molecules are influenced by the presence of their neighbors in the assembled structures. The interaction between molecules and substrates also has to be taken into account. Charge transfer [18] may occur between a donor molecule and an acceptor molecule, inducing a complete charge redistribution. In some systems, intermolecular interactions can cause an energetic realignment of molecular orbitals [19]. The hybridization of the metal surface with reactive molecular groups may enhance vertical charge transfer [20, 21, 22, 23], and induce conformational distortions [24, 25], leading to chemically new molecular species [26]. Even for weak interactions, the metal surface can induce dipolar perturbations to the molecular states [27, 28, 29]. The understanding of how molecular levels realign in the proximity of a metal surface is still under debate [30, 31]. Low temperature scanning

tunneling microscopy [32] (LT-STM) can be utilized to study the local electronic properties of molecules on conducting surfaces.

The ultimate goal of molecular electronics is to replace inorganic semiconductors with cheap and versatile organic molecules. The basic components of molecular electronic circuits are functional molecules serving as diodes [33], transistors [34] or switches [35] contacting with metal electrodes for application of bias voltage [36, 37]. The whole system can be built on an insulating film to reduce the influence from the metal surface [38]. However, the electronic coupling of the molecule to the metal electrodes is inevitable, which drastically disturbs the free molecule properties. It has been reported that the energy level alignment of localized and degenerated orbitals can be locally modified by lifting their degeneracies by step-wise metal atom attachment [39]. Recent works demonstrate that the overlapping of two orbitals from two connected molecules *via* a metal atom can be described by the model of a linear combination of molecule orbitals (LCMO) [40]. Whether the attachment of the bonding to a metal atom can trigger a similar orbital renormalization within an individual molecule is still unknown. The metal-organic contacts can be fabricated through STM manipulations [41]. Actually, the self-assembled metal-organic networks on inert metal surfaces directly resemble the real chemical environments of molecules in organic electronic circuits, where the metal-ligand coordination offers an ideal platform for the study of metal-molecule contact.

Molecules with an internal acceptor-donor-acceptor architecture, dicyanovinylene-substituted oligothiophenes (DCV5T-Me$_2$ and DCV6T), draw interest due to their potential use as photoabsorber in organic photovoltaics [42, 43, 44, 45, 46, 47, 48, 49]. These molecules are composed of a central oligothiophenes (nT) backbone with two terminal dicyanovinyl (DCV) groups linked symmetrically. The linkage within the same architecture of an electron donating unit has the goal of reducing the optical gap and, hence, increasing the solar photon absorption efficiency [50]. Their practical use in photovoltaic blends requires efficient charge dynamics, which is favored by the delocalized character of oligothiophene frontier orbitals and by crystal packing. However, the anisotropy of the packing structure [50], molecular distortions, and the reactivity of the DCV end-groups may facilitate the creation of charge traps that inhibit the charge transport.

In order to improve the performance of organic solar cells based on DCV5T-Me$_2$ and DCV6T, in this thesis, we study their structural and electronic properties at the organic/organic and organic/metal interfaces by using combined STM and AFM. The thesis is described in the following way:

In **chapter 1**, we show the details of the experimental setup and measured systems.

In **chapter 2**, we investigate the pure organic self-assemblies of DCV5T-Me$_2$ on the Au(111) surface. AFM is utilized to determine the bonding structure of molecular islands. Then, electronic properties of the islands are measured with STS and

compared with the isolated molecules to inspect the influence of intermolecular interactions on molecular states. The electronic coupling with the metal surface is significantly suppressed in the second layer of DCV5T-Me$_2$ on Au(111). There the vibronic states of molecules are identified.

In **chapter 3**, we focus on the complexes composed of DCV5T-Me$_2$ and metal atoms or another type of molecules on Au(111). DCV5T-Me$_2$ self-assembles into metal-organic chains by incorporation of Au adatoms, whose bonding structure is resolved by AFM in real space. Then, we characterize the orbital structure of molecules with different coordination geometry. A spatial redistribution of unoccupied orbitals at the one-side coordinated molecule is observed and interpreted with LCMO, while the two-side coordinated molecule only exhibits an orbital energy realignment. Metal-organic chains cementing with Na atoms are formed, when NaCl is co-deposited. We show that the growth of these chains is determined by a long-range repulsion. At the end of this chapter, trials to obtain hybrid molecular structures are presented.

In **chapter 4**, we examine the adsorption and assembly of DCV5T-Me$_2$ on two more reactive metal surfaces, the Ag(111) and Cu(111). There, the molecule exhibits different structural and electronic features with respect to on Au(111). In particular, quantum scattering and confinement of surface electrons by molecular structures are observed on Cu(111).

In **chapter 5**, we study DCV6T molecules on Au(111). In addition to metal-organic Au/DCV6T chains, two kinds of self-assembled organic structures, islands and chains, are formed with different molecular configuration, as imaged by AFM. The lock-and-key effect results in static molecular recognition and stabilization of molecules with the lowest energy structure within islands. In contrast, molecules within chains adopt an energetically unfavorable configuration caused by intermolecular interactions, which is interpreted with the induce fit theory. Then, the electronic properties of different types of DCV6T assemblies are investigated by STS. At the end of this chapter, structural and electronic properties of metal-organic chains composed of DCV6T and Co atoms are measured to inspect the influence of different species of metal atoms on the metal-ligand hybridization. Surprisingly, there the attachment of Co atoms to the ligand induces no influence to the unoccupied molecular states.

In **chapter 6**, we summarize the results presented in this thesis.

1 Theoretical and Experimental Techniques

1.1 Scanning Tunneling Microscopy

The invention of STM by G. Binning and H. Rohrer in 1981 [32, 51, 52] opens the way to study materials at nanoscale in real space. Its working principle is based on the quantum tunneling effect, which has been widely investigated since 1960s [53, 54]. As illustrated in figure 1.1 a, a very sharp metallic tip is approached to a metallic or semiconducting surface as close as a few angstroms to create a narrow potential barrier. Then a bias voltage is applied between the tip and surface, which induces a flow of tunneling current through the vacuum gap. Moreover, the tunneling current exponentially decays with the tip-surface distance z following the way: $I_{\mathrm{T}} \propto \exp(-A\varphi^{1/2}z)$, where A is a constant and φ is the work function. As a result, the distance can be controlled by the tunneling current with high sensitivity[1], which is realized through varying voltages applied to piezos carrying the tip. The controllable tunneling gap [51], combined with the concept of scanning achieved also via piezoelectric effect [32], brings the STM in reality.

There are two scanning modes to obtain topographic image of the surface: the constant current mode and constant height mode (figure 1.1 b). In constant current mode, the tunneling current is kept constant through adjusting the tip-sample distance with the feedback loop closed during scanning. Then the tip height signal at each scanning point results in a map of surface topography. In contrast, in the constant height mode the feedback loop is open and the tip scans over the surface without changing height. Accordingly, the variation of the tunneling current as a function of the tip lateral position represents the surface structure.

In addition to investigation of self-assembled structures, building artificial nano-architectures is also possible by using STM's manipulation function [41]. There are two manipulation modes, namely, the lateral manipulation and the vertical manipulation, as shown in figure 1.1 c. In the lateral manipulation mode, the tip is approached very close to the object, an atom for example, accompanied by the build of tip-atom attractive interactions (step A). Then the atom is moved over the surface following the movement of the tip due to the attractive forces (step B). When

---

[1]In general, the distance between the tip and the sample is around 5-10 Å and the tunneling current changes about one order of magnitude with the change of tip-sample distance of 1 Å.

the atom arrives at the destination, the tip is retracted with the break of tip-atom interactions leaving the atom at a different position on the surface (step C). The first step in vertical manipulation is the same as that in the lateral manipulation, which is building the tip-atom attractive interactions (step A). Afterwards, the tip is slowly retracted. If the tip-atom interactions dominate over the surface-atom interactions (step B), the atom can be vertically transferred to the tip (step C).
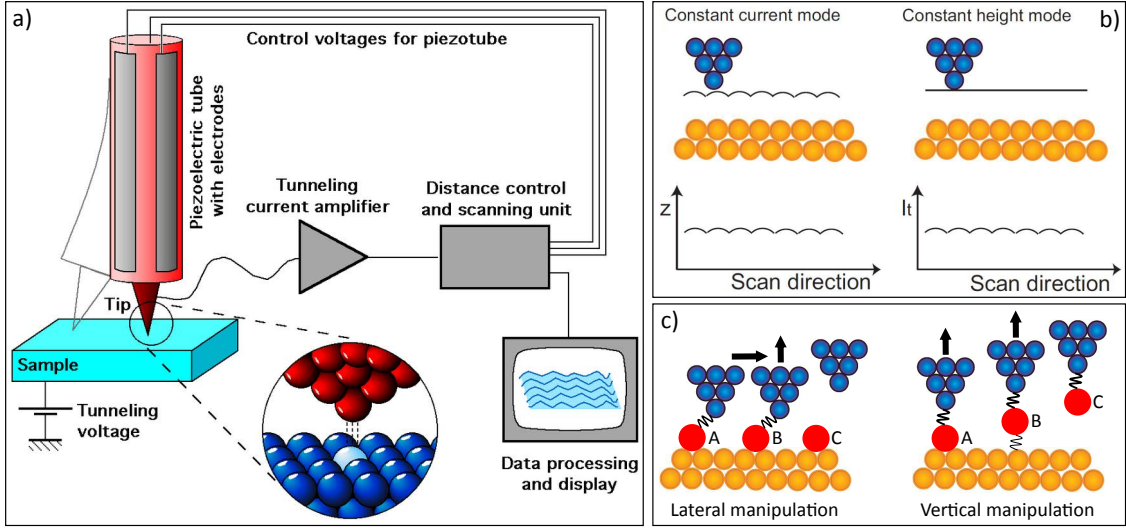
Figure 1.1: a) Scheme of the working mechanism of a STM [55]. b) Constant current and constant height scanning modes [56]. c) Lateral and vertical manipulation modes. The fold lines represent the tip-atom and surface-atom interactions, where their thickness stands for the interaction strength.

1.1.1 Theory of Scanning Tunneling Microscopy

In 1983, Tersoff and Hamann created the first quantitative model for the tunneling current in STM [57, 58]. They treated the tunneling junction as a locally spherical tip approached to a flat surface. By using a first-order perturbation theory, in the limit of low bias voltage and temperature the tunneling current can be expressed as:

$$I_{\mathrm{T}} = (2\pi/\hbar)\mathrm{e}^2 V \sum_{\mu\nu} |M_{\mu\nu}|^2 \delta(E_\nu - E_{\mathrm{F}})\delta(E_\mu - E_{\mathrm{F}}) \tag{1.1}$$

where $\hbar$ is the Dirac constant, e is the elementary charge, V is the applied voltage, E_ν is the energy of surface state ϕ_ν, E_μ is the energy of tip state ϕ_μ and E_{F} is the Fermi energy. According to Bardeen's transfer Hamiltonian approach [53], the tunneling matrix element, $M_{\mu\nu}$, is given by:

$$M_{\mu\nu} = -(\hbar^2/2m) \int d\vec{S}(\phi_\mu^* \nabla \phi_\nu - \phi_\nu \nabla \phi_\mu^*) \tag{1.2}$$

where m is the effective electron mass and the integral is over any surface lying entirely within the barrier region separating the two sides.

By assuming a spherical tip with asymptotic s-wave functions, Eq. 1.1 is simplified as:

$$I_\mathrm{T} = 32\pi^3\hbar^{-1}\mathrm{e}^2 V\varphi^2\rho_\mathrm{t}(E_\mathrm{F})R^2 k^{-4}e^{2kR}\sum_\nu |\phi_\nu(\vec{r_0})|^2\delta(E_\nu - E_\mathrm{F}) \qquad (1.3)$$

where φ is the work function of the tip and sample (we assume that they are the same), $\rho_\mathrm{t}(E_\mathrm{F})$ is the tip density of states per unit volume, R is the radius of curvature of the tip centered at $\vec{r_0}$ and $k = \hbar^{-1}(2m\varphi)^{1/2}$ is the inverse decay length of the wave functions in vacuum. In this expression, the integration term represents the density of states of the surface located at the position of the probe tip near Fermi energy. Therefore, the tunneling current is proportional to the local density of states of the surface if assuming that the tip state is constant.

However, above description is based on the assumption of low bias voltage (around 10 mV). In reality, higher voltages (typical $\pm$ 3 V) are applied to observe properties of organic molecules on the surface. Then a generalization of the Tersoff-Hamann tunneling current after considering the contribution of states in the finite voltage window is necessary. With the Wentzel–Kramers–Brillouin (WKB) approximation, at low temperature the tunneling current can be expressed as [59, 60]:

$$I_\mathrm{T} = (4\pi\mathrm{e}/\hbar)\int_{E_\mathrm{F}}^{E_\mathrm{F}+\mathrm{e}V}\rho_\mathrm{t}(E_\mathrm{F} - \mathrm{e}V)\rho_\mathrm{s}(E)|M_\mathrm{st}(E,V,z)|^2 dE \qquad (1.4)$$

Here, the tunneling current is represented by a simple convolution of the density of states of the tip ρ_t and the surface ρ_s using the tunneling probability $T(E,V,z) = |M_\mathrm{st}(E,V,z)|^2$. The tunneling probability is a function of the tip-surface distance, the energy and the bias voltage:

$$T(E,V,z) = exp\left[-\frac{2z\sqrt{2m}}{\hbar}\sqrt{\frac{\varphi_\mathrm{s} + \varphi_\mathrm{t}}{2} + \frac{\mathrm{e}V}{2} - E}\right] \qquad (1.5)$$

Usually, we assume that ρ_t and T are constant, inducing the tunneling current as the integration of the density of states of the sample in the energy window between E_F and $E_\mathrm{E} + \mathrm{e}V$.

1.1.2 Scanning Tunneling Spectroscopy

As illustrated in figure 1.1 a, the tunneling process is determined by three parameters: the tip-sample distance z, the bias voltage V and the tunneling current I, which is mathematically expressed in Eq. 1.4. Electronic properties of the sample can be derived from the spectroscopy by varying two of the three parameters with the third one fixed. If V is fixed, the local work function φ of the surface can
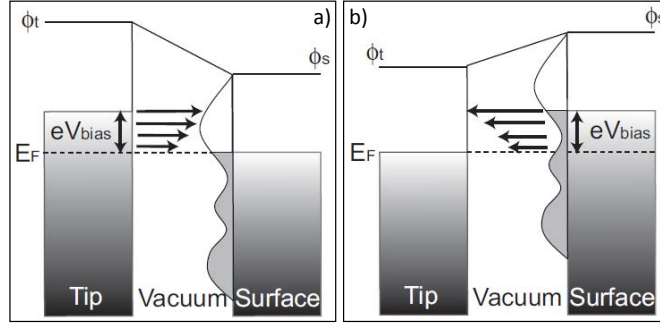
Figure 1.2: Schematic energy diagram in STS [56]. By varying the tip bias voltage at positive a) and negative b) polarities with respect to the sample, electrons tunnel into the unoccupied and out of the occupied states at the sample, respectively.

be obtained by mathematically fitting the corresponding $I \propto \exp(-A\varphi^{1/2}z)$ curve [51, 61]. Otherwise, if V ramps, the first order deviation, dI/dV, of the I-V curve can be directly measured by using a lock-in amplifier through adding a small modulation voltage to the bias voltage. The deviation can simply reflect the local density of states at the surface, as described in the following.

According to Eq. 1.4, the dI/dV is expressed as [59, 60, 62]:

$$
\begin{aligned}
\frac{dI}{dV} \propto\; & \rho_t(E_F)\rho_s(E_F + eV)T(E_F + eV, eV, z) \\
& + \int_{E_F}^{E_F+eV} \rho_t(E - eV)\rho_s(E)\frac{dT(E, eV, z)}{dV}dE \\
& + \int_{E_F}^{E_F+eV} \rho_s(E)\frac{d\rho_t(E - eV)}{dV}T(E, eV, z)dE
\end{aligned}
\tag{1.6}
$$

If we assume that the tunneling probability and the density of states of the tip are constant, the last two integral terms equal zero. Hence, Eq. 1.6 is simplified to:

$$
\frac{dI}{dV} \propto \rho_s(E_F + eV)
\tag{1.7}
$$

It means that the density of states of the surface can be directly investigated through ramping the bias and measuring dI/dV, the scanning tunneling spectroscopy. When the voltage varies at positive bias (figure 1.2 a), electrons tunnel from the tip into the unoccupied states at the surface, which are resolved as resonant peaks in the spectroscopy. Similarly, the occupied states can be detected when the bias varies at negative polarity with respect to the surface (figure 1.2 b). Since the tunneling probability decreases with the decrease of electron energy E (see Eq. 1.5), sometimes it is challenging to observe lower-lying occupied states of the sample in the scanning tunneling spectroscopy [63].

The spectroscopy can be recorded by keeping either z constant or I constant, namely, the constant height mode or the constant current mode. The constant height spec-

troscopy is more closely related to the sample states than the constant current mode, if the change of the tunneling probability $T(z)$ with the barrier width z is taken into account [63, 64]. Generally, peaks are slightly shifted to lower energy in the constant current mode [64].

Density of states of the surface at a certain energy can be spatially mapped by recording dI/dV signals at each points during scanning. Accordingly, there are two mapping modes as well: constant height and constant current. Each has its own advantages. To investigate a planar molecule, the constant height mode is better due to vanish of changing tip height. In contrast, the constant current mode is preferred for mapping a three dimensional object.

1.2 Atomic Force Microscopy

Since STM is based on the tunneling current flowing between the tip and sample, its application is restricted to study metals and semiconductors rather than insulators. The invention of the atomic force microscope in 1985 by G. Binnig et al. [65] extends the spectacular resolution investigation of surfaces in real space to nonconducting materials [15]. However, obtaining true atomic resolution with AFM is much more difficult than with STM due to the complexity of forces between the tip and sample combined with the difficulty to measure extremely small forces in vacuum [15]. It took one decade from the invention of the AFM to resolving Si(111)-(7 × 7) surface, a touchstone of the AFM's feasibility as a tool for surface science, with atomic resolution [66].

There are two basic operation modes in AFM: the static (contact) mode and the dynamic (non-contact) mode. In static mode, the force-induced deflection of the cantilever, $q = F_{ts}/k$, is directly used as the imaging signal, where F_{ts} is the force between the tip and the sample and k is the spring constant of the cantilever. During scanning, a feedback control loop is used to keep the deflection constant, resulting in a topography map $z(x, y, F_{ts} = \text{const.})$. In the dynamic operation mode, the cantilever is deliberately activated by an external excitation to oscillate around its eigenfrequency f_0. Two operation methods exist in the dynamic mode depending on the modulation signal: the amplitude modulation (AM) [67] and the frequency modulation (FM) [68]. In AM-AFM, the actuator is driven by a fixed amplitude at a fixed frequency. When the tip approaches the sample, the amplitude is changed by the force between the tip and the sample. This change is utilized as feedback signal for imaging. In contrast, the cantilever oscillates with constant amplitude in FM-AFM, while the frequency shift, $\Delta f = f - f_0$ induced by tip-sample interaction, acts as the imaging signal.

In this thesis, experiments are carried out in a combined frequency modulation STM-AFM, whose structure is illustrated in figure 1.3. As usual, the tunneling current and tip-sample bias can be directly measured in the STM part. There
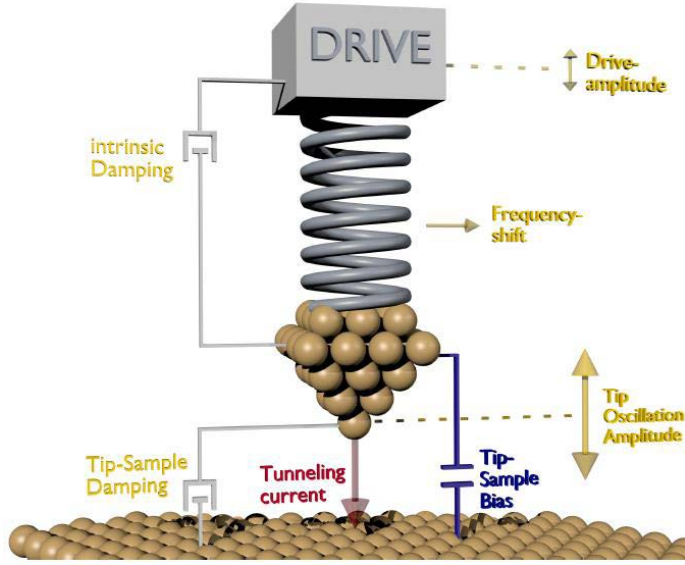
Figure 1.3: Scheme of the dynamic STM-AFM [69]. The yellow labels correspond to observables in the AFM part of the experimental setup.

are five measurable quantities in the AFM part: the drive amplitude, the intrinsic damping, the tip-sample damping, the tip oscillation amplitude and the frequency shift. The damping mechanism is out of the scope of this thesis. In the following, the relationship between the frequency shift and the tip-sample force will be derived. Then, the origin of the long- and short-range forces will be discussed. In the end, the mechanism of AFM imaging of molecular chemical structure is shown.

1.2.1 Theory of Atomic Force Microscopy

In the dynamic AFM, the vibrating cantilever can be treated as a harmonic oscillator with a single degree of freedom in the direction perpendicular to the surface. Its unperturbed motion is given by [70]:

$$q(t) = A_0 \cos(2\pi f_0 t) \tag{1.8}$$

where A_0 is the amplitude and f_0 is the resonant frequency determined by the spring constant k_0 and the effective mass m^* of the cantilever:

$$f_0 = \frac{1}{2\pi}\sqrt{\frac{k_0}{m^*}} \tag{1.9}$$

When the tip is approached close to the surface, the force between the tip and sample, F_{ts}, introduces perturbation to the oscillator, hence, inducing a change in the effective spring constant. In the case that the amplitude is much smaller than the tip-sample distance z, the effective spring constant is expressed as [70]:

$$k^* = k_0 - \partial F_{\text{ts}}/\partial z \tag{1.10}$$

where the second term, $k_{ts} = -\partial F_{ts}/\partial z$, represents the force gradient. If the force gradient is constant during the oscillation cycle, which is satisfied by the small amplitude, the frequency shift can be expressed as [70]:

$$\Delta f = -\frac{f_0}{2k_0}\frac{\partial F_{ts}}{\partial z} \tag{1.11}$$

It means that the imaging signal in FM-AFM, the frequency shift, directly reflects the force between the tip and sample.

The small oscillation amplitude is the premise of the above simple relationship between frequency shift and force, and also improves the quality of simultaneous STM measurements [15]. However, in many AFM studies larger amplitudes are used. A more general expression of the frequency shift valid for any amplitude of oscillation is obtained by using first-order perturbation theory in the Hamilton-Jacobi approach [70, 71]:

$$\Delta f = -\frac{f_0}{\pi A_0 k_0}\int_{-1}^{1} F_{ts}(d + A_0(1+u))\frac{u}{\sqrt{1-u^2}}du \tag{1.12}$$

where d is the distance of closest approach between the tip and sample. So if the tip-sample force function is known, the frequency shift can be calculated. In turn, the force can be deduced from the measured frequency shift curve [71]:

$$F(z) = \frac{2k_0}{f_0}\int_z^\infty \left\{\left(1 + \frac{\sqrt{A_0}}{8\sqrt{\pi(t-z)}}\right)\Delta f(t) - \frac{A_0^{3/2}}{\sqrt{2(t-z)}}\frac{\partial \Delta f(t)}{\partial t}\right\} dt \tag{1.13}$$

In the end, we note that the typical parameters of the tuning fork in our AFM measurements are: $k_0 = 1800$ N/m, $f_0 = 20$ kHz, $A_0 = 50$ pm and the quality factor $Q = 10000$.

1.2.2 Forces in Atomic Force Microscopy

In STM, the tunneling current exponentially decays with the tip-sample distance, which enables the high spatial resolution. However, forces between the tip and the sample in AFM are more complicated. In AFM, the frequency shift is induced by the sum of various types of forces with different strength and distance dependence. Amongst them, the chemical force, the van der Waals (vdW) force and the electrostatic force are the main contributions.

The Chemical Force

The chemical force starts to become significant, when the tip and the sample are closely approached to each other due to the overlap of electron wave functions from
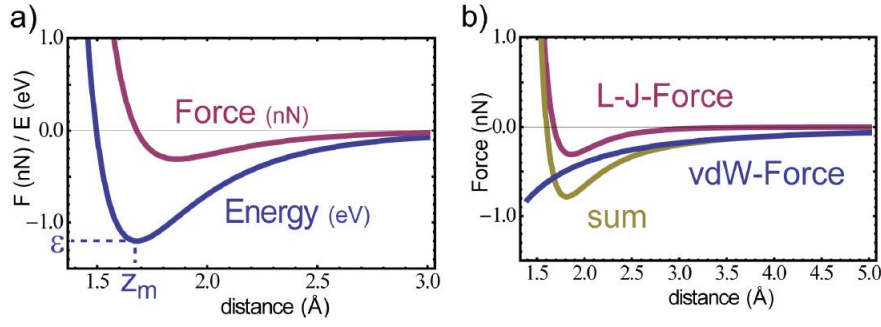
Figure 1.4: [69] a) Modeled Lennard-Jones potential and the corresponding Lennard-Jones force as a function of the distance between two atoms. Z_m and ϵ denote the bond distance and the binding energy, respectively. b) Lennard-Jones force from a, modeled van der Waals force (Hamaker approach) and the sum of them.

two parts. It can be both attractive and repulsive depending on the distance z, which is empirically described by Lennard-Jones potential [72]:

$$E_{\mathrm{LJ}}(z) = \epsilon \left[\left(\frac{Z_m}{z} \right)^{12} - 2 \left(\frac{Z_m}{z} \right)^{6} \right] \tag{1.14}$$

where ϵ is the bonding energy at the equilibrium distance Z_m. The $(1/z)^{12}$ term describes a repulsive force acting only at very short range. It originates from the Pauli repulsion. The Pauli principle inhibits overlap of electron wave functions from tip atoms and sample atoms, hence, forcing electrons to occupy higher energy levels and inducing repulsion force. In contrast, the $(1/z)^6$ term represents an attractive force stemming from the van der Waals force, which will be discussed later.

The corresponding force can be derived from the potential:

$$F_{\mathrm{LJ}}(z) = -\frac{\partial E_{\mathrm{LJ}}(z)}{\partial z} = 12 \frac{\epsilon}{Z_m} \left[\left(\frac{Z_m}{z} \right)^{13} - \left(\frac{Z_m}{z} \right)^{7} \right] \tag{1.15}$$

The modeled Lennard-Jones potential and force by using parameters of $\epsilon = $ -1.2 eV and $Z_m = 1.68$ Å are plotted in figure 1.4 a.

The van der Waals Force

The van der Waals force is caused by fluctuations in the electric dipole moment of atoms and their mutual polarization [15]. It is always attractive. The corresponding energy in a system of two atoms separated by a distance z can be expressed as:

$$E_{\mathrm{vdW}}(z) \propto - \left(\frac{1}{z} \right)^{6} \tag{1.16}$$

The van der Waals force between the macroscopic AFM tip and the sample can be quite large due to its additivity. The Hamaker approach suggests that for a spherical tip with radius R next to a flat surface the van der Waals force is given by [73]:

$$F_{\text{vdW,ts}}(z) = -\frac{HR}{6z^2} \tag{1.17}$$

where the Hamaker constant H depends on the type of materials and z is the distance between the plane connecting the centers of surface atoms and the center of the front tip atom. This equation indicates that the van der Waals force can be significantly decreased by using a sharper tip. Figure 1.4 b shows the calculated van der Waals force by using parameters of $R = 20$ Å and $H = 3$ eV together with the Lennard-Jones force and their sum. The van der Waals force plays a crucial role at larger tip-sample distance, while the chemical fore is dominant when the distance is closer. Therefore, it is necessary to scan at a close tip-sample distance to obtain the atomic resolution in AFM images.

The Electrostatic Force

The electrostatic interaction occurs when the conductive tip and sample carry different potential (work functions). The potential difference leads to a capacitance $C(z)$ varying with tip-sample distance z. In this case, the electrostatic force can be described as:

$$F_{\text{el,ts}} = \frac{1}{2}\frac{\partial C}{\partial z}(V - V_{\text{CPD}})^2 \tag{1.18}$$

where V is the applied voltage and V_{CPD} is the contact potential difference (CPD) between the tip and sample. Due to the term $\partial C/\partial z$ is always negative, the electrostatic force is therefore attractive all the time. The CPD can be experimentally determined by measuring the electrostatic-force-induced frequency shift as a function of the bias voltage. This is the kelvin probe force microscopy [74, 75, 76, 77, 78, 79, 80].

1.2.3 AFM Imaging Mechanism with Functionalized Tip

To resolve the chemical structure of organic molecules at atomic resolution is the ultimate goal in the field of microscopy. The invention of STM enables sub-molecular resolution imaging [38, 81, 82]. However, resolving individual atoms within molecules remains a great difficulty for STM, because the tunneling current is sensitive to the density of states of molecular orbitals rather than the corresponding chemical structure. In contrast, AFM images are generated by the forces varying with tip positions over atoms composing molecules, hence, revealing the chemical structure. The first success was realized by Leo Gross *et al.* [16]. They resolved the chemical structure of the pentacene molecule on Cu(111) (figure 1.5 a and b). This breakthrough was achieved by deliberately attaching a CO molecule to the AFM tip. Then, the

well-defined functionalized tip can be approached up to Pauli repulsion regime to the sample. The Pauli repulsion force, induced by the electron density overlap between the tip and the sample, becomes substantial at positions of atoms within the molecule. The variation of the Pauli repulsion force generates atomic contrast of the molecule in frequency shift images, while the electrostatic force and vdW force only add a diffuse attractive background (figure 1.5 c and d).
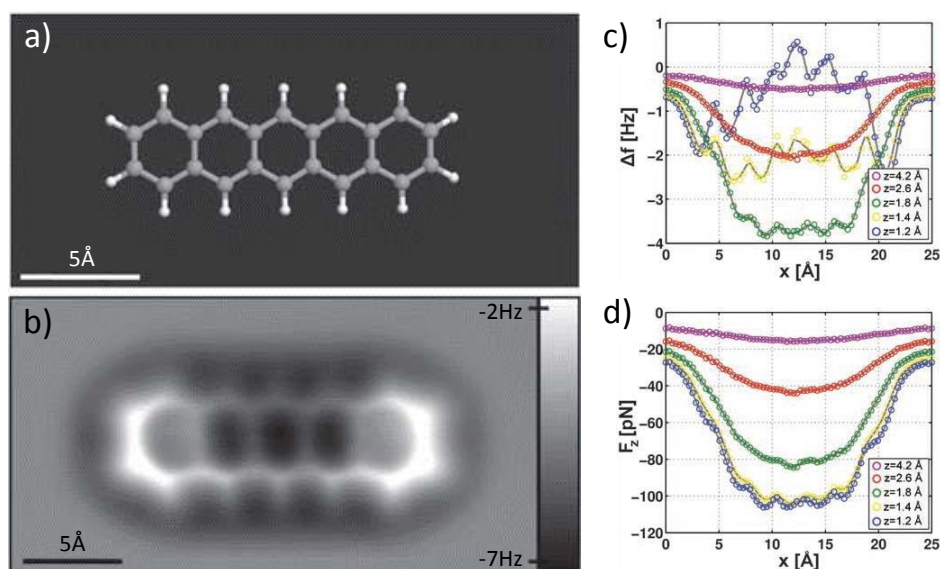

Figure 1.5: Images from [16]. a) Ball-and-stick model of pentacene. b) Constant-height AFM image of pentacene on Cu(111) acquired with a CO-modified tip. The tip was retracted by 0.1 Å from the set point of I = 110 pA and V = 170 mV above the Cu(111) substrate. c) and d) Line profiles of frequency shift Δf and extracted vertical force F_z along the long molecular axis at different tip heights z, respectively. The z values are given with respect to a STM set point of I = 2 pA and V = 200 mV above the substrate.

Based on this achievement, impressive progress has been made in the field of AFM imaging, including determination of chemical structure of unknown compounds [83], discrimination of bond order of organic molecules [84], determination of the adsorption geometry [85], resolving the transformation of covalent bonds in on-surface reaction [86] and imaging the interconversion pathway of a molecular switch [87].

In these studies, the sharp bright lines within individual molecules are assigned to chemical bonds directly interacting with the tip. Soon afterwards, it is claimed that intermolecular bonding also can be resolved as sharp contrast in AFM images [17, 90]. However, contrast can be observed between two no-bonded atoms as well, as shown in figure 1.6 a and b. Deeper understanding on the mechanism of AFM imaging with functionalized tip is necessary to interpret this contradiction. A recent theory work reveals that the sharp contrast between two atoms is induced by the relaxation of the attached molecule or atom on the AFM tip, from the repulsive potential ridge to the attractive potential basins (figure 1.6 c and d). Contrast
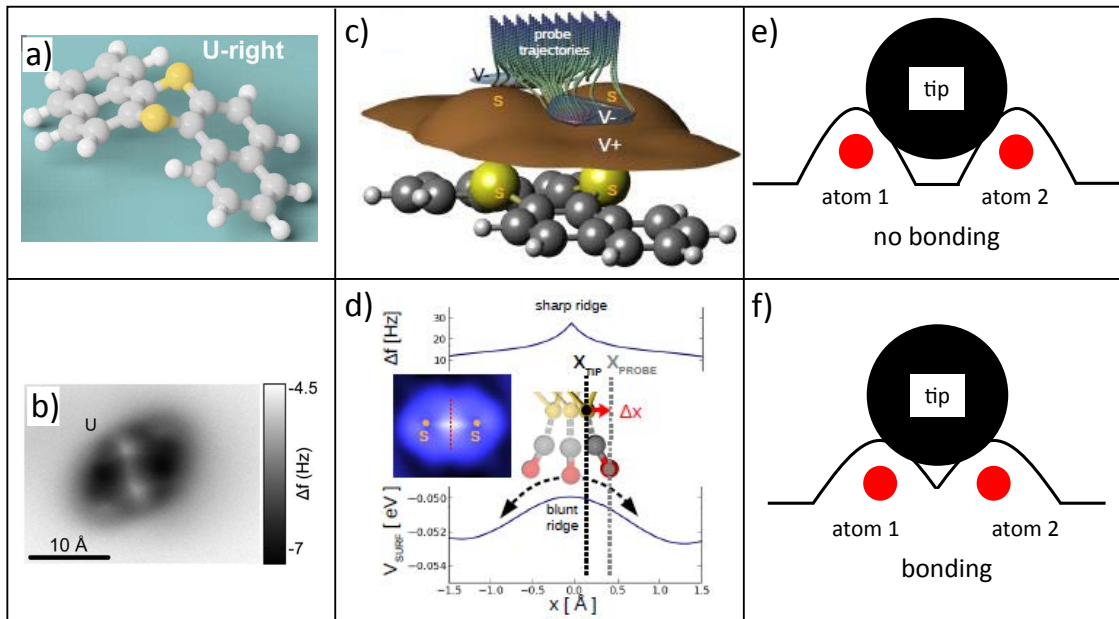
Figure 1.6: The mechanism of AFM imaging. a) Model of DBTH molecule with two sulfur atoms bent upwards from the surface [88]. b) AFM image of a DBTH on NaCl(2ML)/Cu(111) [88]. c) Model showing the potential felt by the functionalized tip over the molecule [89]. The brown curved surface (V+) stands for repulsive potential, while the attractive basins (V-) are in blue. d) The simulated frequency shift and potential along the central cross section of the repulsive saddle [89]. e) and f) Overlap of the electron wave functions from the tip with finite size and two no-bonded and bonded atoms on the surface, respectively.

emerges between any two close-located atoms, no matter they are not bonded (figure 1.6 e) or bonded (figure 1.6 f), due to the finite size of the modified tip. Therefore, the contrast in AFM images can not be simply assigned to intra- or inter-molecular bonding. Nevertheless, the position of atoms can be definitely resolved, from which the reasonable bonding structure can be determined.

1.3 Experimental Setup

All the results in this thesis were acquired in a combined STM/AFM located in LT and ultra high vacuum (UHV) environment, following the design of Dr. Gerhard Meyer and SPS-Createc GmbH [91]. The experimental system consists of two UHV chambers: the preparation chamber and the STM/AFM chamber, as shown in figure 1.7 a. Standard UHV preparation and maintenance tools are equipped in the preparation chamber, like mass spectrometer, sputter ion-gun, ion-pump, turbo-pump and molecular/metal evaporators. The STM/AFM chamber contains the SPM head, which is suspended at the bottom of a liquid-Ne/He cryostat working at an equilibrium temperature of 4.8 K. A rotatable linear manipulator is installed

for sample transfer between these two chambers. The coolable manipulator enables deposition of atoms or molecules on cold sample down to 100 K, while the button heater incorporated in the sample holder makes evaporation on warm sample up to 900 K possible. Contamination of SPM chamber during sample preparation is prevented through separation from the preparation chamber by a gate valve.
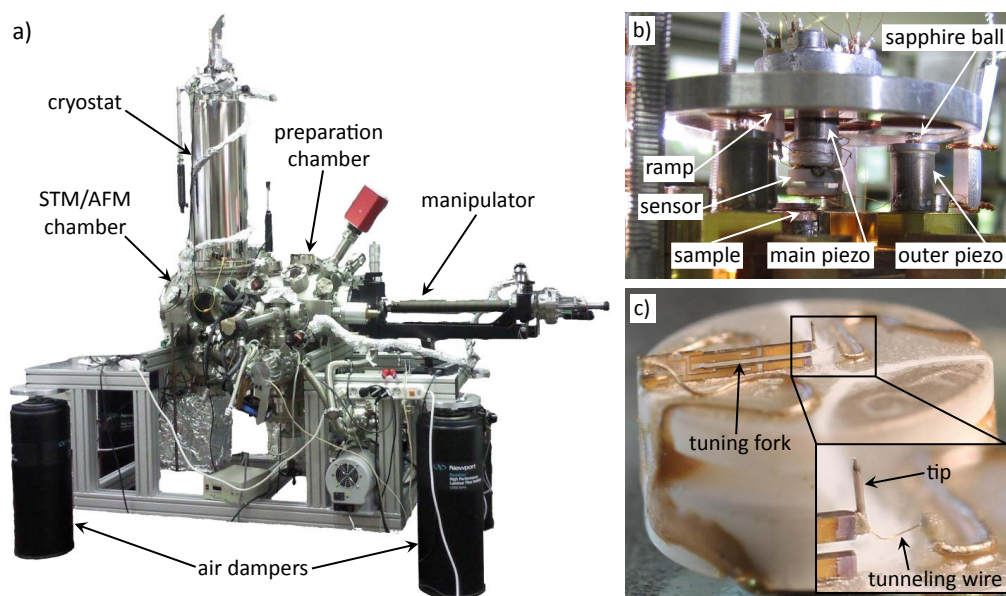

Figure 1.7: Experimental setup. a) Picture of the LT UHV STM/AFM chamber. b) Close-up of the STM/AFM head. c) Zoom-in of the tuning fork dynamic force sensor. Inset shows the SPM tip and tip wire for tunneling current.

Figure 1.7 b shows the structure of the SPM head with Besocke beetle type [92, 93]. Three outer (coarse) piezos are fixed on a baseplate, on top of which three sapphire spheres are mounted. A three-fold ramp made of copper can rotate around its center when applying sawtooth voltage pulses, which stands against the sapphire spheres. The accompanied increase or decrease of the ramp height is used for coarse approach. A ring made of aluminum around the ramp allows for lateral movement for changing scanning area over the sample. In the center of the ramp the main piezo used for scanning is mounted, where the tuning fork sensor is fixed with two magnets. The structure of the sensor is shown in figure 1.7 c. One prong of the tuning fork is glued on a Macor base, while the other prong with a tip remains free to oscillate perpendicularly to the sample surface. Three contacts are made between the scanner and the electrical feedthrough: two for the tuning fork piezoelectric AC current and one for the tunneling current. During measurement, the whole SPM head with sample clamped against the baseplate is isolated from mechanical vibrations *via* stainless steel springs, eddy current damping. The air damper feet can further improve the damping against low frequency vibrations through lifting the whole chamber.

The data acquisition was done using PSTMAFM software from SPS-Createc GmbH.

STS spectra were recorded with an external commercial Stanford Research SR830 lock-in amplifier. For AFM measurements, an additional phase locked loop (PLL) controller from SPECS-Nanonis was utilized. All the data were analyzed with the software of WSxM [94] and SpectraFox [95].

1.4 DFT Calculations

In order to gain theoretical supports for the experimental results, in this thesis we performed density functional theory (DFT) calculations for some measured systems. All the DFT calculations were performed using the GAUSSIAN 09 program package [96] unless noted otherwise. All calculations including geometry optimizations and electronic excitation energies were carried out on isolated systems, without considering the metal surfaces, using the B3LYP exchange-correlation functional. The 6-31G (or 6-311G) and LanL2DZ basis sets were chosen for the systems only containing molecules and the metal/molecule systems, respectively, as a compromise between accuracy and applicability to large molecules and metal atoms.

1.5 Substrates and Molecules

1.5.1 Coinage Metal Surfaces

In this thesis, three types of coinage metal surfaces are utilized as platforms for the growth of molecular architectures, namely Au(111), Ag(111) and Cu(111). They have a face centered cubic (fcc) crystalline structure. Metal atoms arrange into hexagons on the (111) surface of fcc crystal, exhibiting a three-fold (six-fold) symmetry in the first layer with (without) considering the atoms underneath [97], as shown in figure 1.8 a.

Figure 1.8 b shows the STM image of a Au(111) surface, where periodic soliton-lines with height of 0.2 Å are visible in $[11\bar{2}]$ direction due to atom rearrangement. Such reconstruction is induced by incorporating 23 atoms into 22 lattice sites [98] along $[1\bar{1}0]$ direction, as depicted in figure 1.8 c. Consequently, the surface layer is stressed with respect to the bulk and presents corrugation. Then the surface is divided into alternate wider and narrower regions with a period of 6.3 nm by the soliton-lines, corresponding to fcc and hcp packing structure, respectively. Figure 1.8 d represents a dI/dV spectrum recorded on a bare Au(111) surface. The two-dimensional Shockley surface state exhibits a step-like feature at about -500 mV [99]. Moreover, the reconstruction causes an electronic superlattice at the surface [99], where hcp region has lower potential energy by 25 meV accompanied with a higher local density of states (LDOS) compared with the fcc region. However, the lower concentration of atoms with respect to hcp region after taking into count the buried layers, makes fcc region energetically favorable for adsorption [98]. In

addition, molecules and impurities also preferentially adsorb at elbows of soliton-lines due to diminished potential energy there [100], as shown in figure 1.8 b.
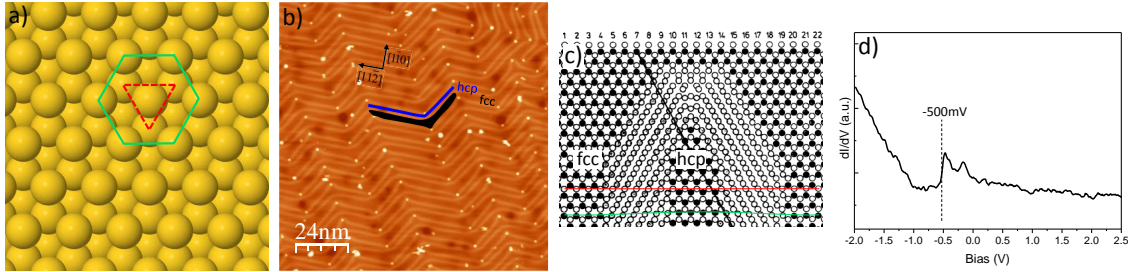

Figure 1.8: Au(111) surface. a) Topview of (111) surface of fcc crystal.   Green hexagon highlights atoms in the first layer, while red triangle highlights atoms in the second layer. b) STM image (I = 1.1 nA and V = 0.78 V) of Au(111) showing surface reconstruction. c) The reconstruction model [98]. Open circles represent atoms in the second layer, while filled circles stand for atoms in the first layer. d) dI/dV spectrum acquired with open feedback (set point: I = 45 pA and V = 3.0 V) at a bare Au(111) surface.
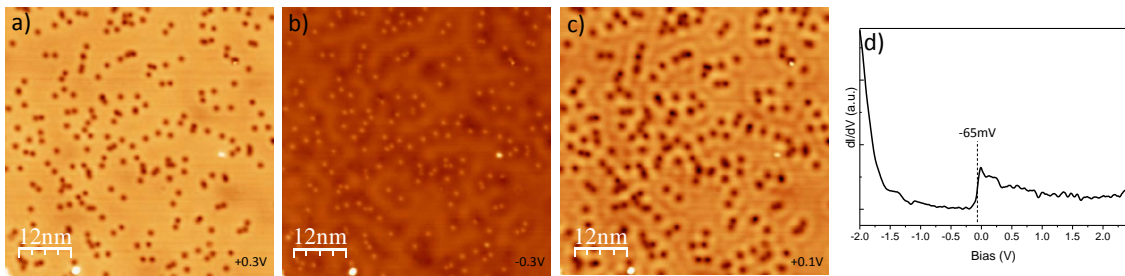

Figure 1.9: Ag(111) surface. a) - c) STM images of Ag(111) surface recorded at +0.3 V, -0.3 V and +0.1 V (I = 120 pA), respectively. CO molecules adsorb on the surface, which scatter the surface electrons. d) dI/dV spectrum acquired with open feedback (set point: I = 70 pA and V = 2.5 V) at a bare Ag(111) surface.

Figure 1.9 a shows the STM image of planar Ag(111) without surface reconstruction. Plenty of small depressions exist when scanning with positive bias, which are assigned to adsorption of CO molecules during sample preparation. They are imaged as protrusions at negative bias, as shown in figure 1.9 b. Moreover, standing waves centered at CO are observed in the STM image recorded near Fermi energy due to scattering of surface electrons [101, 102] (figure 1.9 c). In addition, dI/dV spectrum in figure 1.9 d reveals that the surface state of Ag(111) is localized at -65 mV [101, 102].

Similar with Ag(111), Cu(111) has homogenous surface structure with adsorption of CO molecules, as shown in figure 1.10 a. The resulting standing waves induced by CO scattering have a period of 15 Å (figure 1.10 b), corresponding to half the Fermi wavelength (λ_F) of the surface [103]. Cu(111) has a step-like surface state 450 meV below the Fermi energy, as shown in figure 1.10 c [103].
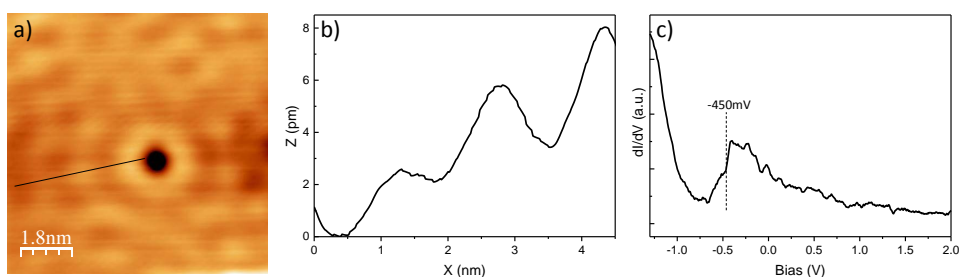
Figure 1.10: Cu(111) surface. a) STM image of a Cu(111) surface (I = 100 pA and V = 0.1 V) with adsorption of a CO molecule scattering the surface electrons. b) Linescan (indicated by the black line in a showing the wavelength (15 Å) of the standing wave centered at the CO molecule. c) dI/dV spectrum acquired with open feedback (set point: I = 20 pA and V = 2.0 V) at a bare Cu(111) surface.

1.5.2 Dicyanovinylene-substituted Oligothiophenes

Dicyanovinylene-substituted oligothiophenes (DCVnTs in short, n represents the number of thiophene rings) are adopted widely in the field of organic solar cells [42, 43, 44, 45, 46, 47, 48, 49, 104]. In this thesis we studied two types of molecules from this family: the methyl-substituted dicyanovinyl-quinquethiophenes (DCV5T-Me$_2$) and the dicyanovinyl-hexathiophenes (DCV6T). The chemical structures of these two types of molecules are shown in figure 1.11. DCV5T-Me$_2$ has two dicyanovinyl (DCV) functional groups that are linked symmetrically to a central quinquethiophenes (5T) group with the central thiophene ring substituted by two methyl (Me$_2$) groups. DFT calculations reveal that there are several types of isomers for DCV5T-Me$_2$ molecules in gas phase, with differently oriented thiophene rings and DCV groups. Amongst them the slightly bent configuration, due to methyl groups' attachment, with alternately oriented thiophene rings and proximity of cyano groups and sulfur atoms from the neighboring thiophene rings has the lowest total energy [48]. The most stable configuration, with a total length of 2.75 nm, adopts C$_{2v}$ symmetry with all the atoms located in the same plane except the hydrogen atoms in the methyl groups (Fig. 1.11 a).

DCV6T has one more thiophene ring than DCV5T-Me$_2$, but without substitution by methyl groups. DFT calculations demonstrate that DCV6T possesses different types of configurations in the gas phase as well. The alternate arrangement of the six thiophene rings and the CN-S interaction generate the most stable molecular configuration [48]: straight, planar and C$_{2h}$ symmetric with a total length of 3.0 nm (Fig. 1.11 b).

In bulk DCV5T-Me$_2$ forms single crystal [105]. X-ray data reveal that molecules are arranged in rows in (6 0 4) plane through hydrogen bonding between vinylic or aromatic CH and N atoms from neighboring cyano groups (blue lines in figure 1.12 a). Two adjacent rows are offset by half molecular length in plane and interact with each other *via* hydrogen-bonds between aromatic CH and cyano groups (red lines
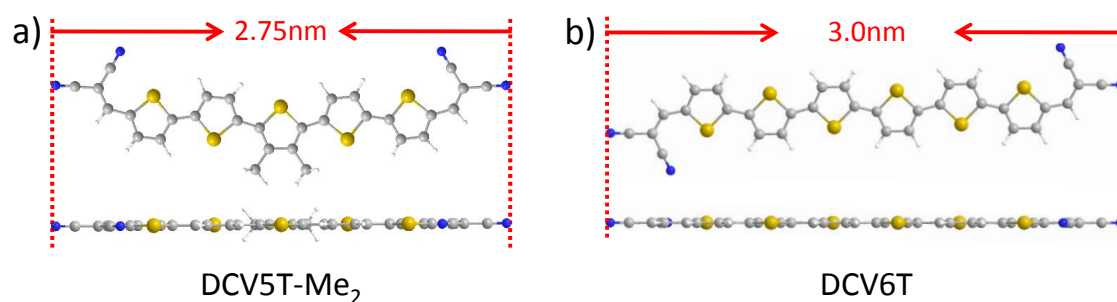
Figure 1.11: a) and b) Chemical structures and optimized configurations of the free DCV5T-Me$_2$ molecule and DCV6T molecule in gas phase, respectively. The color code is white: hydrogen, grey: carbon, blue: nitrogen and yellow: sulfur. Molecules were synthesized by Roland Fitzner.
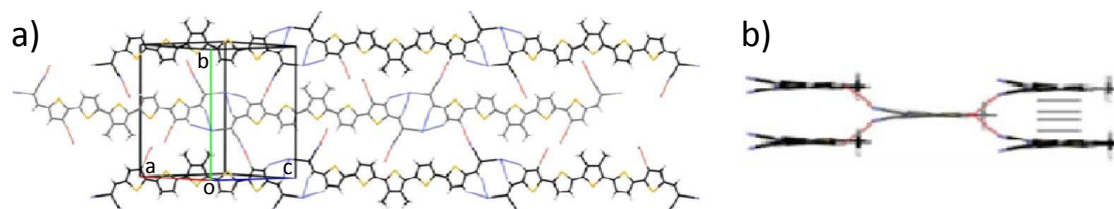

Figure 1.12: Images from [105]. a) Packing structure of DCV5T-Me$_2$ in one layer in the single crystal viewed from the direction normal to the (6 0 4) plane. The blue and red lines stand for hydrogen-bonds. b) The inter-layer packing structure in the single crystal viewed from the direction normal to the (6 0 $\overline{7}$) plane. The gray lines represent π-π interaction, while the red lines show the same hydrogen-bonds as in a.

in figure 1.12 a). Moreover, neighboring rows are located at different height with a distance around 1.6 Å in the direction perpendicular to the (6 0 4) plane, as shown in figure 1.12 b. Molecules within adjacent layers stack through π-π interaction (gray lines in figure 1.12 b). Both hydrogen bonding and π-π stacking stabilize the packing structure, moreover, enhance the intermolecular orbital overlap during charge transport.

DCV6T grows into crystal in bulk as well, where molecules extend in layers parallel to the (9 3 21) plane [48], as shown in figure 1.13 [2]. One unit cell of the crystal contains two pairs of molecules aligning with an angle, with two parallelly aligned molecules in each pair (figure 1.13 a). The short distances, below the van der Waals radii, between the hydrogen atoms from parallelly aligned molecules indicate van der Waals interaction (red dot lines in figure 1.13 a). In addition, every molecule points its cyano groups to the hydrogen atoms from the neighboring molecules forming hydrogen-bonds (red solid lines in figure 1.13 a). In the direction perpendicular to

---

[2]Here we show the X-ray data of DCV4T. It should have the same packing structure as DCV6T, because both of them have even number of thiophene rings in the center exhibiting the same symmetry.
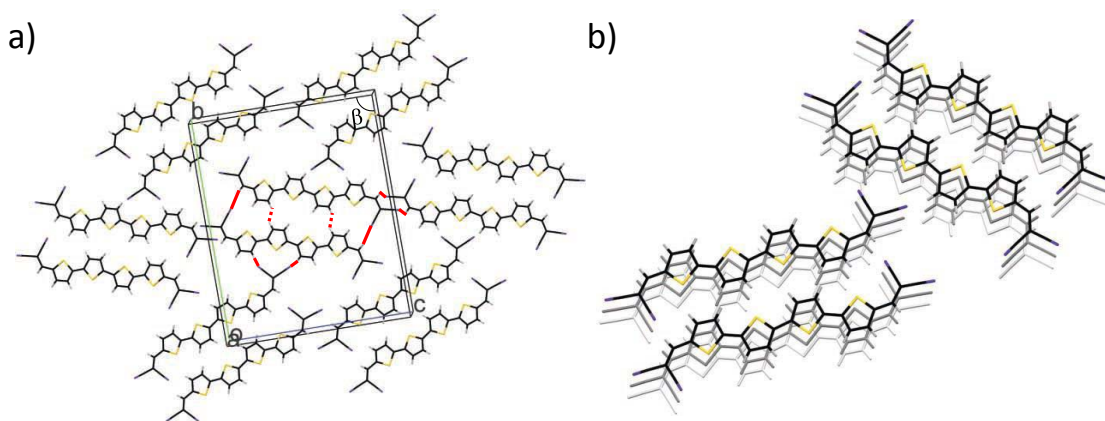
Figure 1.13: Images from [48]. a) Packing structure of DCV4T in one layer in the single crystal viewed from the direction normal to the (9 3 21) plane. The red dot lines stand for van der Waals interaction, and the red solid lines represent the intermolecular hydrogen-bonds. b) The inter-layer π-π stacking structure in the single crystal from the same point of view as in a. The molecules in adjacent layers are drawn in gray gradation.

the (9 3 21) plane, the X-ray data show that the packing structure is optimized by π-π interaction: the aromatic backbones of neighboring layers are almost completely overlapped (figure 1.13 b), which benefits the charge transport in the crystal. All of these intermolecular interactions consolidate the crystal [48].

DCVnTs include both electron donor (thiophenes) and acceptor (DCV groups) parts simultaneously [106] [3]. However, they serve as electron donors in the organic solar cells when combined with C_{60} due to the relatively lower electronegativity [48]. There are two kinds of structures for organic solar cells based on DCVnTs and C_{60}: the planar heterojunction and the bulk heterojunction, as shown in figure 1.14 [48]. One layer of DCVnT and one layer of C_{60} contact to each other in the planar heterojunction, while the DCVnT and C_{60} form one blend layer in the bulk heterojunction. Each one has its own advantages and disadvantages. It is difficult for excitons to diffuse to the interface between two layers and separate into electrons and holes in the planar heterojunction, whereas it is good for the charge transport to electrodes after exciton separation. The bulk heterojunction improves the efficiency of the exciton separation due to the shorter diffusion distances for excitons before reaching the donor-acceptor interfaces. However, the probability of recombination for the charge carriers during transport to electrodes is increased in the bulk heterojunction. A lot of attempts have been made to improve the exciton separation and carrier transport in these two types of heterojunctions, like adjusting the packing structures by attaching side groups [47, 49, 104] and changing the morphology of molecular layers [46], and so on.

---

[3]The aim of attachment of electron acceptor groups is to reduce the molecular optical band gap for enhancing the solar photon absorption, which is mainly ranged between 600 to 800 nm.
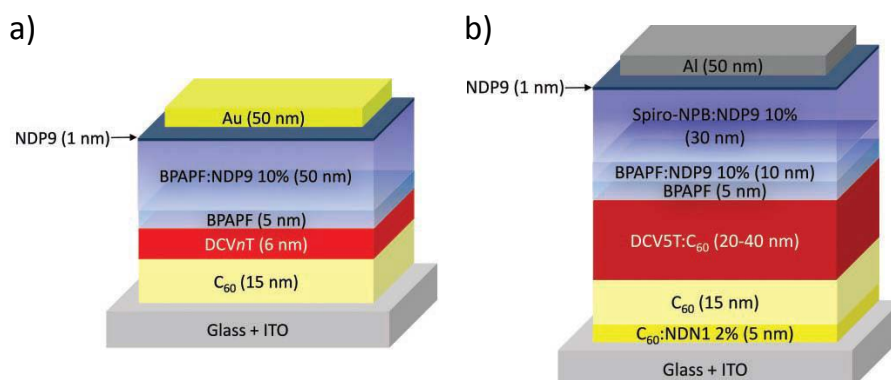
Figure 1.14: Images from [48]. a) and b) Stacking structures of the organic solar cells with planar heterojunction and bulk heterojunction of DCVnT and C$_{60}$, respectively.
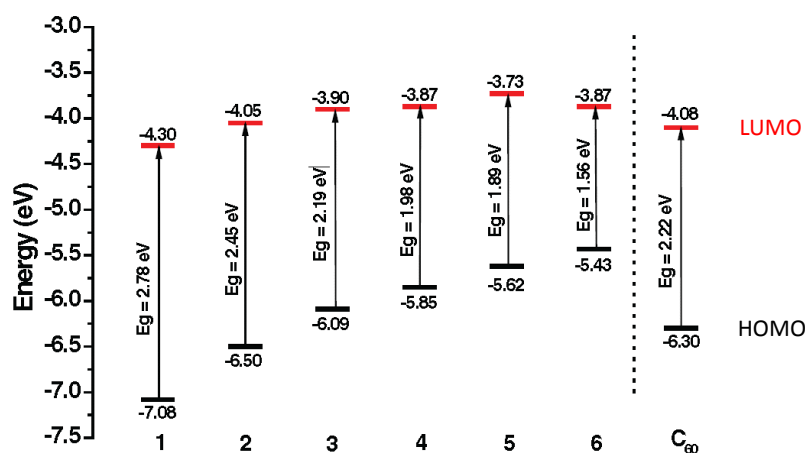
Figure 1.15: Image from [48]. Representation of HOMO/LUMO energies of the DCVnTs (n: 1 - 6) derived from electrochemical data and compared with C$_{60}$.

The performance of the organic solar cells, assessed with the parameters of open-circuit voltage and conversion efficiency, is mainly determined by the energy alignments between the electron donors and acceptors besides the packing structure of organic layers [104]. The bigger the effective energy gap (gap between the HOMO of the donor and the LUMO of the acceptor) is, the higher the open-circuit voltage we gain. On the other hand, the bigger effective energy gap increases the difficulty for charge transfer from the donor to the acceptor, thereby decreasing the conversion efficiency. Therefore, we need to get a trade-off between the open-circuit voltage and the conversion efficiency by tuning the energy alignments of the components. Figure 1.15 shows the energy alignments of DCVnTs with respect to C$_{60}$ [48], data from electrochemical measurements. It is demonstrated that the HOMO of the DCVnTs increases in energy with the increases of the number of the central thiophene rings, while the energy of the LUMO is not strongly modified. Therefore, the performance

of the solar cells can be optimized by tuning the length of the molecules. Within DCVnTs family, the DCV5T-Me$_2$, with combination of C$_{60}$, constructs organic solar cells with the highest efficiency of 7% [106].

In contrast to the extensive studies on structural and electronic properties of DCVnTs in bulk with assemble-average techniques, a microscopic understanding of their geometric and electronic structures on metal surfaces at sub-molecular resolution is still missing. The transition from three-dimensional crystals in bulk to one- or two-dimensional supramolecular architectures on metal surfaces should introduce new phenomena to the system. On one hand, the hybridization between molecules and metal surfaces or adatoms from substrates dominates the structural and electronic properties at the metal-organic interface. On the other hand, molecules decoupled from the metal surfaces within a multiple layer film should exhibit intrinsic properties of the organic substance. In addition, different packing structures are expected to arise in the low-dimensional assemblies. Furthermore, doping the DCVnTs with metal atoms is expected to be another effective way to tune the electronic properties of materials besides mixing them with other organic substance. Therefore, exploring molecular properties of different DCVnTs-based assemblies on metal surfaces with STM and AFM is significant, from the point of application, in order to improve their performance in organic solar cells and even extend their application in other organic devices. From the point of fundamental research, DCVnTs including π-conjugated backbone with positive sulfur and hydrogen atoms and negative cyano groups, offer abundant resource for study in the field of surface science.

1.5.3 Sample Preparation

The Au(111), Ag(111) and Cu(111) samples were cleaned by repeated cycles of Ne$^+$ sputtering (1.5 keV) held at room temperature and subsequent annealing to 750 K. This procedure ensures surfaces free of impurities with big terraces for the adsorption of molecules and metal atoms.

The organic molecules were evaporated onto the cleaned samples *in situ* in the UHV chamber from an organic molecular evaporator with a quartz balance to control the deposition coverage. The temperatures for the evaporation of organic molecules are shown in table 1.1. NaCl molecules, offering Na atoms to mix with organic molecules, were evaporated onto the samples in the same way as organic molecules with an evaporation temperature of 530 °C. The Co atoms were deposited by using a commercial Omicron UHV evaporator EFM3 loaded with high purity Co rod (>99.995%). The evaporation flux was tuned with an integrated flux monitor. The samples were held at room temperature during the adsorbate deposition unless noted otherwise. To keep the DCV5T-Me$_2$ intact on the Cu(111) surface, the Cu(111) sample was held at low temperature during evaporation followed by annealing to thermally activate the formation of self-assembled nano-structures.

A small amount of CO, Cl or Xe molecules are needed to functionalize the tip for AFM measurements. In this thesis we chose Xe since it induces less deviation to AFM images [107]. The Xe molecules were dosed onto the surface by admitting Xe gas into the SPM chamber with a pressure of 1×10^{-6} mbar for 1 minute.

Molecules	DCV5T-Me$_2$	DCV6T	TCNQ	Coronene	C$_{60}$	NaCl
Temperature	240ºC	300ºC	120ºC	120ºC	450ºC	530ºC

Table 1.1: Temperatures for evaporation of molecules.

2 Structural and Electronic Properties of DCV5T-Me$_2$ Organic Films on Au(111)

2.1 Introduction

In supramolecular chemistry, organic molecules self-assemble into ordered structures connected through intermolecular non-covalent bonding. Upon adsorption on a metal surface, the scenario is drastically changed. First of all, the growth of the nanostructures is confined in two dimensions. Moreover, the induced-vertical interactions between the surface and ligands compete with lateral intermolecular interactions, hence, modify structural properties of the assemblies [3]. Consequently, sometimes it is a challenge to expect and determine the packing structure of complex molecules on metal substrates just based on STM images. Therefore, AFM is utilized to resolve the molecular configuration at atomic resolution [16], furthermore, gain significant information on intermolecular bonding geometry.

The intermolecular bonding determines the local chemical environments of a molecule, thereby influencing its electronic properties. At organic/organic interfaces, intermolecular interactions may induce modification to the free molecular properties through screening effect [56], dipole formation [108] and so on. Understanding the evolution of molecular orbital energy alignment upon self-assembly is significant for a designed electron donor molecule, since a higher-lying LUMO in energy is preferred for electron donation.

Recent STM studies of organic molecules are mainly focused on single molecules and self-assembled structures in sub-monolayer level on metal surfaces. However, organic devices, such as organic solar cells and organic light emission diodes, are composed of multiple layers of molecules, whose orbital energy alignment and spatial distribution determine the charge transfer and transport process in the system. Moreover, the multiple-layer film offers an ideal platform to investigate molecular vibronics. On one hand, the vibration induces substantial energy dissipation to the system that drastically reduces stability and lifetime of the device [109]. On the other hand, it triggers the charge delocalization in a charge transfer complex [110, 111]. Besides the resonant and vibrational states, the molecular packing structure within multiple layers also strongly influences the charge transport in organic electronics [104]. Therefore, it is significant to study the structural and electronic properties of

molecules within multiple-layer organic films contacting with metal surfaces, which resemble the real chemical environments of organic devices.

Previous studies have demonstrated that octithiophene (8T) molecules are arranged in parallel within both the first layer and the second layer on Au(111), driven by van der Waals forces and π-π interaction (figure 2.1 a) [29]. Moreover, molecules within both layers exhibit the same orbital alignment (figure 2.1 b), indicating a weak hybridization between 8T and the substrate. In contrast, dicyanovinylene-substituted oligothiophenes, specially designed for organic solar cells, are expected to show different packing and electronic features from unsubstituted oligothiophenes due to the functional cyano groups. However, a microscopic understanding on these molecules is still missing. Therefore, here we use a combined low temperature STM/AFM to investigated DCV5T-Me$_2$ on Au(111).

In the first part of this chapter, we show the bonding geometry of DCV5T-Me$_2$ molecules *via* AFM imaging. It is found that the intermolecular electrostatic interaction combined with hydrogen bonding is in response for the formation of molecular islands, which enhances the thermal stability of the pure organic domains. In the second parts of this chapter, the change of free molecular orbital structure upon assembly is studied, which is attributed to the strong intermolecular interactions. In the third part of this chapter, structural and electronic properties of a double-layer film is presented. Molecules in the second layer pack in the same way as those in the organic islands, exhibiting higher-lying unoccupied orbitals due to being decoupled. Moreover, a vibrational state with energy of 180 meV is detected there, corresponding to stretching mode of carbon bonds.
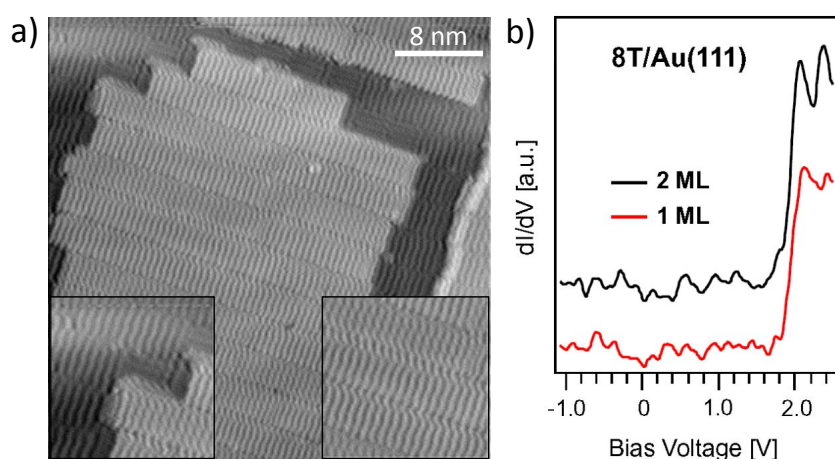

Figure 2.1: Images from [29]. a) Overview STM image of a mono- and bilayer 8T on Au(111) (V = -0.6 V, I = 50 pA). Inset: zoom in STM images of the first layer (left bottom) and the second layer (right bottom), respectively. b) dI/dV spectroscopic data taken at the first layer and the second layer of 8T on Au(111).

2.2 Self-assembly of DCV5T-Me$_2$

We start by describing the assemblies found with LT-STM inspection. When DCV5T-Me$_2$ is deposited on a Au(111) surface at room temperature, it predominantly forms two types of structures: bi-molecular chains and two-dimensional molecular islands (figure 2.2 a). Molecules within both chains and islands adopt a bent configuration. In the chains, every pair of molecules connects to adjacent pairs through their DCV ends (figure 2.2 b), hence, form chains extending typically over more than one hundred nano meters across the herringbone reconstruction of the surface. In the islands, molecules contact their DCV ends instead with centers of neighboring molecules (figure 2.2 c), thereby forming domains with extension of hundreds of nano meters in two dimensions. Moreover, the surface reconstruction underneath the islands is not perturbed by the adsorption of DCV5T-Me$_2$, indicating that the interaction between surface and molecules is weak [28].
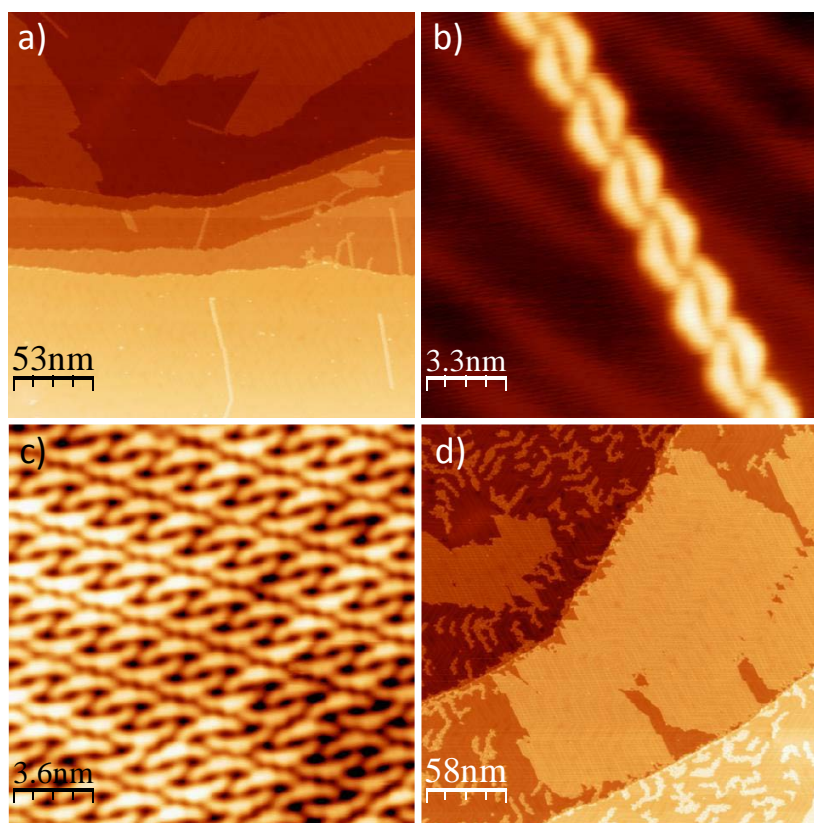
Figure 2.2: Self-assembly of DCV5T-Me$_2$ on Au(111). a) STM overview (I = 73 pA, V = 0.69 V) of DCV5T-Me$_2$ molecules deposited on room temperature Au(111) surface. Chains and islands coexist on the surface. b) and c) High resolution STM images of the chain (I = 71 pA, V = 0.89 V) and the island (I = 81 pA, V = 0.59 V), respectively. d) STM overview (I = 83 pA, V = 0.65 V) after annealing the sample to 280 °C.

These two types of self-assembled structures exhibit different thermal stability. Post-

annealing the sample to 280 °C destroyed the chains completely, while the islands are not influenced at all, as shown in figure 2.2 d. The origin of the difference in thermal stability between the chains and the islands, could be related to different bonding structures. Since it is difficult to determine the exact bonding geometry of chains and islands from STM images, we performed AFM measurements. AFM imaging of islands is shown in the following, while AFM results on chains will be discussed in the next chapter.

2.3 Bonding Determination of Islands with AFM

2.3.1 Functionalization of the AFM tip

In order to gain atomic resolution in AFM images, it is necessary to functionalize the tip with a well defined molecule or atom [16] such as CO, Xe, Cl and so on. In this thesis, all AFM images were recorded with Xe functionalized tips. To functionalize the tip, we dosed Xe molecules onto the sample while seated in the STM chamber, after deposition of organic molecules (details in section 1.5.3). They form big islands with some Xe atoms dispersing separately on the surface, as shown in figure 2.3 a. They also adsorb at edges of DCV5T-Me$_2$ molecular islands (figure 2.3 b). The Xe can be picked up by approaching the tip 4 Å with a typical current set point of 20 pA and 100 mV over it [107]. The absence of Xe at its previous position and the enhanced resolution of STM image recorded with the tip afterwards (figure 2.3 c), indicate that the Xe is attached at the apex of the AFM tip. In general, this method generates quite stable tips that can work several tens of hours before breaking.
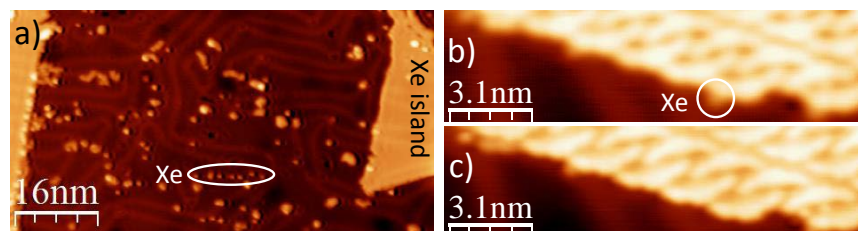
Figure 2.3: Functionalization of the AFM tip with Xe. a) STM image (I = 50 pA, V = 0.31 V) after deposition of Xe on the Au(111) sample with DCV5T-Me$_2$. Large Xe islands are formed with some Xe molecules dispersing on the surface (within the white oval). b) STM image (I = 9.7 pA, V = 0.24 V) of a molecular island with adsorption of Xe at its edge. c) STM image (I = 20 pA, V = 0.1 V) of the same area as in b after picking up a Xe.

2.3.2 Chemical and Bonding Structure of Islands

Figure 2.4 a and b show the STM topography and the corresponding Laplace filtered constant height AFM image of a molecular island, respectively. Chemical structure of DCV5T-Me$_2$ is resolved with atomic resolution. In AFM image, the sulfur atom
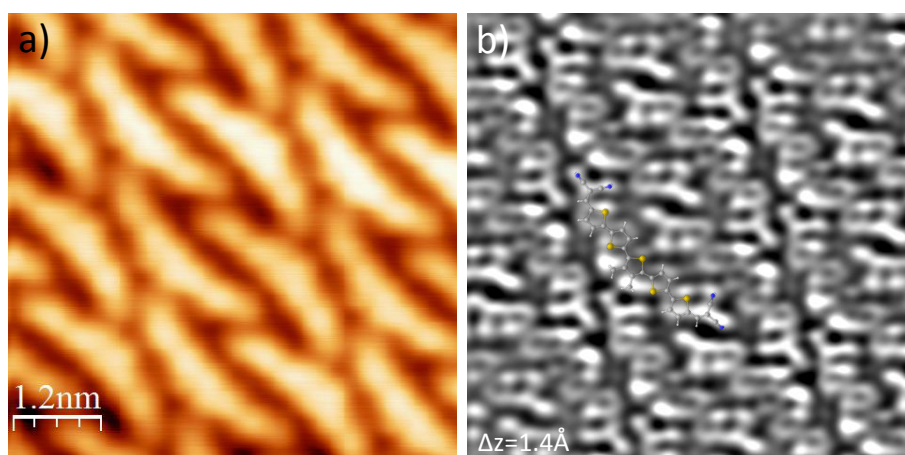
Figure 2.4: AFM Imaging molecular chemical structure of the islands. a) Constant current STM image (I = 50 pA, V = 0.31 V) of an island. b) Laplace filtered frequency shift image of the same island acquired at constant height mode. The tip was approached by 1.4 Å to the sample from the current set point of 0.31 V and 50 pA over the molecule. The DFT optimized configuration of the isolated molecule in gas phase is superimposed over the AFM image.

exhibits the sharpest contrast within a thiophene ring. Based on this fact, it is determined that the five thiophene rings are alternately arranged. The cyano groups are resolved as protrusion lines with brighter contrast localized at the end nitrogen atoms, probably due to abundance of electrons there. DCV groups are arranged in such a way that one of the two cyano groups is close to the sulfur atom at the adjacent thiophene ring. In spite of the large conformational flexibility of DCV5T-Me₂, most of the molecules appear with this shape. DFT calculations of the isolated molecule reveal that, although there are several DCV5T-Me₂ conformers with similar stability in gas phase, the shape observed here corresponds to the global minimum. This minimum energy configuration has a planar structure, thus enhancing its relative stability when forced to lay in a planar adsorption geometry on a metal surface.

At a closer tip-sample distance, contrast emerges at the positions between adjacent molecules, as shown in figure 2.5 a. As demonstrated in a recent theory study [89], these protrusion lines indicate close location of two atoms. They do not directly correspond to intermolecular bonding, however, from which reasonable interaction model could be constructed. Close located CN ligands and CH groups form hydrogen-bonds (red lines in figure 2.5 b). Two adjacent atoms with opposite sign of charge interact with each other through electrostatic force. This explains the rotation of one cyano group close to the sulfur atom from the neighboring thiophene ring. Intramolecular electrostatic interaction (blue lines in figure 2.5 b) induces the proximity of positively charged sulfur and negatively charged nitrogen (figure 2.5 c). For the same reason, we propose that intermolecular S-N electrostatic interaction (green lines in figure 2.5 b) also contributes to the formation of the islands. Moreover, neighboring cyano groups point to different directions, indicating that no metal

bridges are necessarily needed and the islands are pure organic motifs. Actually, the packing structure here is similar with that in the crystal (figure 1.12). The metal surface inhibits the growth of parallel rows in three dimensions, thereby assembling them into two dimensional domains here.
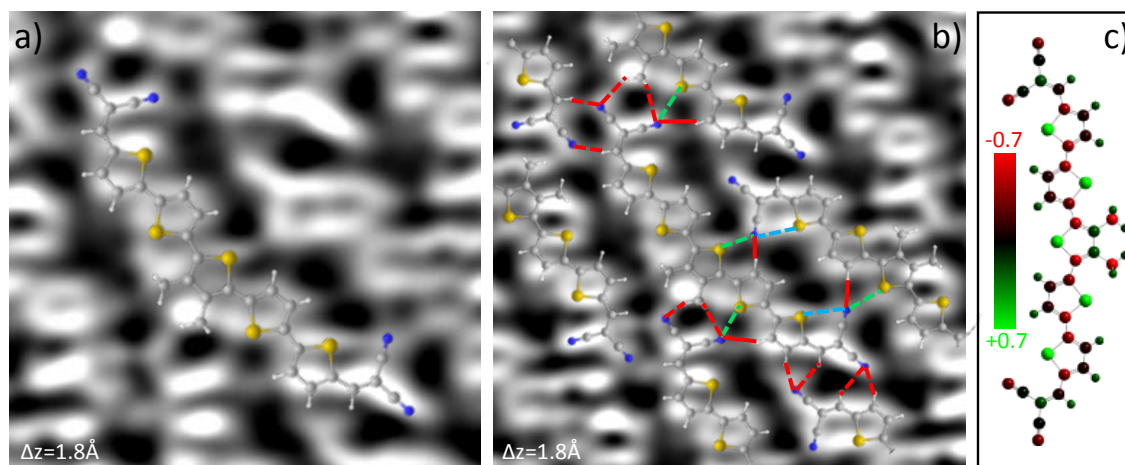

Figure 2.5: a) and b) Laplace filtered AFM images acquired at 0.4 Å closer tip-sample distance than in figure 2.4 b. The tip was approached by 1.8 Å to the sample from the current set point of 0.31 V and 50 pA over the molecule. The size of image a (b) is 2.7 × 2.7 nm (3.5 × 3.5 nm). The bonding model is superimposed over b: out-of-direction hydrogen-bonds (red dash lines), in-direction hydrogen-bonds (red solid lines) and intermolecular electrostatic interactions (green dash lines). The blue dash lines indicate intramolecular electrostatic interaction. c) DFT calculated total charge distribution of a free molecule in gas phase.

Bonding type	Energy	Distance
Hydrogen bonding	0.05–0.7 eV	≈1.5–3.5 Å
Electrostatic interaction	0.05–2.5 eV	long range
Coordination bonding	0.5–2 eV	≈1.5–2.5 Å

Table 2.1: Energy range and interaction distance of different types of bonding [3].

Analysis of the bonding structure in detail reveals that each one molecule possesses nine bonds (or interactions) including five out-of-direction hydrogen-bonds (red dash in figure 2.5 b), two in-direction hydrogen-bonds (red solid in figure 2.5 b) and two electrostatic interactions (green dash in figure 2.5 b). The organic islands have more intermolecular interactions in total than the chains (each one molecule in chains has one coordination bond and four out-of-direction hydrogen-bonds, which will be discussed in chapter 3). The larger amount of intermolecular interactions should play a crucial role in the structural and electronic properties of the organic islands. The extremely high thermal stability of the islands is one of the consequences. Although

the electrostatic interaction is a long range interaction, it could have even higher binding energy than hydrogen-bonds and coordination bonds, as shown in table 2.1. This rationalizes the higher thermal stability of the pure organic islands than the metal-organic chains.

2.4 Electronic Properties of Islands

2.4.1 The Single DCV5T-Me$_2$

STS was utilized to inspect the electronic configuration of organic islands. As a reference, we measured first spectra on individual DCV5T-Me$_2$ monomers, occasionally lying on bare gold regions. DCV5T-Me$_2$ monomers appear in STM images with the same conformation as in the molecular islands (figure 2.6 a). Differential conductance spectra acquired on the center and on the DCV end-groups of a DCV5T-Me$_2$ monomer show a clear peak at 2.0 V (figure 2.6 b) with its largest intensity at the center of the molecule, which we assign to the LUMO-derived resonance. In contrast, the LUMO+1 resonance with onset of 2.5 V [1] is only localized at the two ends. The extended and local character of the LUMO and the LUMO+1, respectively, is in agreement with the free-molecular orbital shape obtained from our DFT calculations (inset of figure 2.6 b), and confirms that DCV5T-Me$_2$ monomers maintain to large degree their free-molecule character upon adsorption on the Au(111) surface.
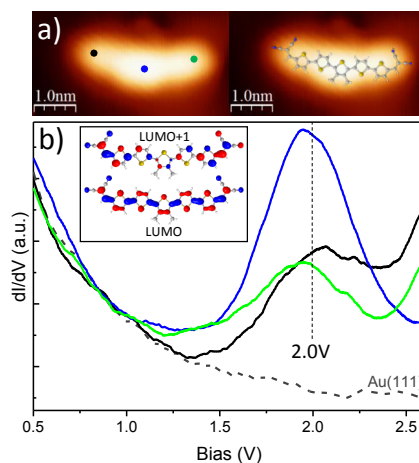
Figure 2.6: a) STM images (I = 67 pA and V = 0.89 V) of a single molecule on Au(111) with DFT calculated optimization configuration superposed (right panel). b) dI/dV spectra acquired with closed feedback (set point: I = 50 pA and V = 0.5 V) at different locations on a single molecule and the surface as indicated in a. The energetic positions of the resonances in the dI/dV spectra are highlighted by the black dash vertical line. Inset is the DFT calculated orbital shape of the LUMO and LUMO+1 in gas phase.

---

[1] The LUMO+1 can not be completely resolved because the molecule becomes mobile when tunneling in that energy region, but the onset of the resonance is clear.

2.4.2 The Islands

The STS spectra in the molecular island (figure 2.7 a and b) show a resonance at 1.3 V distributed over the whole molecule, and a higher-lying resonance at 1.65 V, which is mainly localized at the molecular sides. This distribution is further confirmed by dI/dV mapping, as shown in figure 2.7 d and e. By comparing with the distribution of states over the single molecule, we assign these two resonances to states derived from the LUMO and LUMO+1 of the molecule within islands, respectively.

These results show that the LUMO and LUMO+1 are shifted down to 1.3 V and 1.65 V in islands from 2.0 V and >2.5 V at the single molecule on Au(111). Spectra recorded on the molecule at the edge of the island (dash curves in figure 2.7 b) exhibit states with similar energies with those at the molecule within the island (solid curves in figure 2.7 b). It indicates that the screening effect does not strongly influence the resonance alignment here. Therefore, we attribute this shift to the presence of intermolecular interactions, which is the only possible origin for the change of electronic properties. Studies have demonstrated that the LUMO and the LUMO+1 states of PTCDA molecules within different domains, where the average hydrogen-bonds length varies 0.3 Å, are different in energy [19]. The unoccupied molecular orbitals in the domain with stronger hydrogen-bonds are shifted down 0.35 V overall with respect to the states in the domain with weaker bonding. Similarly, studies on BDATB, PTCDI and BDATB/PTCDI assemblies reveal that the intermolecular hydrogen-bonds may create dipoles within the bonding regime, thereby inducing shift of the molecular resonances in energy [108]. Based on these studies, we propose that the downshift of the LUMO and LUMO+1 of DCV5T-Me$_2$ within the organic islands originates from the intermolecular hydrogen-bonds and electrostatic interaction. Here, the value of the shift is nearly 1.0 V, which is three times bigger than the reported value (0.35 V) [19]. However, it is reasonable considering that in our system the transition is from the absence of bonding to the presence of a big amount of strong intermolecular interactions rather than from weaker bonding to stronger bonding.

We can use the quantum mechanism of "particle in a box" to explain the downshift of molecular orbital energy [112]. Strong intermolecular interactions benefit the orbital overlap between molecules. Consequently, the distribution of electrons are more delocalized over the two dimensional domain than within one single molecule. The bigger the size of the box, the lower the energy of the states. Therefore, islands possess orbitals with lower energies than a single molecule in our system.

To detect molecular states at higher energy level without destroying the organic molecules, we did STS with closed feedback loop. As shown in figure 2.7 c, another resonance of 2.35 V is localized at the center of the molecule, which is also revealed by the corresponding dI/dV mapping (figure 2.7 f). DFT calculations of the free molecule show that the LUMO+2 has higher weight at the central part with an energy 0.81 V above the LUMO+1. Hence, it is reasonable to assign the resonance

of 2.35V to the down-shifted LUMO+2 state upon assembly.
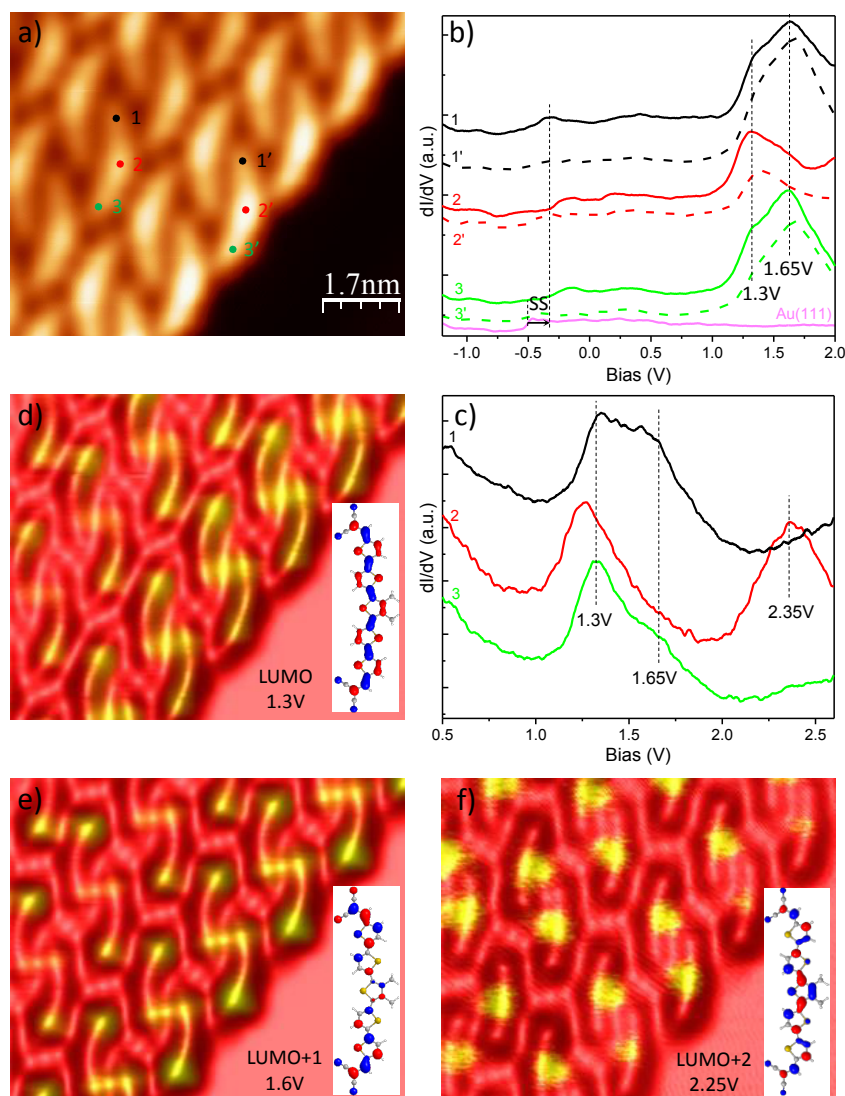
Figure 2.7: Electronic properties of molecular islands. a) STM image (I = 81 pA, V = 1.3 V) of a molecular island. b) dI/dV spectra acquired with open feedback (set point: I = 110 pA, V = -2 V) at different locations on the island as indicated in a. The surface state is shifted up around 0.2 V due to the change of work function by the attachment of the organic layer. c) dI/dV spectra acquired with closed feedback (set point: I = 50 pA, V = 0.5 V), which allows for spectra at higher bias voltage. The energetic positions of the resonances in the dI/dV spectra are highlighted by the black dash vertical lines, and all the spectra are offset for clarity. d) - f) Constant height dI/dV maps of the same island as in a recorded at biases of 1.3 V (81 pA), 1.6 V (81 pA) and 2.25 V (39 pA), respectively. In the maps the red color represents background, while the yellow stands for dI/dV signal. Insets show the calculated orbital shape of the LUMO, LUMO+1 and LUMO+2 of the free molecule.

2.5 Structural and Electronic Properties of the Second Layer

2.5.1 Decoupling of the Second Layer

DCV5T-Me$_2$ molecules start to form islands on top of the first molecular layer when coverage is increased over one monolayer, as shown in figure 2.8 a. The second layer consists of the same unit cell as the first layer. High resolution STM image (figure 2.8 b) shows that molecules become asymmetric within the second layer, with a big lobe connected to a small lobe by a node. After overlapping the bonding models of two layers, we found that the position of molecules within the second layer is not commensurate with the first layer (figure 2.8 b). It means that the growth of the second layer is not templated by the structure underneath. However, the asymmetric configuration should be attributed to the interactions between the two layers. It is expected that cyano groups and thiophene rings in the second layer rotate to interact with the thiophene rings and cyano groups in the first layer, respectively, due to molecular flexibility. This rotation would result in the asymmetric geometry.
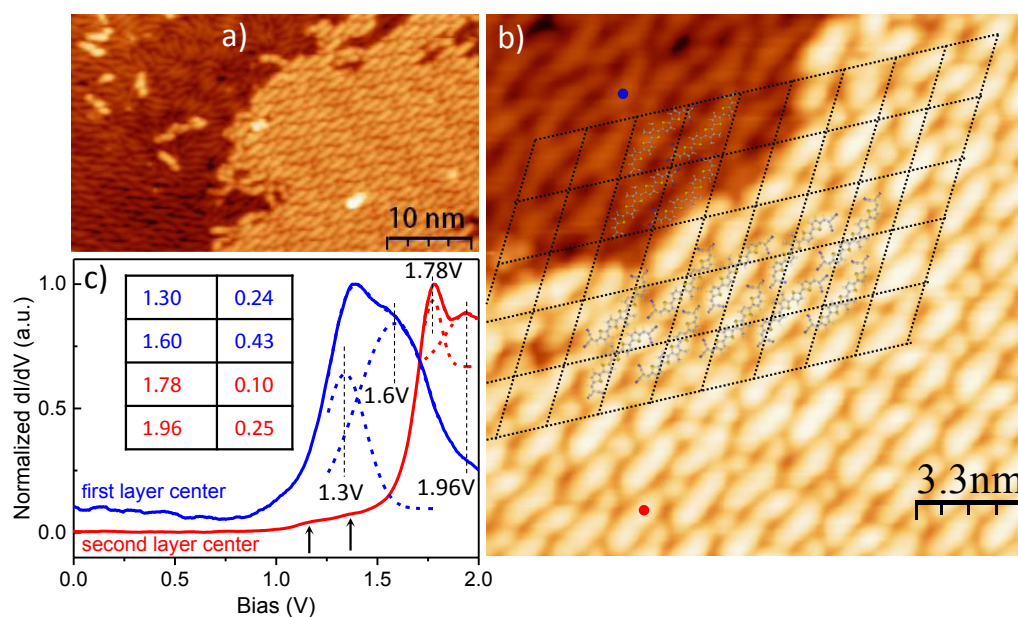
Figure 2.8: Structural and electronic properties of the bilayer film. a) Large scale STM image (I = 63 pA, V = 0.81 V) of a bilayer film of DCV5T-Me$_2$ on Au(111) showing a large ordered island located on top of the first layer. b) High resolution STM image (I = 24 pA, V = 0.63 V) of the bilayer film with a model for the structure superimposed. Every rhombus in the black dash grid surrounds a molecule in the first layer. c) Normalized dI/dV data (solid) acquired with open feedback (set point: I = 91 pA, V = -2 V) at the center of molecules within the first layer and the second layer and the corresponding Gaussian fits (dash). The energetic positions and the full-width-at-half-maximum (FWHM) values of the peaks are listed in the inset table with the unit of eV. The two black arrows under the red spectrum taken at the second layer indicate the states permeating from the first layer.

In order to inspect the evolution of molecular electronic properties with the layer growth, we performed spectroscopic measurements, as shown in figure 2.8 c. The molecule in the second layer possesses a resonance of 1.78 V, which is assigned to the LUMO state. The narrow width of the line shape and the higher lying in energy of this state with respect to the LUMO at the first layer (FWHM: 0.1 V vs. 0.24 V, energy: 1.78 V vs. 1.30 V) imply good decoupling of the second layer from the metal surface. However, the LUMO at the second layer is still lower in energy than that at the single molecule on the Au(111) surface. We attribute this to the existence of intermolecular interactions within the second layer and between the two layers, which shift down the molecular orbital as well. Note that the states around 1.3 V permeate from the first layer to the second layer, which induce a shoulder in the spectrum taken at the molecule within the second layer as indicated by the black arrows.

2.5.2 Vibronic Spectroscopy in the Second Layer

Interestingly, a satellite peak 0.18 eV above the LUMO in energy arises at the center of the molecule in the second layer (figure 2.8 c). From its location at the molecule and its distance to the LUMO in energy, the possibility of being LUMO+1 is ruled out. A reasonable origin of this peak is a vibrational state coupled with the LUMO resonance in a well decoupled organic layer from metal substrates. We will demonstrate this in the following content.

Vibronic Spectroscopy in STM
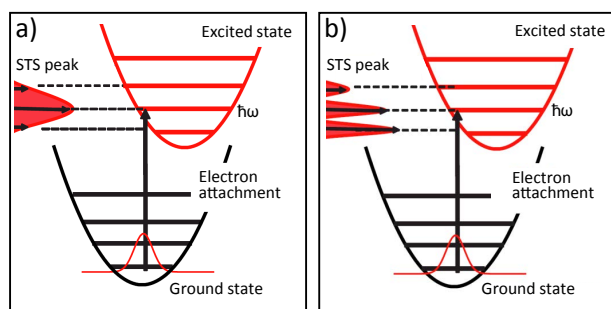
Figure 2.9: Images from [37]. a) Vibrational states are hidden in the broad line shape of molecular resonance, when molecules strongly hybrid with the metal surface, which induces extremely short lifetime of the excited state. b) Vibronic states can be detected as separate peaks in dI/dV spectra, when molecules are well decoupled from the metal surface, which induces longer lifetime of the excited state and sharper molecular resonance.

Before going to the experimental data, we first introduce the electron-vibration coupling briefly. In STM, the tunneling process through molecules can be treated as

transiently attaching an electron into an excited state (take tunneling into unoccupied orbitals as an example), then this electron decays into the substrate. When the energy of the electron exactly equals the energy difference between the ground state and the excited state, only transition between different electronic states occurs. If the electron carries more energy corresponding to a vibration mode, the molecular can be excited from its ground state to the excited electronic state associated with a vibrational excitation - the vibronic transition.

In the tunneling process, the width of the the molecular resonant state scales inverse with the electron lifetime. When organic molecules directly adsorb on top of a metal surface, the tunneling time scale is very short, so the width of the corresponding resonance is broadened. As a result, vibrational states are normally hidden by the broad line shape of the molecular resonance in STS, as shown in figure 2.9 a. In order to resolve vibrational peaks from the resonant state, organic molecules have to be decoupled from the metal surface for example by an insulating layer [27, 113, 114, 115] or by the first layer of organic molecules [116, 117]. The increased lifetime induces a sharper resonant peak. When its width is smaller than the vibrational energies, vibronic states can be detected as separate peaks in STS, as shown in figure 2.9 b.

Vibronic States of DCV5T-Me$_2$

The decoupling of DCV5T-Me$_2$ from Au(111) in the second layer offers the opportunity to detect molecular vibronic states with scan tunneling spectroscopy. Figure 2.10 shows three exemplary STS spectra at the sides and center of a molecule in the second layer and the corresponding Gaussian fits. Two peaks are distributed at the center, whereas the two sides possess four peaks with different intensities. Peak 1 at 1.78 V is assigned to the LUMO of the molecule, as has been discussed above. Peak 3 is 0.36 eV higher in energy than the LUMO. This energy perfectly matches DFT calculated energy difference (0.35 eV) between the LUMO and the LUMO+1 states. Therefore, we assign Peak 3 at 2.14 V to the LUMO+1 state [118]. This assignment is further confirmed by its spatial localization at only two sides of the molecule, as we observed in the DFT calculated distribution.

Peak 2 and Peak 4 present the same energy, 0.18 eV, above the LUMO and LUMO+1 states, respectively. Calculations suggest that Peak 4 is not derived by the LUMO+2 state, since LUMO+2, for the free molecule, appears at 0.81 eV above the LUMO+1 in energy. These facts indicate that Peak 2 and Peak 4 should be assigned to the vibrational states of DCV5T-Me$_2$. Actually, the vibration with energy of 0.18 eV (1450 cm^{-1} in frequency) has been detected with STM on oligothiophenes, corresponding to the C=C and C-C bonds stretching of the aromatic backbone [119]. So, we believe that here the same vibration mode is measured on the dicyanovinylene-substituted oligothiophenes. Moreover, spectra (black and green in figure 2.10) recorded at the two functional groups also exhibit vibronic peaks, meaning that this vibration mode

extends to the DCV groups. Note that the vibrational state lay in the middle of the LUMO and the LUMO+1 in energy, which brings difficulty to the assignment of the four peaks. Benefiting from the nonuniform distribution of the LUMO+1 state over the molecule, the peak at 2.14 V can be assigned to the LUMO+1 rather than the vibration with higher order, which is absent at the center of the molecule.
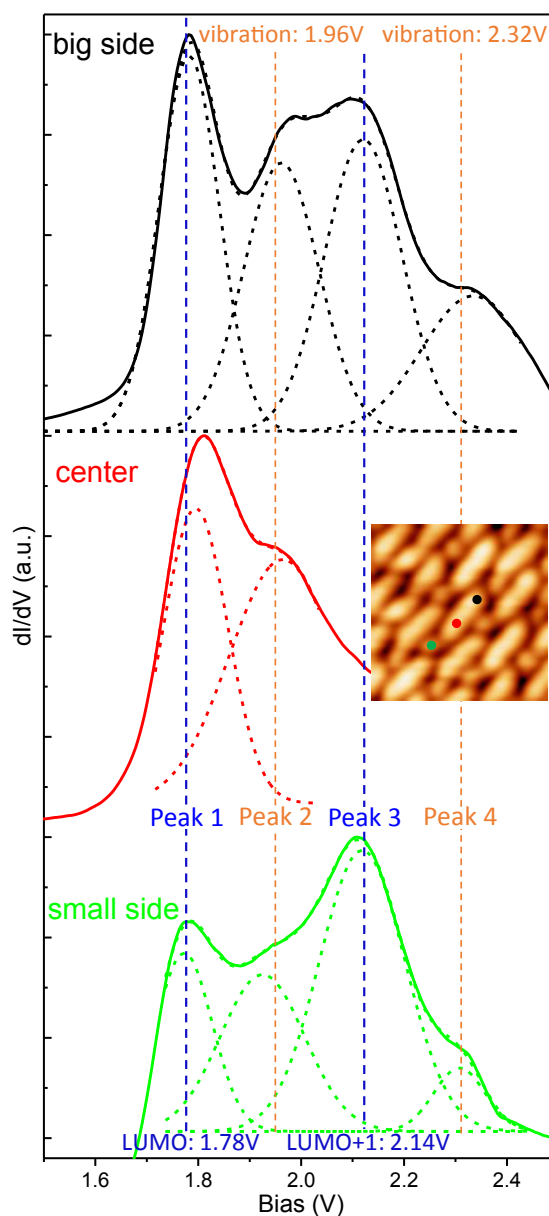
Figure 2.10: Three exemplary dI/dV spectra (solid) acquired with open feedback (set point: I = 70 pA, V = -2 V) at the sides and the center of a molecule in the second layer and the corresponding Gaussian fits (dash). In all the dI/dV spectra the energetic positions of the peaks are highlighted by the vertical dash lines. In particular, the blue dash lines indicate the electronic states, while the orange dash lines indicate the vibrational states. All the spectra are offset for clarity.

2.5.3 DFT Calculated Vibrations

Vibrational spectroscopies were calculated to gain theoretical supports for our experimental data. DFT calculations reveal that DCV5T-Me$_2$ molecule [2] has 159 vibrational modes. The bands below 1000 cm^{-1} are always related to a mixing of different in-plane vibrations or out-of-plane bending and folding modes, while the band of 2250 cm^{-1} corresponds to the C≡N vibrations [43]. More interestingly, in the Raman and IR spectra, bands in the range between 1000 and 1700 cm^{-1} offer structural information on the π-conjugated molecular backbone [43]. As shown in figure 2.11, a local strongest vibrational band is localized at 1446.85 cm^{-1} in the Raman spectrum, corresponding to 0.1794 eV in energy. The calculated IR spectrum exhibits the strongest vibrational band at the same energy (frequency). This calculated energy is in good agreement with the value measured in our STS data.
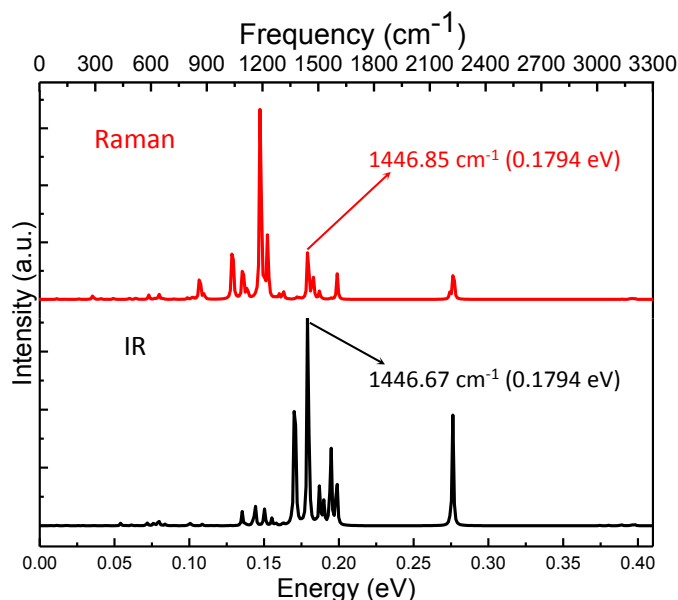
Figure 2.11: DFT calculated Raman spectrum (upper panel) and infrared spectrum (lower panel) of the DCV5T-Me$_2$ molecule charged with one electron in gas phase.

The eigenvectors associated with the strongest vibrational bands are represent in figure 2.12 [3]. The vibrational mode with energy of 0.1794 eV in Raman (IR) spectrum describes the totally symmetric (anti-symmetric) in-plane stretching of the C=C and C-C bonds over the whole molecular backbone. Both vibrational modes involve the movements of carbon atoms on the whole molecular backbone including the oligothiophenes and the DCV groups. This calculated result matches with the STS measurements very well. The vibrational satellite peaks follow the distribution

---

[2]Because in STS measurements molecules are at excited state due to the attachment of one tunneling electron, here we calculate vibrations in negatively charged DCV5T-Me$_2$ with one electron.

[3]Hydrogen atoms and their movements are not shown in the vibrations.

of the orbitals, by which they are excited. Therefore, we conclude that the satellite peaks of 0.18 eV higher than the molecular resonances in STS are induced by either symmetric or anti-symmetric stretching of the C=C and C-C bonds over the whole molecular backbone.

The calculated data are based on the free molecule in gas phase and the reported experimental data [119] correspond to the single molecule on an insulating layer on Cu(111). Our data were measured on the molecule within an organic film, where strong intermolecular interactions exist. However, comparisons show that the vibrational mode with energy around 0.18 eV not only exists at the free and isolated molecule but also survives at the molecule within self-assembled organic film. It means that the stretching of C=C and C-C bonds is not influenced by the intermolecular interactions.

a) 1446.85 cm⁻¹ (0.1794 eV)

b) 1446.67 cm⁻¹ (0.1794 eV)
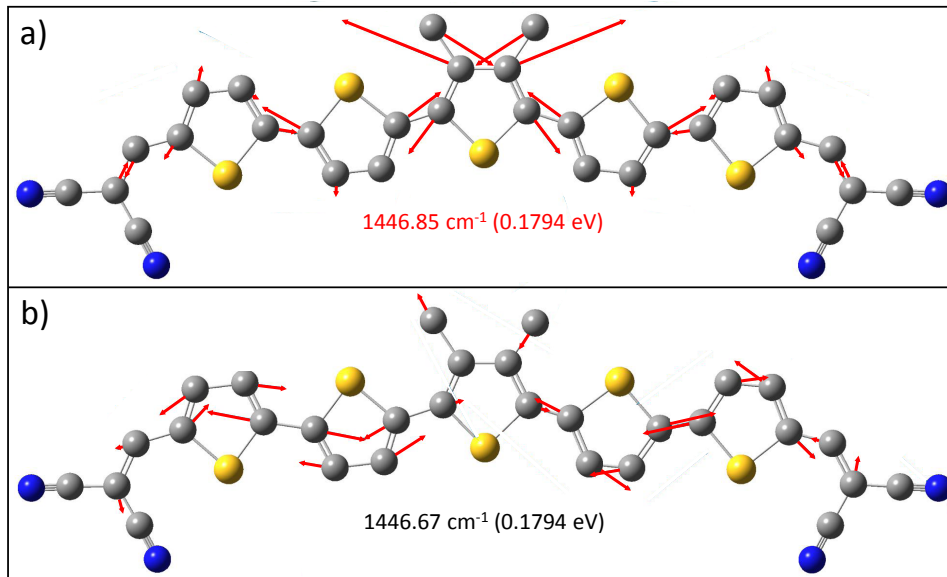
Figure 2.12: DFT calculated eigenvectors (atomic vibrational displacements) for the modes corresponding to the strongest Raman spectrum band a) and infrared spectrum band b).

This vibration mode plays an important role in the charge transfer process in blends of DCVnTs polymer and fullerene. Recent studies [110] demonstrated that the strong coupling between polymer vibrational state of C=C and C-C stretching at 1450 cm⁻¹ and fullerene vibration of pentagonal pinch mode at 1470 cm⁻¹ triggers and mediates a coherent charge transfer from the polymer to fullerene. Calculations show that charge transfer is inhibited if vibrations are frozen by clamping the thiophene backbone [111]. The match of vibronic states of DCVnTs and C₆₀ in energy contributes to the high performance of organic solar cells based on their mixture. Therefore, molecular vibrations are necessary and significant for the charge transfer in organic electronics. Here, we show that the electron-vibration coupling during charge transport through organic films can be detected with sub-molecular resolution by using STM/STS.

2.6 Conclusions

Figure 2.13 summarizes the evolution of structural and electronic properties of DCV5T-Me$_2$ on Au(111) with coverage. AFM imaging reveals the assembly structure of the molecule on the metal surface. For packing in two dimensions on Au(111), molecules self-assemble into organic islands through intermolecular hydrogen-bonds, and also strong electrostatic interaction that induces high thermal stability to the pure organic domains. Molecules in the second layer adopt asymmetric configuration lying over the first layer with different orientations, while they pack in the similar structure with that underneath.

Electronic properties vary accordingly. Unoccupied molecular orbitals within islands are energetically shifted down by intermolecular interactions with respect to the single molecule on Au(111). Molecules within the second layer have sharper and higher-lying resonances compared with molecules in the first layer due to being well decoupled from the metal surface. Consequently, a vibrational state coupled with both the LUMO and LUMO+1, with energy around 0.18 eV, was observed, which corresponds to the stretching of C=C and C-C bonds over the whole molecular backbone. By comparing with DFT calculations of the free molecule, it is determined that this vibration mode is not influenced by the strong intermolecular interactions.

These results demonstrate that, differently from oligothiophenes, structural and electronic properties of dicyanovinylene-substituted oligothiophenes strongly vary with its chemical environments, which should be taken into account during designing organic electronics based on this family of molecules.
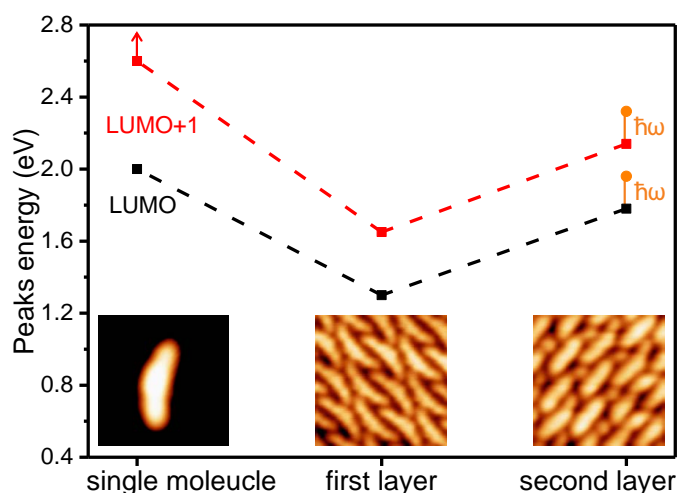

Figure 2.13: Evolution of structural and electronic properties of DCV5T-Me$_2$ molecule on Au(111): from single molecule to bilayer molecular film.

3 Structural and Electronic Properties of Complexes Based on DCV5T-Me$_2$ on Au(111)

3.1 Introduction

The combination of organic linkers with metal atoms on metal surfaces offers fascinating perspectives for functional electronic and magnetic nanoscale devices. Some organic ligands are very active, so that they can bond to metal adatoms directly from the metal substrate and form metal-organic nanostructures [120, 121, 122, 123] or even meditate the complete reconstruction of the metal surface underneath [124, 125, 126, 127, 128]. The incorporated metal atoms modify the alignment of localized and degenerated orbitals locally and lift their degeneracies by step-wise metal-ligand hybridization [39, 129], as shown in figure 3.1. Recent works on insulating surfaces tracked precisely the effect of metal atoms on the molecular orbital structure [40, 130, 131], which in many cases induces a renormalization of molecular states that can be described as the linear combination of free-molecule orbitals, as shown in figure 3.2. Whether this simple picture still applies on a metal-organic interface is still unknown.

Structural and electronic properties of chains of DCV5T-Me$_2$ self-assembled on Au(111) simultaneous with the organic islands (see section 2.2) are studied in the first part of this chapter. AFM imaging reveals that the chains are formed through incorporation of Au adatoms by cyano groups from the surface. Then, a site-specific influence of the coordination on the molecular orbital energy alignment and spatial distribution is determined by STS with the combination of DFT calculations.

Another typical source of metal atoms in metal-organic architectures is external deposition [3, 8, 132, 133, 134, 135, 136, 137, 138]. In particular, Na atoms can be extracted by ligands from NaCl islands on metal surfaces to form metal-organic complexes[139, 140]. The results of co-deposition of NaCl with DCV5T-Me$_2$ are represented in the second part of this chapter. The pre-formed organic islands and chains with Au adatoms are transformed into long and parallel chains with Na-CN bonding. The statistics of coverage dependence of inter-chain distances reveals an inter-chain long-range repulsive potential induced by intra-molecular charge transfer.

Hybrid molecular systems, built from combination of two types of molecules, are
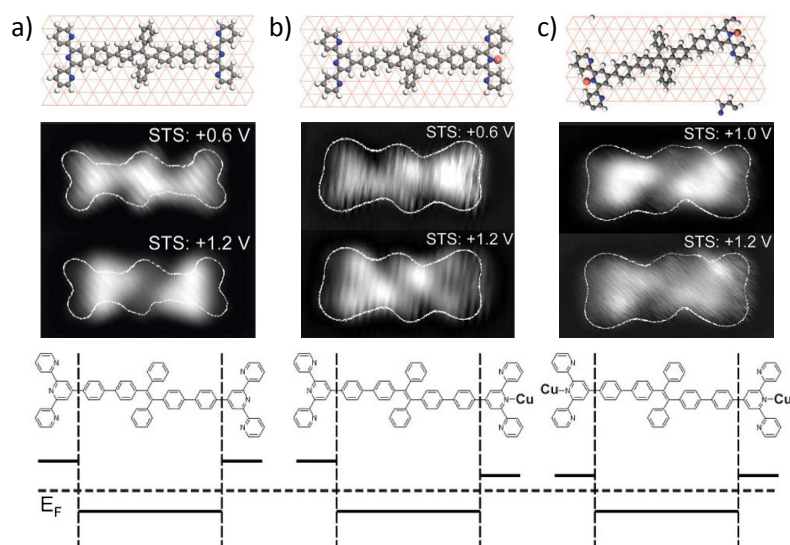
Figure 3.1: Images from [39]. Upper column: DFT optimized a) single molecule, b) molecule with one Cu atom at one side and c) molecule with two Cu atoms at both sides, respectively, adsorbed on one layer of Cu atoms. Middle column: STS maps acquired at the indicated bias voltages. The molecular contour of the STM topography (white line) is overlaid on the STS maps. Image size is 50 Å by 25 Å. Bottom column: scheme showing the realignment of the localized molecular orbitals by single-atom contacts.
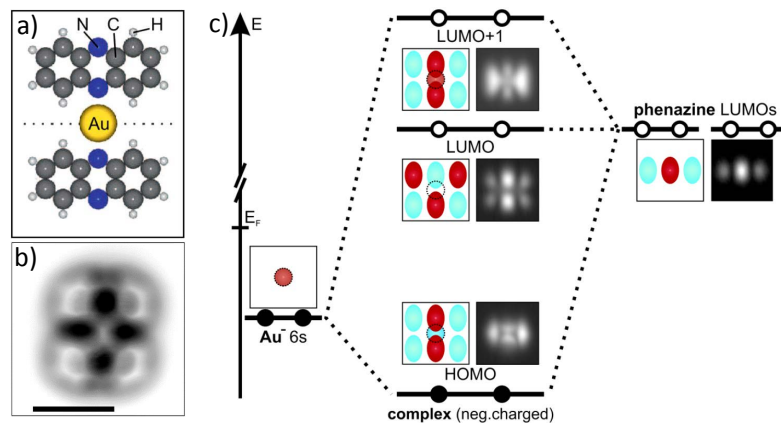
Figure 3.2: Images from [40]. a) and b) Model and constant-height AFM image of the phenazine-gold-phenazine complex on NaCl on Cu(111), respectively. c) Schematic level diagram and basic orbital model. Light blue and dark red indicate different signs of the wave function. The black-white images show the shape of orbitals from measurements. The three constituents' orbitals being combined are the Au 6s state (left) and two unoccupied phenazine LUMOs (right). Due to the complex's symmetry, only the phenazine LUMOs couple to the complex's LUMO. The Au 6s contributes to the complex's HOMO and LUMO+1.

of great interest due to the structural and electronic properties of the components can be modified by the intermolecular interactions, like the charge transfer effect

[18, 141, 142, 143]. The charge transfer mechanism dominates the performance of organic electronics, especially organic solar cells. Recently, organic solar cells composed of several tens of nanometers of mixed films of DCVnTs and C$_{60}$ have been extensively studied with average techniques [42, 43, 44, 45, 46, 47, 48, 49, 104]. However, very little is known about the thin-film behavior in sub-molecular level. Therefore, we attempt to mix DCV5T-Me$_2$ molecules with C$_{60}$, coronene and tetra-cyanoquinodimethane (TCNQ) on Au(111), in order to get a charge transfer system. Unfortunately, the strong intermolecular interactions and coordination bonding with Au atoms, hinder the ordered mixing with other types of molecules. The corresponding results are shown in the third part of this chapter.

3.2 Gold-adatom-mediated Bonding and Molecular Orbital Redistribution in Metal-organic Chains

3.2.1 AFM Imaging Bonding Geometry of Chains

As has been shown in section 2.2, the deposition of sub-monolayer amounts of DCV5T-Me$_2$ on Au(111) at room temperature leads to the formation of extended molecular chains simultaneous with organic islands. The chains are bi-molecular linear structures linked by a characteristic motive. This bonding geometry is missing in bulk. High resolution STM image (figure 3.3 a) shows that the linking motive is a bonding node of four molecules pointing their cyano terminations towards each other. Such a bonding configuration is highly unfavorable for the bare electronegative nitrogen terminations, unless a cementing metal atom coordinates to them. Thus, we consider that Au adatoms are trapped and incorporated into the DCV5T-Me$_2$ chain structures at room temperature *via* coordination bonds with the cyano moieties of DCV5T-Me$_2$ [123].

To prove the incorporation of Au atoms and the bonding geometry of the coordinated structure, we measured the chains with atomic force microscopy. Figure 3.3 b shows a Laplace-filtered AFM image of the same chain as in figure 3.3 a acquired at constant height mode. The molecular structure can be unambiguously identified from the Δf map, which is the same as that in the islands. The AFM image also confirms the four-fold motives formed by four DCV groups around one common point. Focusing on the linking four-fold motifs, a rounded protrusion appears between the four cyano groups when imaged at closer tip-sample distance (figure 3.3 d). This protrusion is unambiguously assigned to the Au atom bridging the four negatively charged cyano groups. Moreover, the four cyano groups are located around the Au adatom following a four-fold bonding arrangement, supporting that the Au adatom uniformly bonds to the four surrounding molecules (figure 3.3 c).

It is well known that mobile Au adatoms exist on the Au(111) surface even at 80K [144], so they can be easily incorporated by the organic ligands at room tempera-
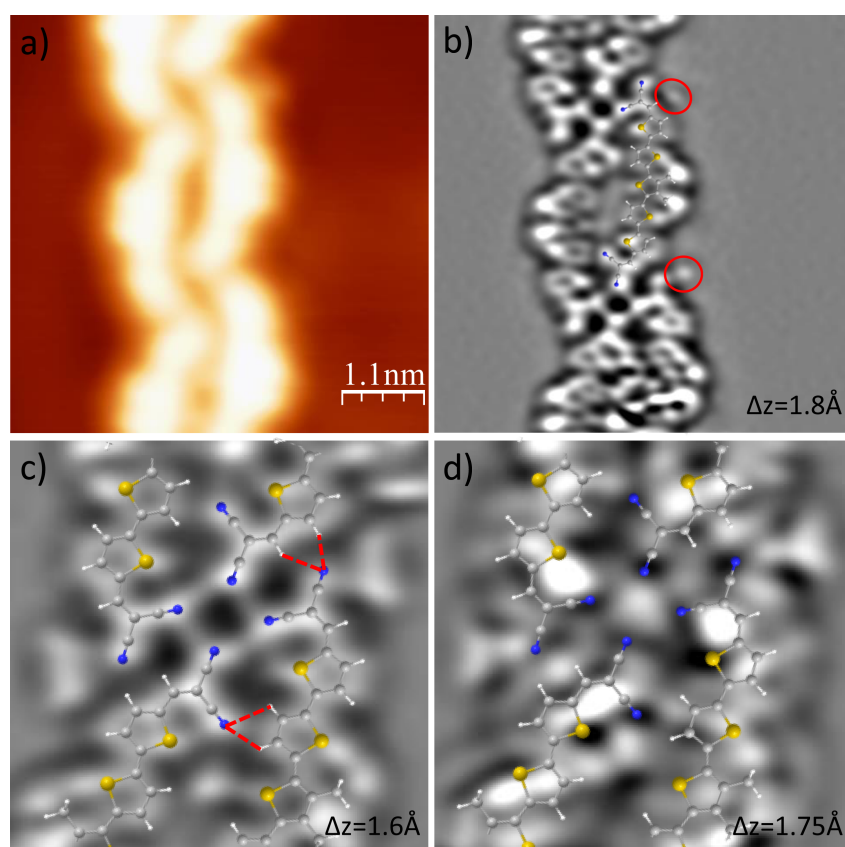
Figure 3.3: Real-space imaging the Au atom and bonding geometry in coordination bond within chains. a) High-resolution STM image (I = 15 pA, U = 0.1 V) of a chain recorded with a Xe-functionalized tip at constant current mode. b) Laplace filtered AFM image of the same chain superimposed by a molecule model, plotting the amplitude of the frequency shift while scanning at constant tip-sample height. The tip was approached by 1.8 Å towards the sample from an initial position set by the control parameters of I = 15 pA and U = 0.1 V over the molecule. The red circles highlight two Xe near the chain. c) and d) Laplace filtered AFM images of the joint of four adjacent molecules around one Au atom. The tip was approached by 1.6 Å (c) and 1.75 Å (d) towards the sample (I = 21 pA, U = 0.11 V) over the molecule, respectively. Images c and d are recorded with the same tip, which is different from the tip for image b acquisition. The size of images in c) and d) is 2.45 nm × 2.45 nm. Intermolecular hydrogen-bonds should also exist, as indicated by the red dash lines (c).

ture [121, 124, 126]. Recently, studies have demonstrated that F4TCNQ molecules, which have the same di-cyano functional group as DCV5T-Me$_2$, can form coordination bonds with Au adatoms on the Au(111) surface [123]. Therefore, we believe that DCV5T-Me$_2$ molecules pick up mobile Au adatoms from the surface at room temperature and self-assemble into four-fold metal-organic chains. Usually, it is only possible to determine the existence of the metal cores and the bonding structure in the coordination through electronic states measurements with STS, while they are invisible in STM images [122, 135]. Here, we resolve the metal atoms and the exact bonding geometry in the coordination in real-space through AFM imaging [40].

Besides the coordination, intermolecular hydrogen-bonds also exist between cyano groups and hydrogen atoms in the adjacent thiophene rings, as indicated by the red dash lines in figure 3.3 c. Each one molecule possesses four hydrogen-bonds in the chains. However, these bonds should not be strong, since the involved hydrogen atoms are out of the extension direction of the lone-pair electrons localized at the nitrogen atoms (the hydrogen atoms are not in the line of the C≡N). Therefore, it is expected that the coordination bond drives the formation of the chains and dominates their electronic properties.

3.2.2 Downshift of the LUMO in Both-side Coordinated Molecule

To determine the effect of the cementing Au adatoms on the molecular functionality, we studied their electronic configuration by means of STS. As a reference, spectra on the individual DCV5T-Me$_2$ monomer are shown here as well (figure 3.4 a and b). For easier description, we label its LUMO resonance at 2.0 V as P1.

The incorporation of Au atoms modifies the resonance structure of the DCV5T-Me$_2$ molecules. Bottom panel of figure 3.4 b shows STS spectra recorded on different positions within the chain structure indicated in figure 3.4 c. We find that the new LUMO state is a resonance centered at 1.3 V (P2). This state is observed with larger weight on the sites closer to the Au atoms, as pictured in dI/dV maps (figure 3.4 d). On top of the Au atom, the state appears centered at 1.5 V (P3) suggesting that this corresponds to a metal-atom-derived localized state [135]. In fact, the dI/dV map recorded at 1.6 V (figure 3.4 e) allows to resolve the position of individual Au adatoms incorporated in the self-assembled chains, otherwise not visible in the STM topographic images (figure 3.4 c). The dI/dV map taken at 2.0 eV, energy of the LUMO at uncoordinated molecules, shows no feature at the metal-organic chain (figure 3.4 f). The downshift of the LUMO state from 2.0 V to 1.3 V, and its localization at the terminal groups, are ascribed to the effect of hybridization with Au adatoms, presumably mixing N lone-pair 2p electrons of cyano groups with Au 6s electron of gold adatoms [39, 123, 129, 135, 145].

3.2.3 Redistribution of Orbitals in One-side Coordinated Molecule

Metal dopants, therefore, modify the functionality of molecular films, even on weakly interacting substrates. The redistribution and localization of electronic states induced by coordination to Au atoms may affect exciton mobility, whereas, orbital energy shifts modify energy level alignment at the interfaces. However, in real molecular devices, molecules pack in films with geometries different than the ordered chain structure, such as molecules asymmetrically bonded to the metal.
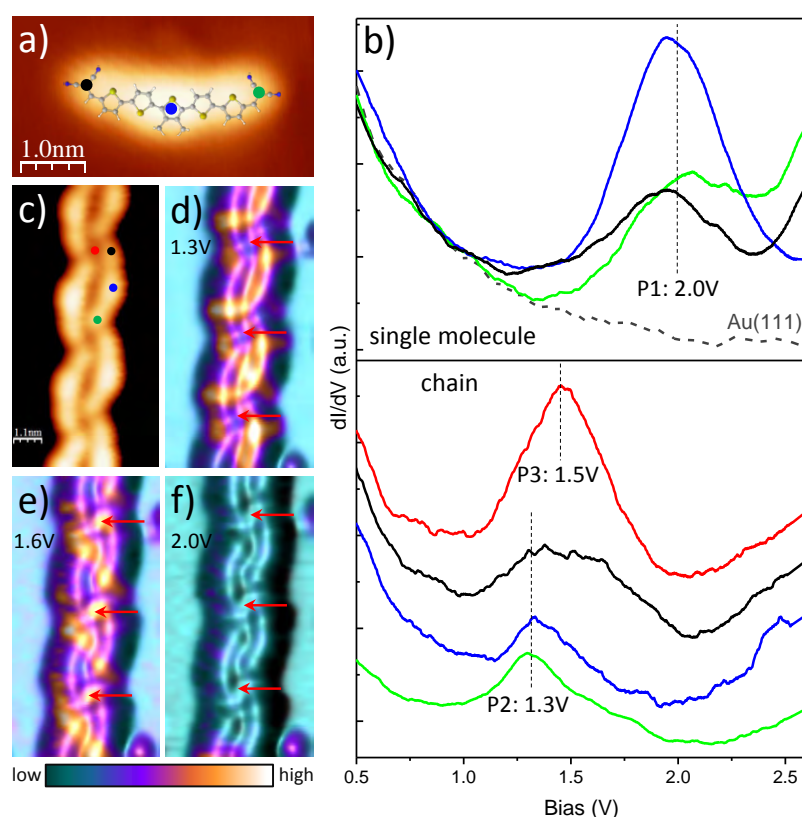
Figure 3.4: Electronic structure of a molecule coordinated within a chain. a) STM image (I = 67 pA, U = 0.89 V) of a single molecule on Au(111), with a DFT optimized configuration superposed. b) dI/dV spectra acquired with closed feedback at different locations on the single molecule (upper panel, set point: I = 50 pA, U = 0.5 V) and on the molecule within a chain (bottom panel, set point: I = 34 pA, U = 0.2 V), at sites indicated in a) and c), respectively. The energetic positions of the resonances in the dI/dV spectra are highlighted by the black dash vertical lines. Spectra on the coordinated molecule are offset for clarity. c) STM image (I = 22 pA, U = 0.80 V) of a chain. d) - f) Corresponding dI/dV maps at the energies of the resonances of the coordinated molecules in chains (d), of the Au adatoms (e), and of the single molecule (f), that is, at 1.3 V, 1.6 V and 2.0 V (I = 79 pA), respectively. In d) - f) the dI/dV signals (bright) are overlapped on top of a top-illuminated STM topography. The red arrows indicate the positions of the Au atoms incorporated in the chain.

To explore the effects of asymmetric bonding to metal atoms, we extend our analysis to molecules at the ends of the molecular chains, as shown in figure 3.5. Terminal DCV5T-Me$_2$ molecules in the chain bonding to only one Au adatom at one side, while they expose an uncoordinated DCV end-group at the other [1] (figure 3.5 a). The effect of such asymmetric coordination pattern is reflected in the electronic configuration. In figure 3.5 b, we compare STS spectra taken over both molecular ends. At the coordinated side of the molecule, the first unoccupied resonance appears at 1.4

---

[1] The far distance between the two end DCV groups from the two terminal molecules indicates that no Au atom is incorporated there.

V (P2) similar with the symmetrically coordinated case, whereas the uncoordinated side shows only a higher-lying resonance at 2.2 V (P4). This asymmetric resonance redistribution is reflected in the spatially resolved spectroscopic maps at the corresponding resonance voltages. At 1.3 V, the dI/dV signal is localized at the joints of cyano groups, corresponding to the position of Au adatoms and coordinated DCV groups (figure 3.5 d). In contrast, the spectroscopy map at 2.2 V (figure 3.5 e) shows dI/dV signal only at the free sides of the terminal molecules. These dI/dV maps corroborate the fact that the molecular orbital alignment and spatial distribution within individual molecules are strongly modified by metal-ligand coordination.
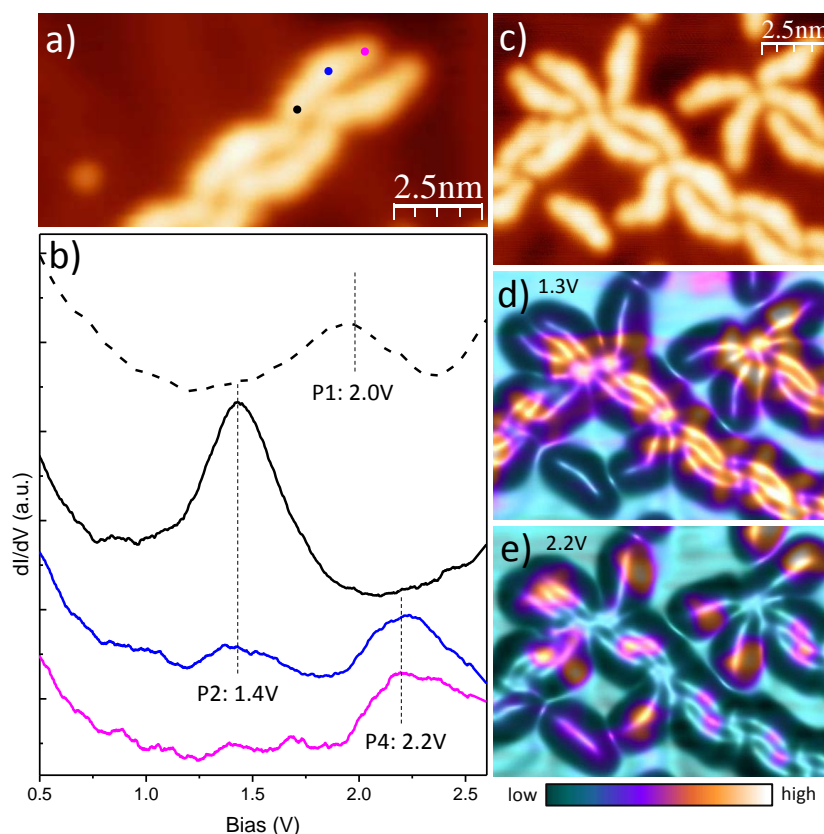
Figure 3.5: Electronic structure of a one-side-coordinated molecule. a) STM image (I = 24 pA, U = 0.71 V) of a chain termination showing two molecules without coordination bonds at the end. b) dI/dV spectra acquired with closed feedback (set point: I = 34 pA, U = 0.2 V) at different locations on the end molecule as indicated in a). The black dash spectrum taken at one side of the single (uncoordinated) molecule is shown here as a reference. The energetic positions of the resonances in the dI/dV spectra are highlighted by the black dash vertical lines, and all the spectra are offset for clarity. c) STM image (I = 50 pA, U = 0.80 V) of chains with only one-side-coordinated molecules at the ends. d) and e) Corresponding dI/dV maps at the energies of the resonances of the coordinated sides and free sides of the terminal molecules, that is, at 1.3 V and 2.2 V (I = 50 pA), respectively. In d) and e) the dI/dV signals (bright) are overlapped on top of a STM topography.

3.2.4 Dissociation of the Coordination Bond

Actually, at relative lower coverage, three-fold chains emerge [2]. Figure 3.6 a shows a three-fold metal-organic chain with a half-coordinated molecule at the end. Note that the end molecule is different from molecules within the chain in configuration. It adopts a metastable configuration with all the five thiophene rings oriented to the same direction and without S-CN interactions. However, DFT calculations (figure 3.7) demonstrate that this configuration has similar frontier molecular orbitals, both in structure and energy, with the most stable configuration.
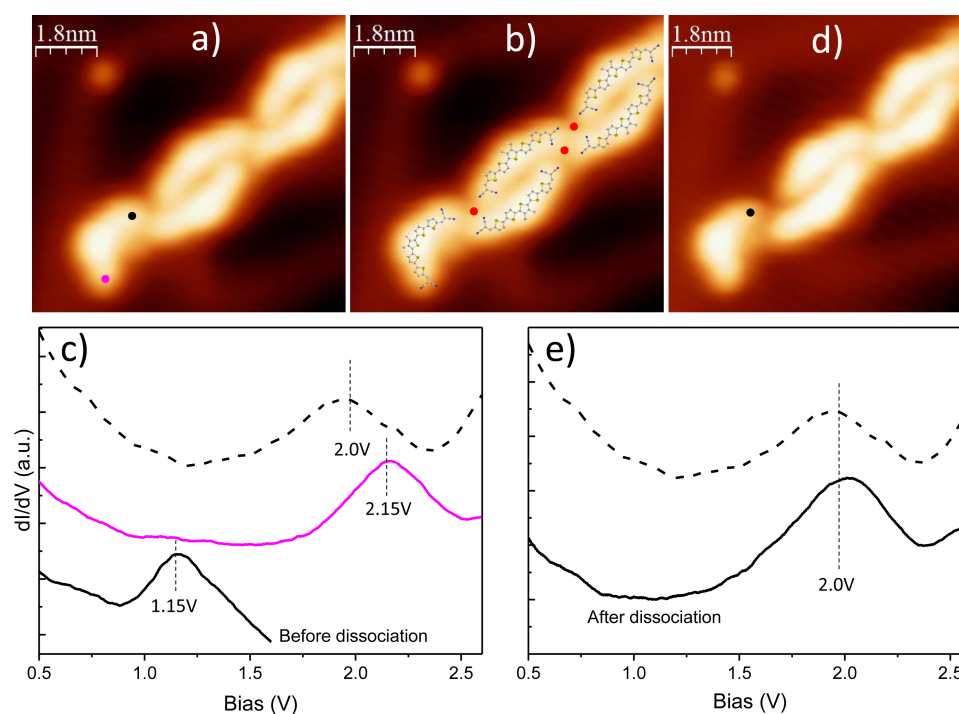
Figure 3.6: Dissociation of the coordination bond. a) STM image (I = 59 pA and V = 0.80 V) of a three-fold metal-organic chain with a half-coordinated molecule at the end. b) Model for the end structure. Red circles represent Au atoms. c) dI/dV spectra acquired with closed feedback (set point: I = 50 pA and V = 0.2 V) at different locations on the end molecule as indicated in a). The black dash spectrum recorded at one side of a single molecule is shown as a reference. The coordination bond was dissociated by high-energy electrons during taking spectrum (black solid spectrum in c) at the coordinated side (the fussy part due to bond dissociation is not shown here). d) STM image taken at 49 pA and 0.56 V after dissociation of the coordination bond. e) Spectrum (black solid) taken at the previous coordination side after the dissociation. The energetic positions of the resonances in the dI/dV spectra are highlighted by the black vertical lines, and all the spectra are offset for clarity.

---

[2]For three-fold chains, one molecule possesses one Au atom (figure 3.6 b). While one molecule within four-fold chains occupies half Au atom. Therefore, the transformation from three-fold to four-fold with coverage is attributed to the Au-atom/DCV5T-Me$_2$ ratio. When molecules are excess compared with the metal atoms, four-fold metal-organic chains are formed (simultaneous with organic islands assembled by the extra molecules).

STS measurements show that the uncoordinated side of the end molecule has a resonance at 2.15 V, whereas the coordinated side possesses a lower-lying resonance at 1.15 V. Based on the discussion above, they can be assigned to the new LUMO+1 and LUMO modified by the coordination [3], respectively.

Moreover, the fact that orbitals are spatially modified at the end molecule, where intermolecular hydrogen-bonds are missing, proves that the modification of molecular orbitals in four-fold chains (weak hydrogen-bonds exist there) is indeed induced by coordination rather than hydrogen-bonds.

The coordination bond was dissociated by high-energy electrons during taking spectrum at the coordinated side. Figure 3.6 e shows the spectrum after bond dissociation. The possession of a resonance at 2.0 V coinciding with the LUMO energy of the uncoordinated molecules and the STM image taken after spectra (figure 3.6 d) manifest the intactness of the end molecule after dissociation. The absence of the resonance at 1.15 V after coordination dissociation rules out the possibility that the low-lying resonance at the coordinated sides of the molecule is derived from the extension of Au-atom state rather than from the modification of the molecular LUMO state.
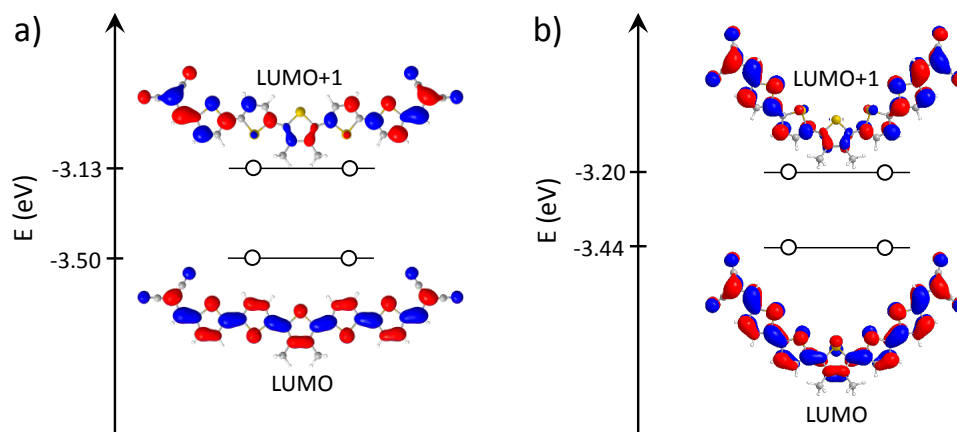
Figure 3.7: DFT calculated structure of molecular orbitals. a) The most stable configuration. b) The bent configuration.

3.2.5 DFT Calculations of Metal-organic Complexes

The origin of the resonance splitting and redistribution cannot simply be explained by a bare orbital shift (figure 3.1). As recently reported (figure 3.2), coordination to Au atoms enables the mixing of molecular states with gold orbitals. To determine

---

[3]Resonances in the molecule with three-fold coordination are lower in energy with respect to the four-fold case, which can be tentatively ascribed to the different strength of metal-ligand hybridization due to different bonding geometry [146]

Figure 3.8: DFT calculations of the Au/DCV5T-Me$_2$ complex with two Au atoms. a) The relaxed structure. The grey circles represent Au atoms. The distances between Au atoms and nitrogen atoms from the molecule are 2.2 Å, which are within the range of coordination bond length. b) Schematic diagram of the calculated energy levels and density of states of the orbitals participating in the formation of the metal-ligand complex. Unoccupied and occupied states are represented by open and filled circles, respectively.

the degree of orbital mixing in these systems, we have carried out DFT calculations of molecular orbitals and charges for (i) an isolated molecule and for a molecule coordinated with (ii) one Au atom and (iii) two Au atoms. Due to the weak interaction of the supporting Au(111) substrate with the DCV5T-Me$_2$ molecule [29] and the negligible spatial overlap between adjacent molecules, these results reproduce the main trends observed in our experiments. DCV5T-Me$_2$ has four non-equivalent cyano groups, which are labeled as 1, 1$'$, 2 and 2$'$ in figure 3.8 a. To simulate the experimentally determined bonding structure, we calculated a metal-organic complex with two Au atoms bonded at sites 1 and 2$'$. The energy optimized structure reproduces a CN-Au bond length of 2.2 Å, which is characteristic for coordination bonds [3]. Similarly, the complex with only one Au atom (located at site 2$'$, figure 3.9 a) possesses a coordination bond with bond length of 2.3 Å. Hence, our simulations reproduce the chemical reactivity of CN end-groups to form a local bond with gold atoms.

We look first into the effect of the metal-organic bond on the orbital structure of the

complex with two Au atoms. Figure 3.8 b presents the calculated energy levels and spatial distribution of atomic and molecular orbitals around the chemical potential. The LUMO and LUMO+1 of the isolated molecule interact with the 6s states of the gold atoms, resulting in a set of new orbitals (central column of figure 3.8 b). The states with the lowest energy are two singly occupied orbitals (SOMO) localized at the gold atoms (regarded as the zero point of the system) and mainly with Au(6s) character. Above them, other states exhibit the symmetry and characteristic nodal structures of the LUMO and LUMO+1 orbitals of the isolated molecule, with a down-shifted energy alignment. The coordination bond with the gold atoms is weak, amounting to 284 meV. A Mulliken analysis of the charge distribution shows no significant charge transfer between the Au atoms and the molecule, but just some charge redistribution within individual molecules.
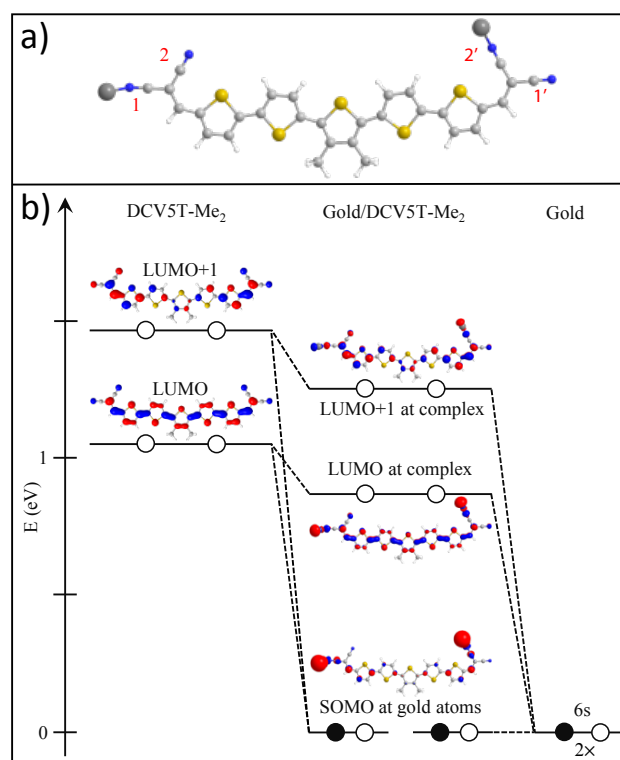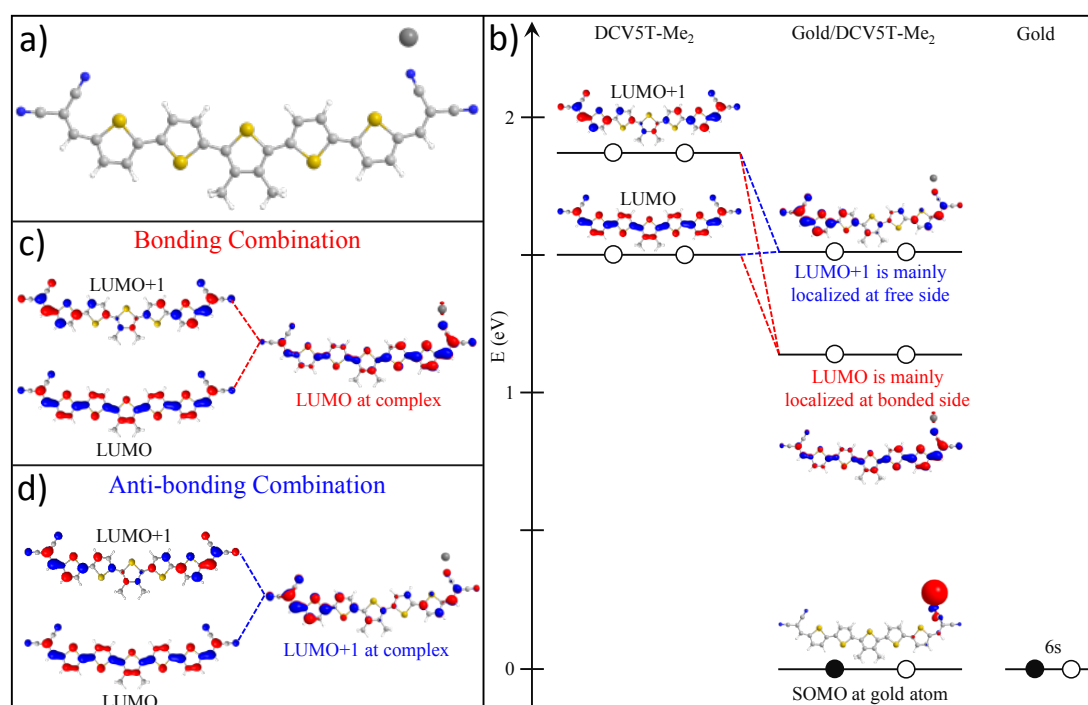

Figure 3.9: DFT calculations of the Au/DCV5T-Me$_2$ complex with one Au atom. a) The relaxed structure. The grey circle represents the Au atom. The distance between Au atom and nitrogen atom from the molecule is 2.3 Å. b) Schematic diagram of the calculated energy levels and density of states of the orbitals participating in the formation of the metal-ligand complex. Unoccupied and occupied states are represented by open and filled circles, respectively. c) and d) The new LUMO and LUMO+1 orbitals with asymmetric shape at the complex originate from the bonding combination and anti-bonding combination of the original LUMO and LUMO+1 orbitals of the molecule, respectively.

For the case of bonding to only one single Au atom, the simulations reproduce the asymmetric spatial distribution of the molecular states. Figure 3.9 b shows the calculated energy levels and orbital amplitude isosurfaces for the complex with only

one Au atom bonding to the 2$'$ site. Three new orbitals are generated at the metal-molecule complex from the two original orbitals at the molecule and the Au(6s) state (central column of figure 3.9 b). The SOMO state near the zero point energy is localized at the Au-N node. We also find here no significant charge transfer between the Au atom and the molecules, and an overall energy down shift of the renormalized LUMO and LUMO+1 states, in consistency with the experimental case. However, now the states show a clear asymmetry in the orbital shape: the new LUMO appears localized around the molecular end contacting with Au atom, whereas the new LUMO+1 state shows larger intensity at the opposite side of the metal-ligand bond.

We note that for the free, uncoordinated molecule, the LUMO is mirror symmetric with respect to the center of the molecule, whereas the LUMO+1 is anti-symmetric (figure 3.9 c and d). Hence, the renormalized molecular states necessarily involve the mixture of free-molecule states to adapt themselves to the new geometry. This can be interpreted at the very basic level as a linear combination of free molecular orbitals. Comparing the orbital shapes from figure 3.8 b, the splitting of the original LUMO into two asymmetric states is then described by the respective addition and subtraction of some weight of the original LUMO+1 to (figure 3.9 c) and from (figure 3.9 d) the free LUMO.

To confirm the orbital mixing, we have calculated the projected density of states (PDOS) of complex with one Au atom onto the free molecular orbitals [4], as shown in figure 3.10. Indeed, both the LUMO (blue) and LUMO+1 (red) from the free molecule contribute to the formation of the new LUMO at the complex. The same is true for the new LUMO+1 orbital. These results definitely demonstrate that the linear combination of free molecular orbitals results in the new set of states with a spatial distribution adopting the symmetry of the singly coordinated molecule. We note that the calculation also shows the mixing of the Au states with the molecular orbitals (HOMO-1: gray, LUMO: blue and LUMO+1: red), which contributes to the metal-organic coordination bond formation.

Studies have reported that metal atoms can bridge and induce overlap of two LUMO orbitals from two molecules [40]. In that case, the orbital structure is modified globally and symmetrically. Our results suggest that asymmetric metal atom attachment can even trigger mixing of orbitals belonging to one individual molecule, resulting in a spatial redistribution of the molecular electronic structure. Furthermore, different electronic properties of molecules with zero, one and two coordination bonds depicts a tuning strategy to manipulate the orbital character of molecular films by site-specific doping with metal atoms.

---

[4]The calculation was performed by Dr. Roberto Robles from Campus UAB, Spain. VASP program package and B3LYP exchange-correlation functional are used for the calculation, without considering the metal surface. In the calculation, peaks are not normalized, so it is difficult to gain quantitative values in the orbital mixing. However, major trends for the orbital renormalization can be clearly shown.

It is also interesting to compare the electronic properties of metal-organic chains with those in organic islands. The unoccupied molecular orbital alignments are shifted down within both structures by metal-ligand coordination and intermolecular interactions, respectively. However, the modification in space is significantly different. The interactions are not symmetrically applied to two sides of one molecule within islands from its neighbors (figure 2.5 b), but the molecular states at two sides are symmetrically modified (figure 2.7 d, e and f). Even molecules located at the edge of islands, where some intermolecular interactions are missing at one side, exhibit the same symmetric feature as molecules within islands (figure 2.7 d, e and f). In contrast, orbitals are renormalized into asymmetric shape at molecules with coordination at only one side. This comparison corroborates that the local coordination bonding induces spatial modification to the molecular orbitals, while the hydrogen bonding and electrostatic interactions influence the molecular states globally.
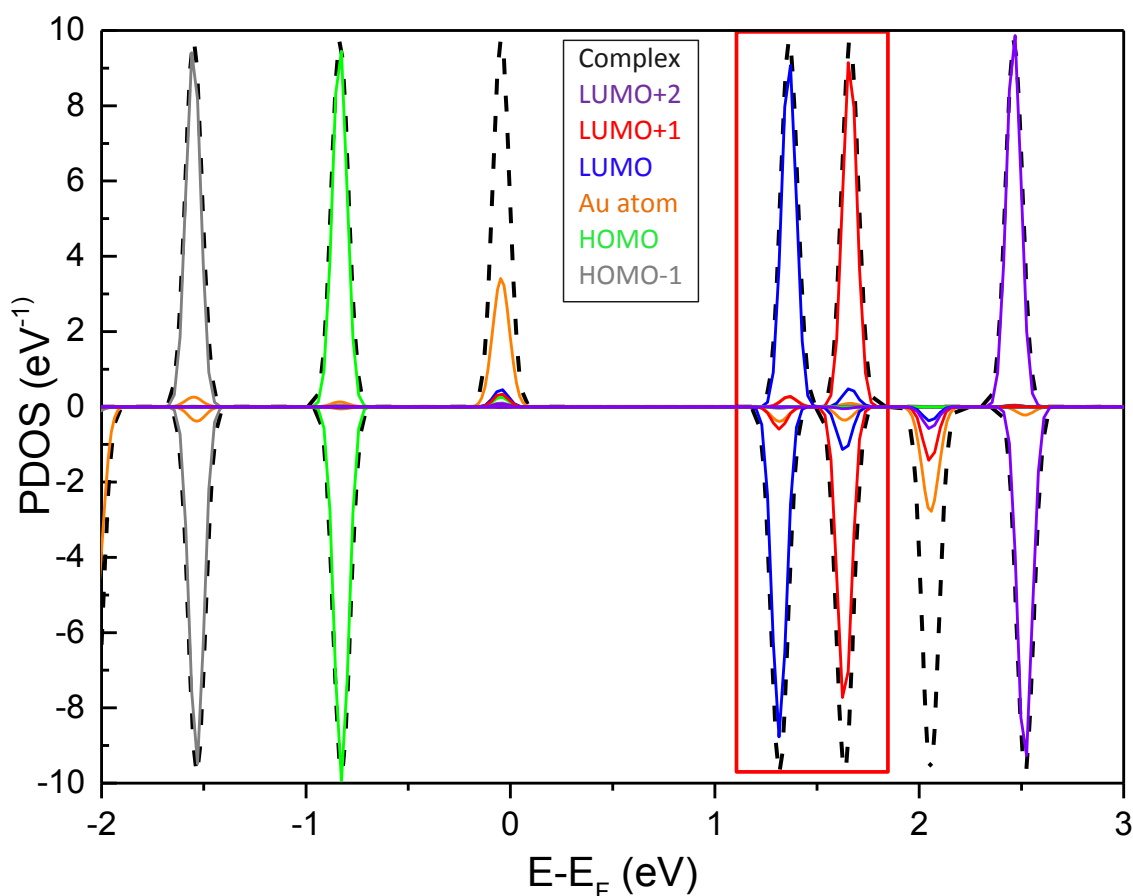

Figure 3.10: DFT calculated density of states at the one-Au/DCV5T-Me$_2$ complex (black dash peaks) projected onto the free molecular states (colored peaks). The red square highlights the LUMO and LUMO+1 peaks. The LUMO (LUMO+1) at the complex has contributions from both the LUMO and LUMO+1 of the free molecule.

3.3 Mixing DCV5T-Me$_2$ with Na Atoms

As has been shown in section 2.2, upon deposited on Au(111) DCV5T-Me$_2$ molecules form assemblies (islands and chains) with different bonding motifs. The mixing of two different structures with different electronic properties is not favorable for the corresponding organic devices. In order to fabricate architectures with homogenous bonding geometry, external components, which exhibit more chemical reactivity for substituting the intermolecular interactions and Au-CN coordination, have to be introduced. Alkali metal atoms are ideal candidates for this purpose, since they are very prone to transfer electrons to organic ligands and bond with them. Amongst, Na atoms can be easily obtained by depositing NaCl onto the metal surface. Two dimensional ionic layer by reaction of NaCl and TCNQ with Na-CN bonding has been fabricated in this way [139, 140]. The same reaction scenario is expected upon codeposition of DCV5T-Me$_2$ and NaCl on Au(111). However, the exact assembled structure should be different from the TCNQ case, due to the complex chemical configuration of DCV5T-Me$_2$. For example, instead of compact domains, porous networks are anticipated because of the long backbone of DCV5T-Me$_2$. Moreover, the charge distribution within the acceptor-donor-acceptor (A-D-A) molecule may also mediate the growth of the assemblies.

3.3.1 Two Mixing Procedures

We start by describing the mixing procedures of DCV5T-Me$_2$ and NaCl depending on the order of their deposition. Figure 3.11 a - c show STM images of first deposition of NaCl followed by evaporation of DCV5T-Me$_2$ at room temperature. It is found that DCV5T-Me$_2$ assemblies (chains and islands) and NaCl islands separately disperse on the surface simultaneously (figure 3.11 a). The bonding structures of DCV5T-Me$_2$ chains and islands are not influenced by the presence of NaCl (figure 3.11 b), meaning that no mixing occurs. This is due to DCV5T-Me$_2$ can not extract Na atoms from the established NaCl molecules at room temperature. Thermal activation induces changes of the structure. As shown in figure 3.11 c, post-annealing the sample to 400 K transforms the heterogeneous assemblies into long and parallel bi-molecular chains covering the whole surface. We attribute this production to reaction of NaCl and DCV5T-Me$_2$ with the formation of Na-CN bonding [139, 140] other than the increased number of Au adatoms at higher temperature, because annealing the sample without NaCl deposition to the same temperature induces no change to the DCV5T-Me$_2$ assemblies. Moreover, these chains are transformed to glassy networks by post-annealing to 500 K (shown in section 3.3.4), while nothing is changed to the Au/DCV5T-Me$_2$ chains at 500 K. This furthermore demonstrates that the structure in figure 3.11 c is from the bonding between Na atoms and DCV5T-Me$_2$ molecules.

In contrast, Na atoms and DCV5T-Me$_2$ start to mix when NaCl is deposited on the pre-formed DCV5T-Me$_2$ assemblies, as shown in figure 3.11 d. The organic islands

are transformed to disordered phases (figure 3.11 e), where cyano groups assemble or are pinned to the NaCl islands indicating the incorporation of Na atoms. Ordered Na/DCV5T-Me$_2$ structure, long chains, also can be produced through thermal activation, as shown in the STM image after annealing the sample to 400 K in figure 3.11 f. Therefore, here we conclude that the first-step results of mixing DCV5T-Me$_2$ and NaCl are strongly dependent on the order of deposition, while in the end thermal activation leads to the formation of homogenous bi-molecular chains with ionic bonds [5].
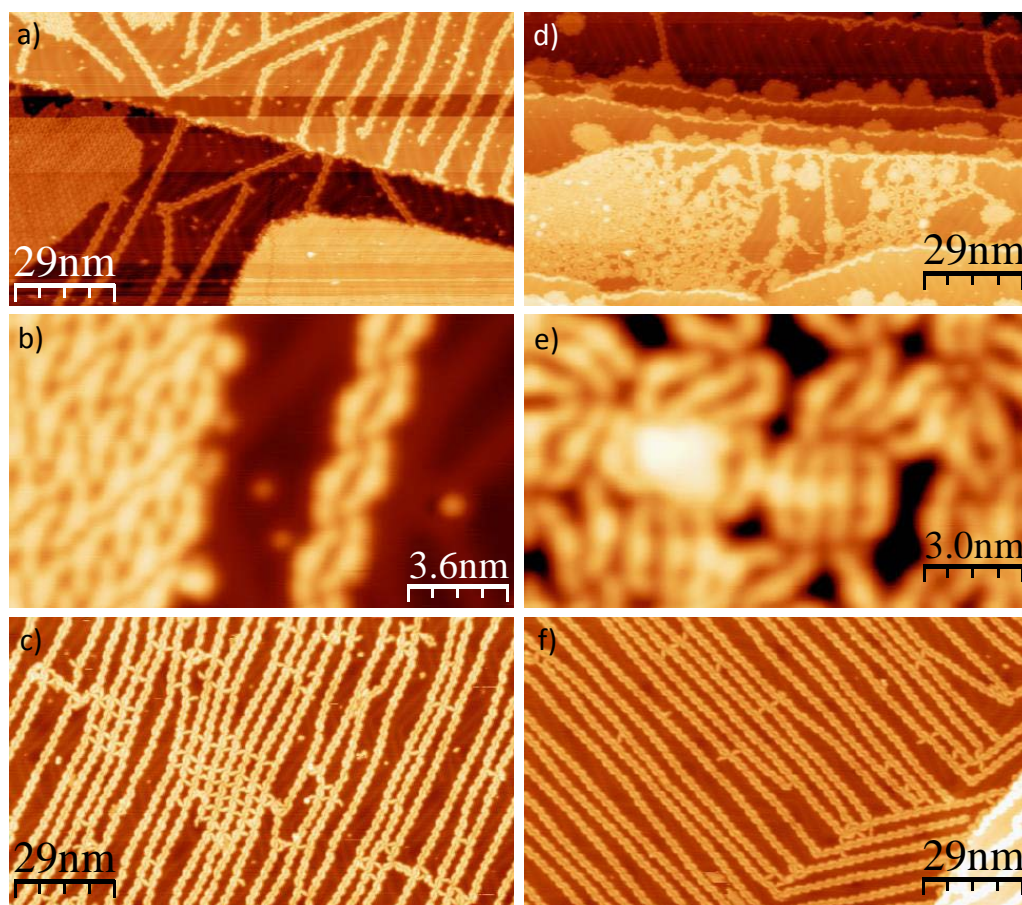
Figure 3.11: Results of two procedures for mixing DCV5T-Me$_2$ with Na atoms from NaCl on Au(111). (a) - (c) First deposition of NaCl followed by evaporation of DCV5T-Me$_2$. a) A STM overview (I = 56 pA, V = 0.67 V) of the co-deposition of DCV5T-Me$_2$ with NaCl at room temperature. b) High resolution STM image (I = 100 pA, V = 0.68V) of the islands and chains. c) STM image (I = 110 pA, V = 0.63 V) after annealing the sample to 400 K. (d) - (f) First deposition of DCV5T-Me$_2$ followed by evaporation of NaCl. d) A STM overview (I = 82 pA, V = 0.65 V) of the co-deposition of DCV5T-Me$_2$ with NaCl at room temperature. e) High resolution STM image (I = 170 pA, V = 0.65V) of the disordered mixture domain. f) STM image (I = 63 pA, V = 0.61 V) after annealing the sample to 400 K.

---

[5] Here the Na-CN bonding should be ionic instead of coordinative, because the Na atoms is prone to transfer one electron to the ligand in the bonding.

3.3.2 Long-range Repulsive Growth of Metal-organic Chains

The deposition of DCV5T-Me$_2$ with NaCl and posterior annealing, lead to the formation of quasi-periodic one-dimensional super-lattice in the direction perpendicular to the growth of chains, as shown in figure 3.12 a - c. We compare the results of depositing three different amounts of DCV5T molecules, corresponding to coverages of 0.21 monolayer (ML), 0.38 ML and 0.49 ML [6] Assembly of islands is expected *via* the short-range intermolecular attractive interactions and bridging of metal atoms [139, 140]. However, in the present case, the long chains keep separate, parallel and equi-distant, being accompanied by a monotonous decrease of the inter-chain distance with the increase of coverage. This trend to avoid compact assembly through the formation of quasi-periodic one-dimensional super-lattices is a fingerprint of a long-range repulsive interaction.

Metal-organic porous networks are formed when the coverage reaches a threshold, 0.75 ML, as shown in figure 3.12 d. At this coverage, the inter-chain separation is reduced to the value similar with the length of one molecule. At this point, the excess molecules adopt such a geometry that DCV groups at both sides contact the joints of two adjacent chains rather than form more chains.
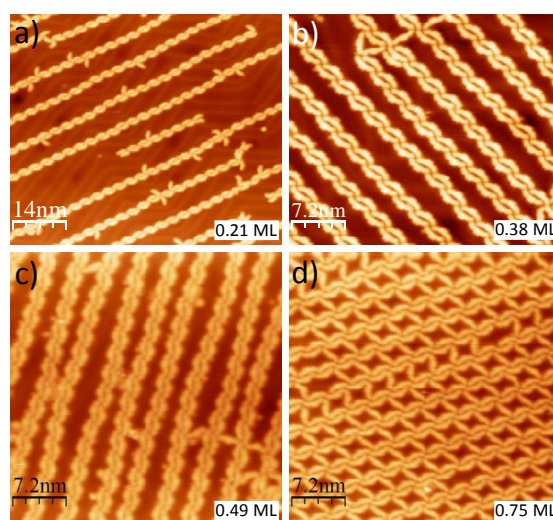
Figure 3.12: STM images of DCV5T-Me$_2$/Na chains and networks at various coverages on Au(111). a) 0.21 ML (I = 100 pA, V = 0.65 V). b) 0.38 ML (I = 66 pA, V = 0.64 V). c) 0.49 ML (I = 57 pA, V = 0.63 V). d) 0.75 ML (I = 210 pA, V = 0.69 V). The distances between neighboring chains decrease with the increases of coverage, while the chains keep nearly parallel and equi-distant. When the coverage is high enough, the adjacent chains can be connected by individual molecules forming porous networks (d).

The structure of bonding to Na atoms evolves with the increase of coverage. At relative lower coverage, 0.21 ML, the CN-Na bonding is three-fold and two Na

---

[6]The molecular coverage is determined from STM images of large surface areas, assuming that 1 ML corresponds to 0.4 molecule per nm^2.

atoms are incorporated in one node (figure 3.13 a). Whereas, at relative higher coverage, 0.38 ML, a four-fold CN-Na bonding motif is formed, where one node possesses one Na atom (figure 3.13 b). We attributed this transformation to the ratio between molecules and metal atoms available for bonding [7]. We assume that at a certain temperature there is an equilibrium between Na atoms confined in NaCl islands and free to bond with ligands. With the increase of molecular coverage, Na atoms available for coordination are not enough for the three-fold bonding geometry, where the ratio between Na and DCV5T-Me$_2$ is 1:1. Hence, the bonding adapts itself a four-fold geometry with a Na/DCV5T-Me$_2$ ratio of 1:2. This explanation is confirmed by the fact that at very high molecular coverage a few molecular islands survive on the surface due to lack of Na atoms for bonding although NaCl islands still exist. In the porous networks, the four-fold bonding configuration is maintained, as shown in figure 3.13 c. In addition, the molecules connecting neighboring chains adopt a metastable configuration with one DCV group and its adjacent thiophene ring rotated (figure 3.13 c).
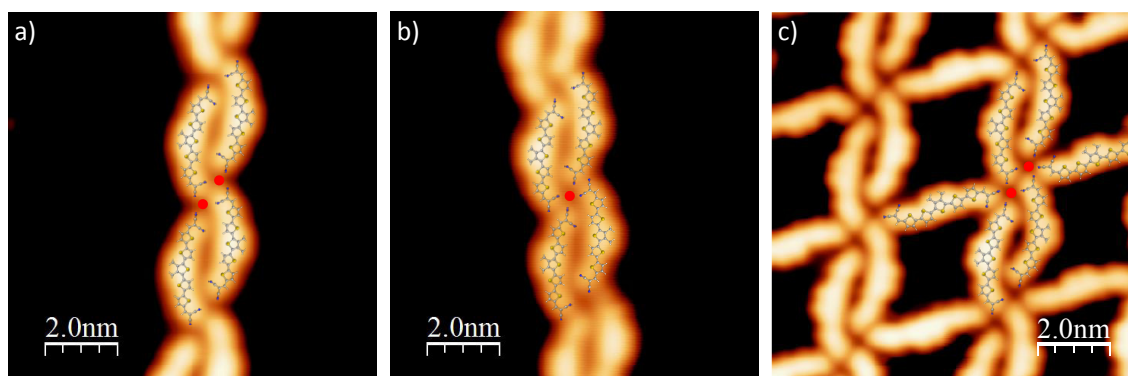
Figure 3.13: High resolution STM images of DCV5T-Me$_2$/NaCl mixing structures at various coverages on Au(111). At relative lower coverage of 0.21 ML (a: I = 170 pA, V = 0.65 V) the CN-Na bonding frame is three-fold; at relative higher coverage of 0.38 ML (b: I = 110 pA, V = 0.6 V) the CN-Na bonding frame is four-fold; at high coverage of 0.75 ML (c: I = 180 pA, V = 0.63 V) porous networks are formed and the four-fold CN-Na bonding frame is maintained. The model of the molecules is superimposed to identify the bonding structure. One DCV group and one thiophene ring are rotated in the molecules connecting the parallel chains. The red circles represent the Na atoms.

In order to get an insight in the origin of this one-dimensional metal-organic super-lattice, we performed a statistical analysis of the inter-chain distance for the four different coverages investigated in figure 3.12. The distributions are shown in figure 3.14. For each plot 200 chain-pairs are taken into account. The distributions are peaked with a dominant inter-chain distance, whose value is 6.8 nm, 4.5 nm, 4.0 nm and 3.7 nm from the lowest to the height coverage, respectively. The one-dimensional random distribution, f_{ran}, corresponding to particles without interactions is plotted for each coverage in figure 3.14 as well. The one-dimensional random distribution is

---

[7]The same explanation as the Au/DCV5T-Me$_2$ case.
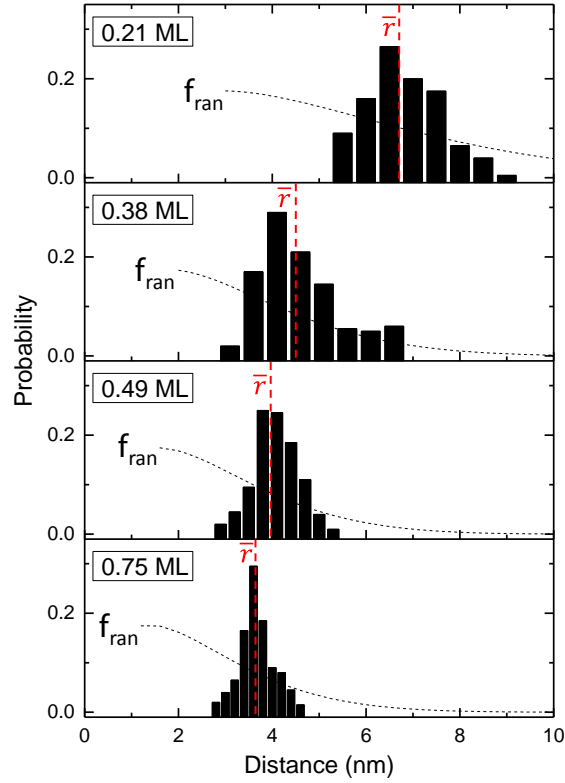
Figure 3.14: Inter-chain distance distribution between adjacent chains at different coverages. The dominant chain-distances, $\overline{r}$, are highlighted with red dash lines (6.8 nm, 4.5 nm, 4.0 nm and 3.7 nm). The corresponding one-dimensional random distributions for non-interaction particles, f_{ran}, are shown as black dash lines.

expressed as [22, 147]:

$$f_{\mathrm{ran}} = \frac{Nar}{L}(1 - \frac{2r}{L})^N \tag{3.1}$$

where N is the number of chains per image, L is the distance from the first chain to the last chain in one image, a is the minimum width of the box which can fit one unit cell of chains inside, and r is the distance between two adjacent chains. The random inter-chain separation distributions decrease monotonously in the experimentally observed distance range for all the four coverages, while the experimental data exhibit a peaked distribution. This confirms the existence of an inter-chain interaction.

There are several mechanisms which can induce the long-range quasi-periodic growth of molecules on metal surfaces. The reconstruction of the Au(111) surface may play a role in the molecular growth. The fcc regions can offer more stable adsorption sites due to the lower concentration of surface atoms when considering the buried layers [22, 98]. As a result, molecules preferentially adsorb in the fcc regains forming one-dimensional super-lattice. However, in the present case, the growth direction of

chains crosses the herringbones (figure 3.12 a). Therefore, the mediation from the surface reconstruction can be ruled out here.

Friedel oscillation of the two-dimensional surface electrons also can induce long-range interactions to adsorbates [147, 148, 149, 150, 151]. The fingerprint of Friedel oscillation is that the oscillatory character of the interactions corresponds to half of the Fermi wavelength (λ_F). For Au(111), it is 1.8 nm [151]. However, the statistics on the experimental data shows much larger inter-chain separations and one-peaked distributions for all coverages. Therefore, the surface-electron-mediated growth also can be excluded here.

Besides the mediation from substrates, the dipolar nature of the adsorbates can hinder the self-assembly as well [22, 152]. The existence of an intrinsic dipole within molecules or charge localized between molecules and metal surfaces can create intermolecular repulsive interactions. Although interactions between DCV5T-Me$_2$ and Au(111) are weak, dipoles within individual DCV5T-Me$_2$ are expected due to the built-in acceptor-donor-acceptor structure. This dipolar nature of DCV5T-Me$_2$ should still exist when bonding with Na atoms, which should be responsible for the long-range repulsive growth of chains.

3.3.3 DFT Calculations

In order to get deeper insight into the long-range repulsive growth, we performed DFT calculations. The calculations show that a bond with length of 2.1 Å between cyano group and Na atom is formed with DCV5T-Me$_2$ keeping planar configuration, as shown in figure 3.15 a. Due to the higher electronegativity of organic molecules than Na atoms, 0.817 e$^-$ is transferred from Na to DCV5T-Me$_2$. Within individual DCV5T-Me$_2$, the cyano groups are negatively charged, while the sulfur atoms and hydrogen atoms are positively charged (figure 3.15 b).

Electrostatic potential induced by the charged atoms within individual molecules determines the intermolecular interactions. An iso-surface with a total electron density of 0.006e/Å^3, generated from the self-consistent field (SCF) density matrix, was plotted onto the optimized structure. Then this electron density iso-surface was mapped with the SCF-generated electrostatic potential energy felt by an electron moving over this surface, as shown in figure 3.15 c. It reveals that positive potential (blue color) is localized at the convexity of the molecule, while negative potential (red color) is located at the cyano groups and the inner part. As a result, an assembled chain possesses positive potential at the outer circle and faces it to the adjacent chains, thereby inducing long-range inter-chain repulsive force, as sketched in figure 3.15 d. We believe that these electrostatic interactions are the mechanisms that drive the formation of one-dimensional super-lattice of metal-organic chains.

The experimental interaction potential can be obtained by further analysis on the
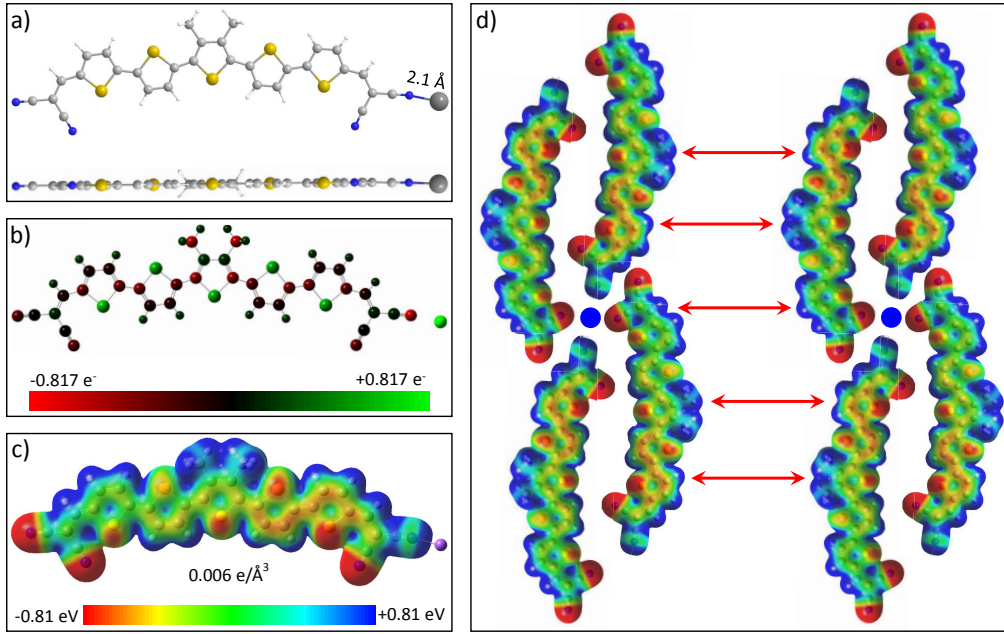
Figure 3.15: DFT calculations of the Na/DCV5T-Me$_2$ complex. a) Relaxed structure. The gray circle stands for the Na atom. b) Total charge distribution from Mulliken population analysis. c) Calculated electrostatic potential energy of a molecule with one-side bonded. The red stands for electron accumulation, while the blue stands for electron depletion. d) The model showing the long range repulsive force between adjacent chains.

statistics in figure 3.14. The experimental distribution f_{exp} and the random distribution f_{ran} are related to each other by Boltzmann factor [22, 147, 152]:

$$f_{exp} = f_{ran}\exp[-E(r)/k_B T] \tag{3.2}$$

where $E(r)$ is the interaction potential energy as a function of the inter-chain distance, k_B is the Boltzmann constant, and T is the temperature of the system. Then the interaction potential energy can be expressed as:

$$E(r) = -k_B T\ln[f_{exp}/f_{ran}] \tag{3.3}$$

We divide the experimental distribution by the random one and plot $-\ln[f_{exp}/f_{ran}]$ in figure 3.16. The potential exhibits a well shape for all the four coverages [8]. Moreover, with the increase of the coverage, the potential well becomes shallower and more symmetric corresponding to smaller r. It indicates that the chains are confined by the inter-chain interactions forming a super-lattice and stabilizing the whole system.

The potential from statistics in the limit of a dilute system, is expected to be a good approximation for the repulsive pair interaction potential. The Coulomb repulsion

---

[8]The peak in the red curve for coverage of 0.38 ML is noise from the statistics in figure 3.14.

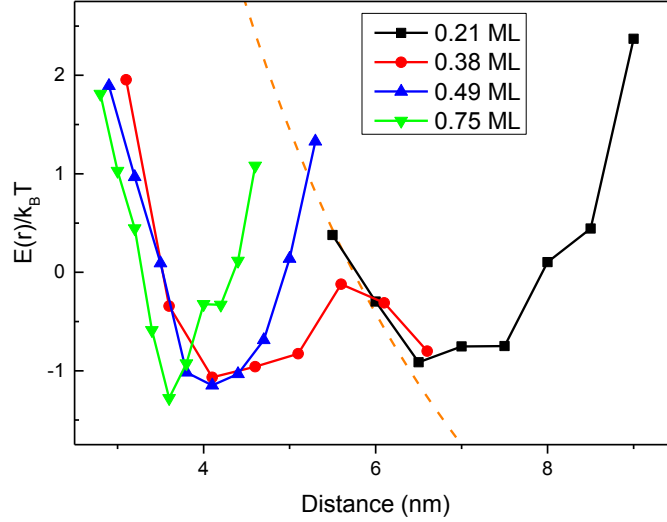**Figure 3.16:** Potential energy between adjacent chains as a function of the distance at different coverages. The repulsive force between chains induces the well shape of the potential and the corresponding dominant average distances (6.8 nm, 4.5 nm, 4.0 nm and 3.7 nm). The orange dash line represents modeled Coulomb repulsion potential, acquired by assuming that the inter-chain interaction is dominated by practicals (CH$_3$) charged with one e$^-$ at room temperature (300K). After shifting upwards 9.75, it nicely fits with the potential from statistics at dilute limit (0.21 ML). This up-shifted value represents the zeroth order internal potential of the system.

induced potential is given as:

$$E(r_{ij})_{\text{Coulomb}} = \frac{1}{4\pi\epsilon_0} \frac{q_i q_j}{r_{ij}} \tag{3.4}$$

where q_i and q_j are the charges located at two points and r_{ij} is their distance. The dipole-dipole interaction induced potential follows:

$$E(r_{ij})_{\text{dipole}} = \frac{1}{4\pi\epsilon_0} \frac{\mu_i \mu_j}{r_{ij}^3} \tag{3.5}$$

where μ_i and μ_j are the dipole moments of two polar objects and r_{ij} is their distance.

Our DFT calculations show that the six hydrogen atoms at the two methyl groups have each one positive charge. Assuming that $q_i = q_j = 1$ e$^-$, the Coulomb repulsive potential (orange curve) fits with the potential of the most dilute coverage (0.21 ML) from statistics at small inter-chain distance, as shown in figure 3.16. In contrast, the modeling dipole-dipole interaction can not fit with the experimental data. It means that the two methyl groups at individual molecules can be treated as one positively charged point and dominate the repulsive interaction between chains, while the internal parts of chains do not play a crucial role due to being screened by the outer parts. Moreover, the positive charges at the methyl groups are not completely screened by Au(111), therefore, no strong dipoles are created.

3.3.4 Formation of Glassy Networks

In contrast to the wide investigation of glasses and amorphous materials in bulk, only few studies are reported at molecular level [153, 154]. For our system, post-annealing to 500 K transforms the ordered metal-organic chains to two-dimensional glassy networks [9], as shown in figure 3.17 a. Although the structure is not long-range ordered and even the molecules themselves adopt different configurations, all the molecules assemble through end-to-end connection indicating a homogenous CN-Na bonding motif, as shown in the STM image in figure 3.17 b. There are three typical kinds of components within the amorphous networks. One of them is the two-molecule-wide chains (figure 3.17 c), where four cyano groups from four adjacent molecules gather implying four-fold coordination. Another component is the one-molecule-wide chains (figure 3.17 d) with two-fold coordination. The third one is the pore (figure 3.17 e) with two-fold coordination as well. The flexibility and diversity of molecular configuration determine the amorphous growth of networks [153, 154], which is activated by the high temperature annealing. This metal-organic based two-dimensional glassy material is an ideal platform to study the properties of condensed disordered matters.
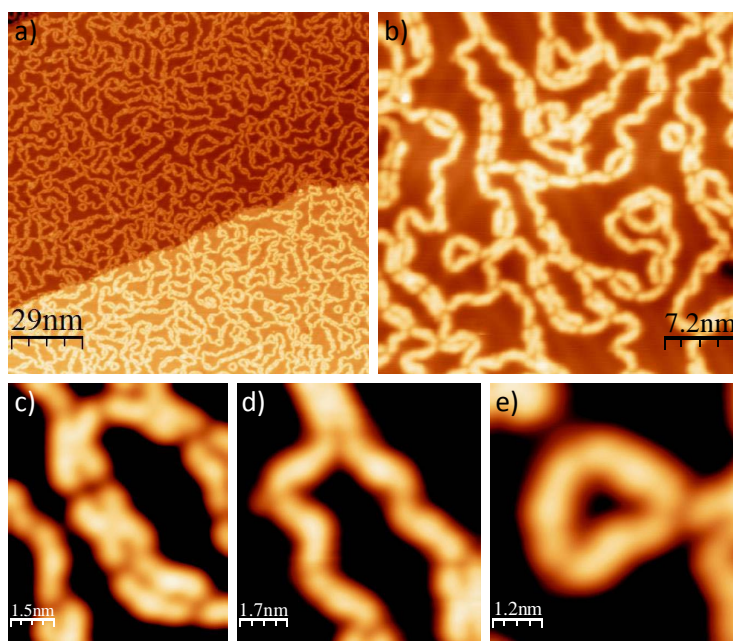
Figure 3.17: Glassy networks obtained by high temperature annealing (500 K). a) An overview STM image (I = 130 pA, V = 0.63 V) after annealing the sample covered with DCV5T-Me$_2$/Na chains to 500 K. The chains are transformed to two-dimensional amorphous porous networks. b) A zoom-in STM image (I = 130 pA, V = 0.63 V) of the disordered networks. c) − e) STM images (I = 130 pA, V = 0.63 V) of the three typical components (two-molecule-wide chain, one-molecule-wide chain and molecular pore) of the amorphous networks.

---

[9]Note that the structure of Au/DCV5T-Me$_2$ chains is not influenced by annealing to 500 K, which confirms the substitution of Na for Au after deposition of NaCl.

3.4 Mixing DCV5T-Me$_2$ with Organic Molecules

DCV5T-Me$_2$ is designed as an absorber of light and serves as electron donor in high efficiency organic solar cells [106]. The physics at the interface with another type of organic material is interesting, because it determines the charge transfer process, hence, influence the performance of the device. Therefore, in this section we mix DCV5T-Me$_2$ with electron acceptor molecules (C$_{60}$, coronene and TCNQ) and study their interface properties at sub-molecular resolution with STM/STS.

3.4.1 Mixing with C$_{60}$

Recently, organic solar cells composed of hybrid films of DCVnTs and C$_{60}$ have been fabricated [106]. Amongst them, devices based on DCV5T-Me$_2$ and C$_{60}$ exhibit the best performance with an efficiency of 7% [48, 106]. In order to gain a microscopic understanding of their mixing structure, we co-deposited DCV5T-Me$_2$ and C$_{60}$ on Au(111) at sub-monolayer coverage. However, DCV5T-Me$_2$ assemblies (islands and chains) and C$_{60}$ islands disperse separately on the surface without mixing, as shown in figure 3.18 a. We attribute the absence of mixing to the intermolecular interactions amongst DCV5T-Me$_2$ and the coordination bonding between DCV5T-Me$_2$ and Au atoms, which are stronger than the interactions between DCV5T-Me$_2$ and C$_{60}$ and hinder their binding. As reported before [20, 21, 155], C$_{60}$ molecules adsorb on the Au(111) surface with different orientations (figure 3.18 b). The C$_{60}$ with two-fold symmetry axis adsorbs with two pentagon rings upwards (orientation 1 in figure 3.18 b), while the triangle shape corresponds to a hexagon ring upwards (orientation 2 in figure 3.18 b).
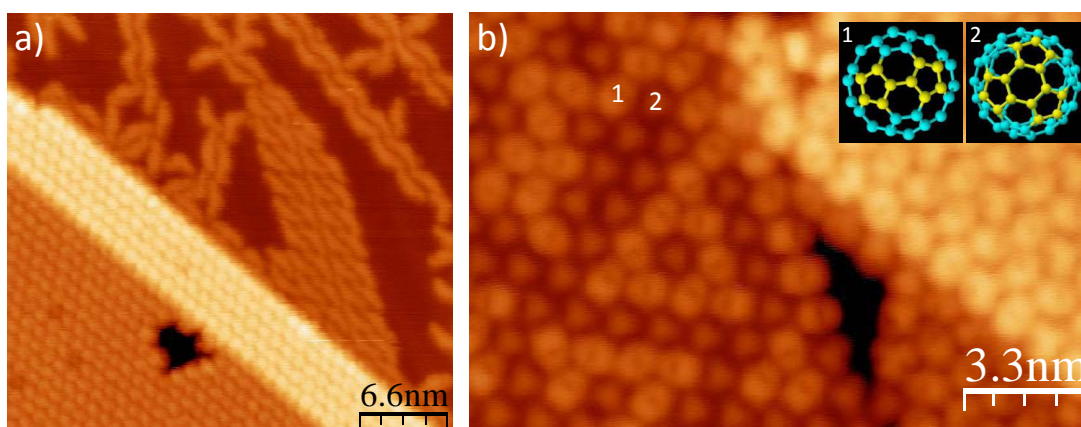
Figure 3.18: Mixing DCV5T-Me$_2$ with C$_{60}$ in sub-monolayer on Au(111). a) STM image (I = 72 pA, V = 1.03 V) of co-deposition of DCV5T-Me$_2$ and C$_{60}$ at room temperature followed by annealing to 430 K. b) High resolution STM image (I = 71 pA, V = 0.8 V) of C$_{60}$ islands on Au(111). Inset: models showing arrangement of C$_{60}$ [155].

In order to inspect the electronic structure of the interface between DCV5T-Me$_2$ and

C_{60}, we deposited C_{60} on top of a saturated DCV5T-Me$_2$ monolayer on Au(111), as shown in figure 3.19 a [10]. Typical hexagonal islands of C_{60} are formed also on the DCV5T-Me$_2$ film. A high resolution STM image reveals that C_{60} adopts only one type of orientation with two-fold symmetry axis (figure 3.19 b). This homogeneous orientation could be ascribed to the π-π interaction between C_{60} and DCV5T-Me$_2$, presumably stronger than the interaction between C_{60} and Au(111) surface. The spectra show that C_{60} on DCV5T-Me$_2$ monolayer (black in figure 3.19 c) possesses higher LUMO orbital in energy compared with that of C_{60} on Au(111) (gray in figure 3.19 c), which is due to the decoupling effect of the organic film of DCV5T-Me$_2$ [156]. On the other hand, the far-lying of C_{60} LUMO from the Fermi level in energy indicates that no electrons are transferred from DCV5T-Me$_2$ to C_{60}. This can be interpreted from the point of view of energy alignment at their interface. The onset of LUMO at the decoupled C_{60} is around 1.3 V (black in figure 3.19 c), which is higher than the onset of LUMO at DCV5T-Me$_2$ (1.1 V) on Au(111) (red in figure 3.19 c). This orbital energy alignment inhibits electron transfer from DCV5T-Me$_2$ to C_{60}, because electrons can not move from lower energy level to higher one.
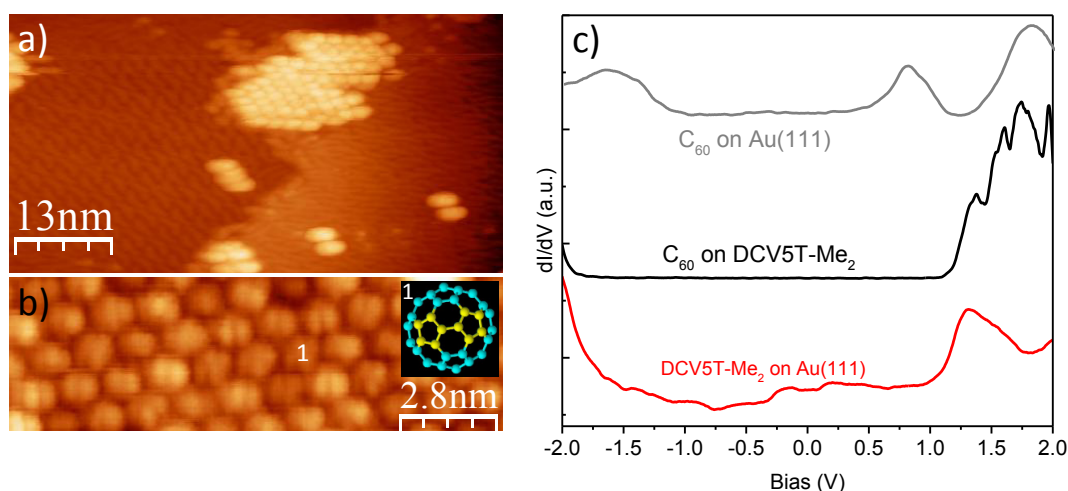
Figure 3.19: Mixing DCV5T-Me$_2$ with C_{60} in double-layer on Au(111). a) STM image (I = 63 pA, V = 0.86 V) of deposition of monolayer of DCV5T-Me$_2$ followed by evaporation of C_{60} at room temperature. b) High resolution STM image (I = 22 pA, V = 0.85 V) of C_{60} islands on top of the DCV5T-Me$_2$ layer. Inset: models showing arrangement of C_{60} [155]. c) dI/dV spectra acquired with open feedback at C_{60} on Au(111) (gray: set point is I = 110 pA and V = -2.2 V), C_{60} on top of the DCV5T-Me$_2$ monolayer (black: set point is I = 75 pA and V = -2.1 V) and DCV5T-Me$_2$ on Au(111) (red: set point is I = 110 pA, V = -2 V).

3.4.2 Mixing with Coronene

Coronene is a polycyclic aromatic hydrocarbon including six fused benzene rings, as shown in figure 3.20 a. It can be considered as the analogue of C_{60} in two dimension

---

[10]The reduplication of features in this image is due to being taken with a double-tip.

saturated by hydrogen [157]. Therefore, we expected that it could mix with DCV5T-Me$_2$ when confined to the metal surface. Upon adsorption, coronene disperses on Au(111) (figure 3.20 b). The spectrum (black in figure 3.20 e) shows that coronene possesses HOMO orbital at -1.5 V. The dI/dV map in figure 3.20 c reveals that the HOMO is localized at the outer ring of the molecule, which is in agreement with the DFT calculations in gas phase (figure 3.20 a).
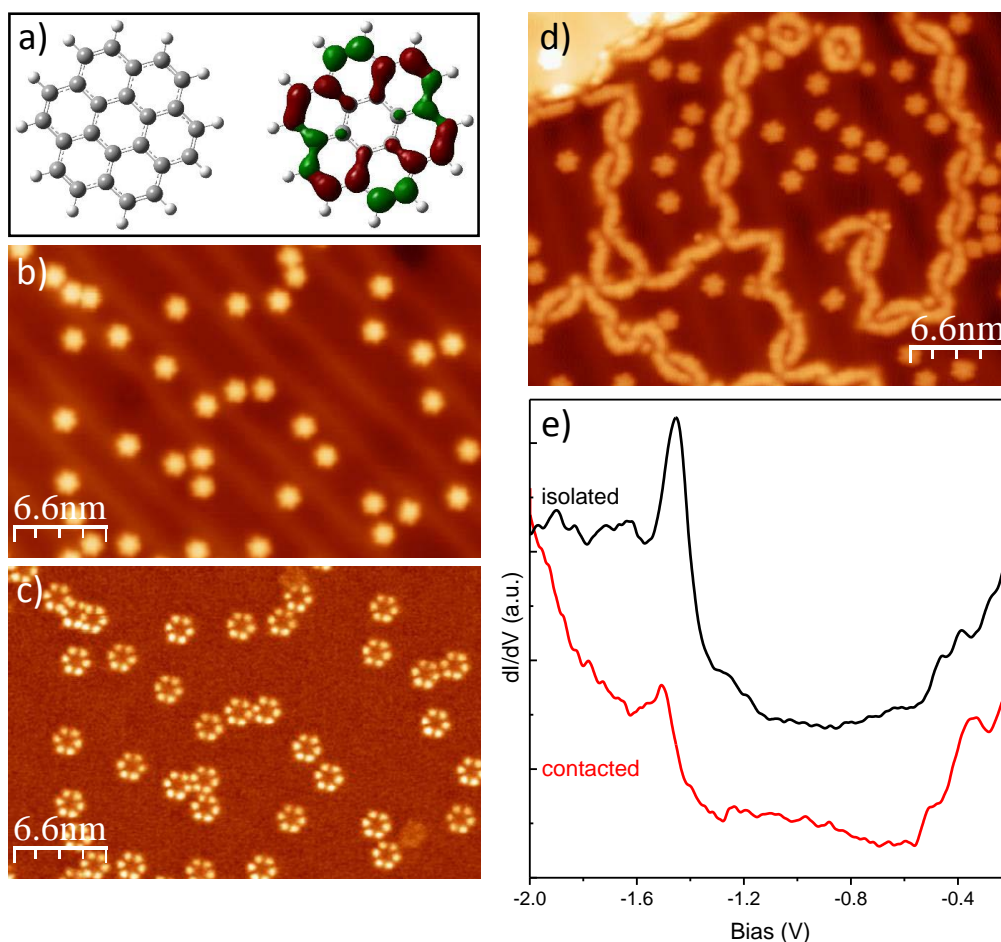
Figure 3.20: Mixing DCV5T-Me$_2$ with coronene on Au(111). a) Chemical structure of coronene (white: hydrogen, grey: carbon) and DFT calculated HOMO orbital structure in gas phase. b) STM image (I = 67 pA, V = -1.45 V) of coronene deposited on room temperature surface. c) Corresponding dI/dV map. d) STM image (I = 34 pA, V = -1.45 V) of the co-deposition of DCV5T-Me$_2$ and coronene at room temperature followed by annealing to 370 K. e) dI/dV spectra acquired with open feedback (set point: I = 51 pA and V = - 2 V) at the edge of one isolated coronene (black) and one coronene contacting with a DCV5T-Me$_2$ (red).

Figure 3.20 d shows a STM image after co-deposition of coronene with DCV5T-Me$_2$ on Au(111). No ordered mixing phase is formed even after thermal activation by annealing to 370 K, with only a few coronene occasionally contacting with DCV5T-Me$_2$ chains. The spectrum (red in figure 3.20 e) taken at the coronene contact-

ing with DCV5T-Me$_2$ exhibits the same features as that measured on the isolated coronene. It indicates that no significant interactions exist between the two types of molecules. In this case, the mixing should be hindered by the strong coordination bonding between DCV5T-Me$_2$ and Au atoms as well. Moreover, both the DCV5T-Me$_2$ and coronene expose positively charged hydrogen atoms outwards, which is not favorable for attractive intermolecular interactions. In contrary, negatively charged functional groups should enable the mixing with DCV5T-Me$_2$. Therefore, we try TCNQ in the following section.

3.4.3 Mixing with TCNQ

TCNQ is a typical electron acceptor and widely used in the charge transfer complex [140, 142]. Figure 3.21 a shows the STM image of co-deposition of TCNQ with DCV5T-Me$_2$ on Au(111). Large TCNQ islands and disordered mixed domains of TCNQ and DCV5T-Me$_2$ are formed. TCNQ molecules interact with each other through hydrogen-bonds in islands, as shown in the inset of figure 3.21 a [28]. High resolution STM image (figure 3.21 b) of the mixed phase shows that TCNQ is randomly embedded amongst the DCV5T-Me$_2$ molecules. By superimposing the molecular models on the STM image, it is determined that intermolecular hydrogen-bonds (red lines in figure 3.21 b) between cyano ligands and CH groups are formed. Although these hydrogen-bonds are not strong enough to drive the assembly of ordered hybrid structure, they are comparable in strength with the bonding between two DCV5T-Me$_2$ enabling the growth of a mixing phase. During mixing, some DCV5T-Me$_2$ adopt asymmetric configurations to optimize the bonding with adjacent TCQN molecules, as shown in figure 3.21 c. All these results demonstrate that mixed structure can be obtained by co-deposition of DCV5T-Me$_2$ and TCNQ on Au(111).

To inspect the influence of interactions between DCV5T-Me$_2$ and TCNQ on their electronic properties, we performed STS measurements. As shown in figure 3.21 d, spectra at TCNQ molecules in the mixed phase exhibit either a sharp peak (blue) around +1 V or a sharp deep (red) around -1 V, while the LUMO-derived resonance at +0.8 V (gray) in the TCQN islands is absent there. As reported on a TCNQ-based charge transfer complex [158], the sharp peak and deep are the fingerprints of discharging and charging of one electron over a single TCNQ molecule, respectively. The intensity and energy position of the peak and deep vary with the STM tip positions located over different TCNQ molecules, because of the change of chemical environments for each molecule in the disordered structure. Nevertheless, these features definitely demonstrate that electrons are transferred from DCV5T-Me$_2$ to TCNQ at their interface. Therefore, in addition to C$_{60}$, TCNQ could be another option to combine with DCVnTs molecules for building organic solar cells. The stronger interaction between TCNQ and DCVnTs than that between DCVnTs and C$_{60}$, may result in better performance of the device.
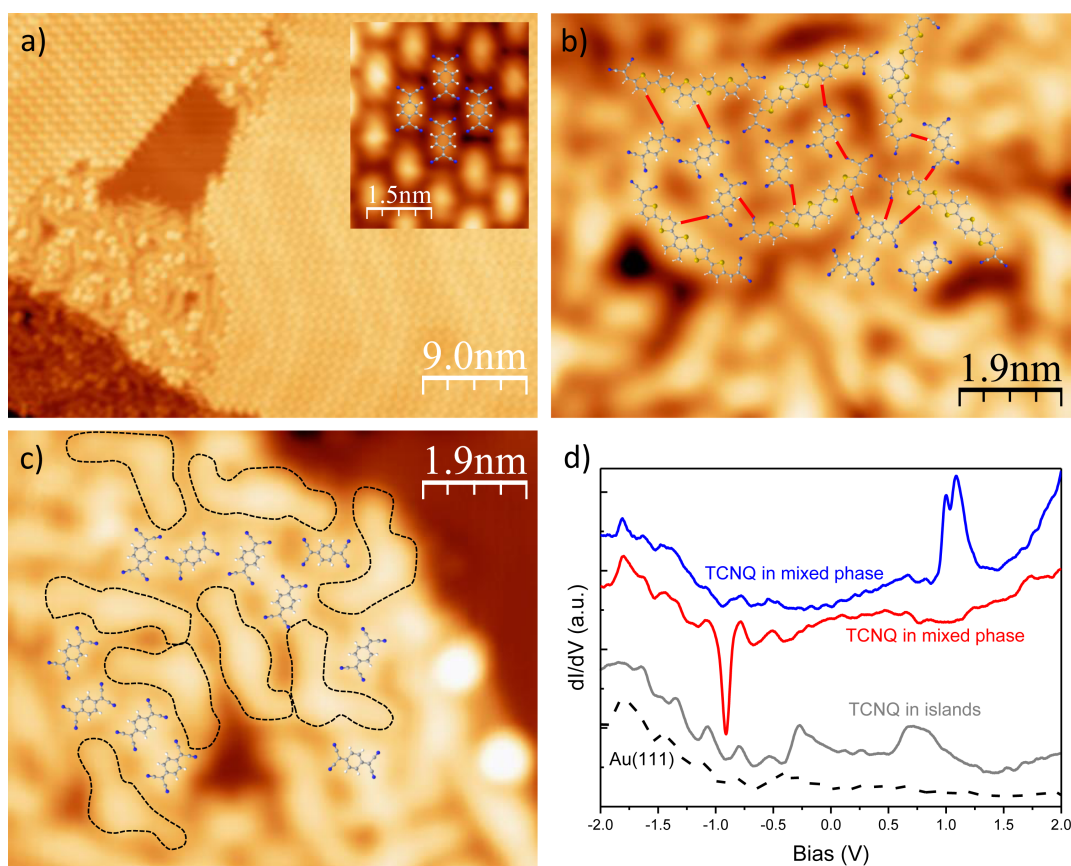
Figure 3.21: Mixing DCV5T-Me$_2$ with TCNQ on Au(111). a) STM overview (I = 63 pA, V = 0.8 V) of the co-deposition of DCV5T-Me$_2$ and TCNQ on cold sample followed by annealing to 373 K. Large TCNQ islands and disordered mixture domains are formed. Inset: high resolution STM image (I = 56 pA, V = -0.71 V) of the pure TCNQ domain with bonding model superimposed. b) and c) High resolution STM images (b: I = 53 pA and V = 1.12 V, c: I = 53 pA and V = 0.71 V) of the mixture domains with molecular model superimposed. Red lines in b indicate hydrogen-bonds between DCV5T-Me$_2$ and TCNQ. Black dash lines in c sketch the shape of DCV5T-Me$_2$. d) dI/dV spectra acquired with open feedback (set point: I = 130 pA and V = - 2 V) at TCNQ in mixed phase (blue and red) and ordered TCNQ islands (gray).

3.5 Conclusions

In this chapter various complexes based on DCV5T-Me$_2$ are studied. DCV5T-Me$_2$ molecules self-assemble into metal-organic chains on Au(111) *via* the capture and coordination to Au adatoms, which are resolved by AFM in real space. The coordination with metal atoms at two sides of molecules causes a characteristic energy downshift of the LUMO with respect to uncoordinated single molecules. Interestingly, when molecules are coordinated at only one side, the LUMO and LUMO+1 orbitals are spatially redistributed within individual molecules. It is interpreted using a linear combination of molecular orbitals, in which the Au atom triggers a mixing of unoccupied states to produce a new set of orbitals that are adapted to

the new bonding geometry. This depicts a tuning strategy to manipulate the orbital character of molecular films by site-specific doping with metal atoms.

The mixing structure of DCV5T-Me$_2$ with Na atoms offered by NaCl is determined by the kinetics and thermodynamics processes. Ordered metal-organic chains or networks can be obtained by thermal activation to 400 K. Further annealing to 500 K transforms the ordered long chains to disordered glassy networks through altering the molecular configuration.

The Na/DCV5T-Me$_2$ chains, keeping separate and parallel, grow with coverage-dependent distance, which decreases with the increase of coverage. The statistics on the inter-chain distance distribution reveals an inter-chain repulsive force generating an electrostatic potential well, which induces the formation of the one-dimensional super-lattice. It is demonstrated that the charged methyl groups within individual molecules serve as positively charged points and are responsible for the inter-chain Coulomb repulsion. These results indicate that the long-range interaction on surfaces not only can influence the adsorption of individual adsorbates, but also could mediated the growth of self-assembled nanostructures, as for example gratings composed of metal-organic chains.

Strong DCV5T-Me$_2$ intermolecular interactions and coordination between DCV5T-Me$_2$ and Au atoms, inhibit the mixing of DCV5T-Me$_2$ with C$_{60}$ and coronene. And the orbital energy realignment induced by metal-ligand hybridization and inter-molecular interactions suppress the electron donor character of DCV5T-Me$_2$ when contacting with acceptor C$_{60}$ molecules.

Mixed structures can be formed by co-deposition of DCV5T-Me$_2$ and TCNQ on Au(111), which are stabilized by intermolecular hydrogen-bonds benefiting from the electronegative cyano groups at TCNQ. Moreover, charge transfer occurs at the DCV5T-Me$_2$/TCNQ interface, demonstrated by the sharp peaks and deeps in spectra at TCNQ molecules. Therefore, we propose that the mixed film of DCVnTs and TCNQ may also be a potential candidate for high efficiency organic solar cells.

4 DCV5T-Me$_2$ on Ag(111) and Cu(111) Surfaces

4.1 Introduction

In the last two chapters, we characterize structural and electronic properties of DCV5T-Me$_2$ on the Au(111) surface. Since its potential applications are based on the corresponding artificial architectures contacting with different metallic leads, it is crucial to understand the evolution of properties when adsorbing on various metal surfaces. The absorption of DCV5T-Me$_2$ on Ag(111) and Cu(111) is expected to differ from the features observed on the more inert Au(111) surface. First of all, the work function is different for these three substrates [159], which will simply shifts the orbital alignment in energy [38]. Secondly, the presence of different types of adatoms influences the self-assembled structures on metal surfaces [24]. Finally, the strength of hybridization between metal surfaces and organic molecules strongly varies from physisorption to chemisorption, modifying molecular geometry [25]. In addition, various degrees of charge transfer occurs between metal substrates and organic molecules, which dominates the structural and electronic properties of their interface [24].

In this chapter, we show that pure organic islands of DCV5T-Me$_2$ are formed upon physisorption on Ag(111), where molecular orbitals are rigidly shifted down with respect to on Au(111) due to the lower work function of Ag. In contrast, molecules assemble into metal-organic motifs by incorporating Cu adatoms on the Cu(111) surface through proper thermal activation. The strong hybridization between metal substrate and ligands eliminates the molecular resonances from the spectra. Accordingly, the chemisorption enables corresponding nano-structures to scatter and confine surface electrons, which are absent on the Au and Ag surfaces.

4.2 DCV5T-Me$_2$ on Ag(111)

4.2.1 Assembly Structure

The adsorption of DCV5T-Me$_2$ on Ag(111) shows a different result from that on Au(111). As shown in figure 4.1 a, large islands of DCV5T-Me$_2$ are formed there. The High resolution STM image in figure 4.1 b reveals that there are two types of
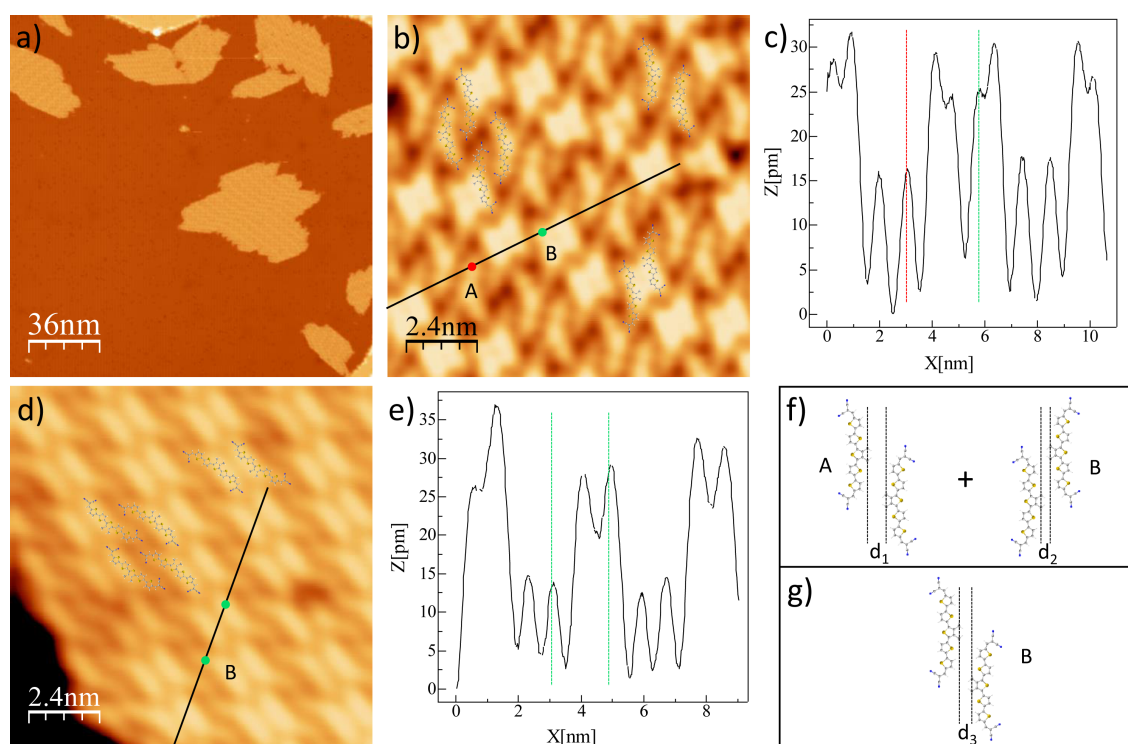
Figure 4.1: Self-assembly of DCV5T-Me$_2$ on Ag(111). a) Overview STM image of DCV5T-Me$_2$ islands (I = 15 pA and V = 0.78 V). b) and d) High resolution STM images (I = 70 pA and V = 0.79 V in b; I = 14 pA and V = 0.56 V in d) of islands with different molecular height contrast. c) and e) Line profiles showing the height of molecules in images b and d, respectively. f) and g) Models showing distances between neighboring molecules in images b and d, respectively. d$_1$ = 0.43 nm, d$_2$ = 0.22 nm and d$_3$ = 0.26 nm.

molecules with different height contrast upon packing in islands. One type exhibits homogenous contrast like on Au(111), named as type A. In contrary, for the other type, one side and the center of the molecule are imaged brighter than the other side, which are labeled as type B. The brighter part of type B molecule is 10 pm higher than type A (figure 4.1 c). Moreover, type B molecules arise in pair and the brighter contrast is localized at their contacting regions (model in right bottom corner of figure 4.1 b). Type A molecules emerge in pair as well, however, with larger intermolecular distance (model in right upper corner of figure 4.1 b). The intermolecular distance differs by a factor of 2 in two cases, as shown in figure 4.1 f. Therefore, we attribute the higher apparent height of type B molecules to the closer intermolecular distance, which probably forces molecules to point their methyl groups outwards from the surface. Islands consisting of only type B molecules are also observed on the surface, as shown in figure 4.1 d and e. In this case, the brighter contrast is induced by close intermolecular distance as well (figure 4.1 g). Additionally, the basic packing pattern on Ag(111) is the same as that in islands on Au(111) (compare models in figure 4.1 b and d with figure 2.2 c). Hence, we propose that intermolecular hydrogen-bonds and electrostatic interaction are also responsible

for the self-assembly. However, after the same sample preparation procedure as on Au(111), here no metal-organic structures (like chains) are formed.

Lateral manipulation [41, 160, 161, 162, 163, 164, 165, 166, 167, 168, 169] further demonstrates the dense packing origin of the intra-molecular contrast. After removing its neighbor, a type B molecule is transformed to type A molecule, where two sides of the molecule adsorb with the same height (figure 4.2 c and f). The same change happens to the resultant single molecule after dragging it out of the island (figure 4.2 b and e).
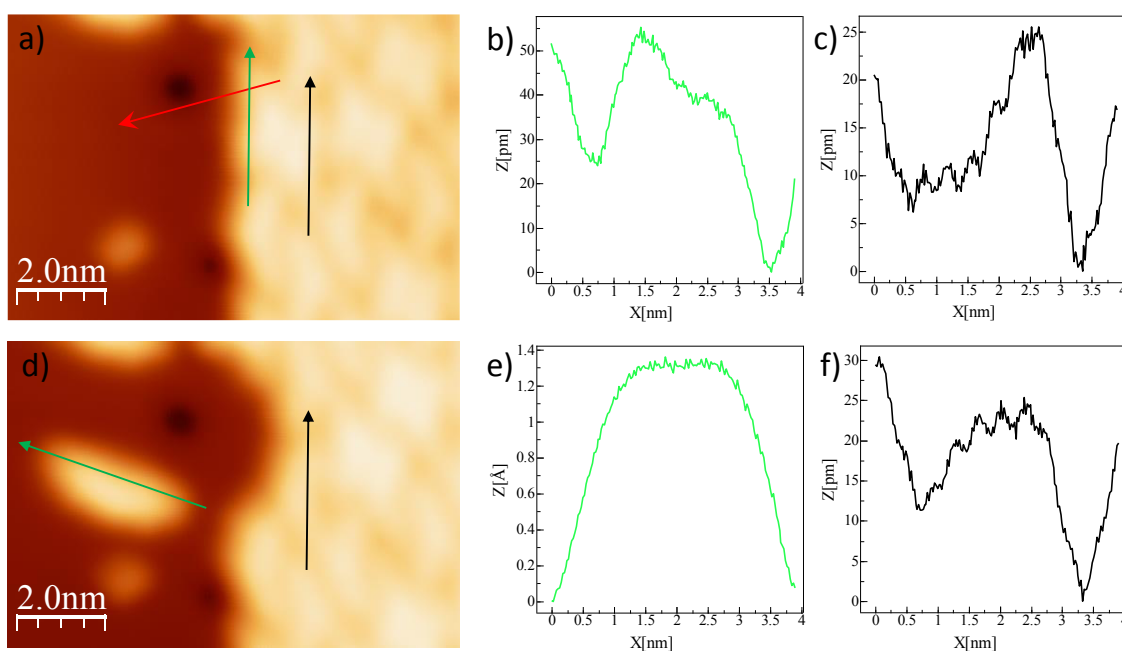
Figure 4.2: Contrast changes by lateral manipulation. a) and d) STM images (I = 20 pA and V = 0.76 V) before and after extracting a molecule from a compact domain (set point of the lateral manipulation: I = 100 nA and V = 0.01 V). The movement trace of the tip during manipulation is indicated by the red arrow in a. An intact single molecule is obtained after the manipulation. b) and c) Profiles show the height of two type B molecules before the manipulation. e) and f) Profiles show the height of the same molecules after the manipulation. The sides with arrows have bigger values in X axis in the profiles.

The self-assembled architectures on the Ag(111) surface differ from those on Au(111) in that they have different lateral interactions (table 4.1). The absence of metal-organic motifs on Ag(111) indicates that the interaction between Ag adatoms and cyano groups is weaker than intermolecular interactions. One would expect that Ag atoms should be more active than Au atoms. However, no coordination involving Ag atoms has been observed until now [8, 134, 170, 171, 172]. To unreveal the origin of this difference reactivity of Ag and Au adatoms is beyond the goal of this thesis, and would involve detailed first principles simulations including a precise description of the substrate density of states.

4.2.2 Electronic Properties

The single molecule is a good reference to study evolution of electronic properties of DCV5T-Me$_2$ upon self-assembly into islands. dI/dV spectra (figure 4.3 a) show that the LUMO at 1.4 V is mainly distributed at the central part of the single molecule with lower weight at the two sides, whereas the LUMO+1 at 2.2 V is localized at the two sides. This distribution is further imaged in the dI/dV maps shown in figure 4.3 b, and fits with the DFT calculated orbital structure of DCV5T-Me$_2$ in gas phase.
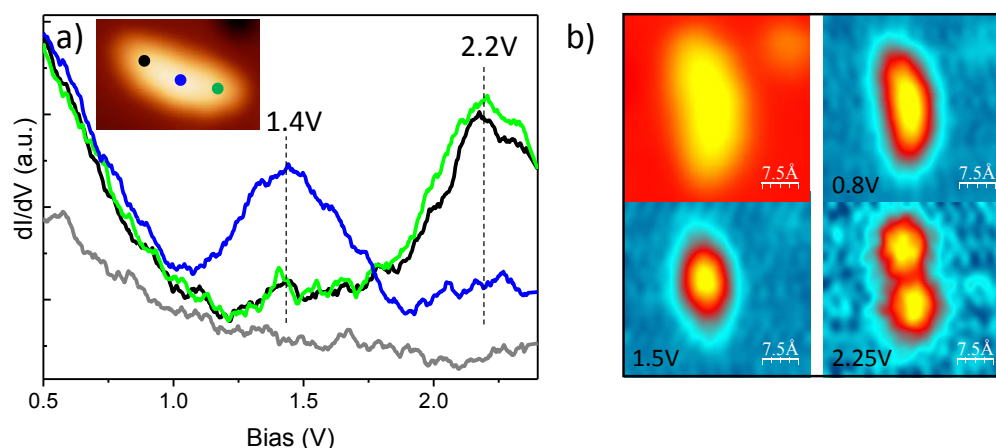

Figure 4.3: Electronic properties of the single molecule. a) dI/dV spectra acquired with closed feedback (set point: I = 8 pA and V = 2.4 V) at different locations of the single molecule as indicated inset. The energetic positions of the resonances in the dI/dV spectra are highlighted by the black dash vertical lines. b) Constant current STM images (left upper panel: I = 20 pA and V = 0.76 V) and corresponding constant height dI/dV maps (the other three panels) recorded at indicated biases. The currents are 40 pA, 31 pA and 9 pA from low to high bias, respectively.

The orbital energy alignment is changed upon self-assembly. Figure 4.4 a shows spectra recorded over a type A molecule within an island. Here, three resonances are observed. The state at 0.5 V is distributed over the whole molecule, while the resonance at 0.8 V is mainly located at the two sides. By comparing with the distribution of unoccupied orbitals over the single molecule, we assign these two states to the LUMO and LUMO+1. The downshift in energy with respect to the single molecule is ascribed to intermolecular interactions [19, 108]. In addition, the center possesses a higher-lying state at 1.5 V. Since calculations show the LUMO+2 located at the center of DCV5T-Me$_2$, this 1.5V resonance can be assigned to the down-shifted LUMO+2 after assembly. The type B molecule exhibits the same features, which can be demonstrated through dI/dV mapping (figure 4.4 b). The map acquired at 0.5 V shows similar contrast with the topography due to the delocalization of the LUMO, while signals are located at the two side and the center at maps taken at 0.7 V and 1.5 V corresponding to the LUMO+1 and LUMO+2, respectively.
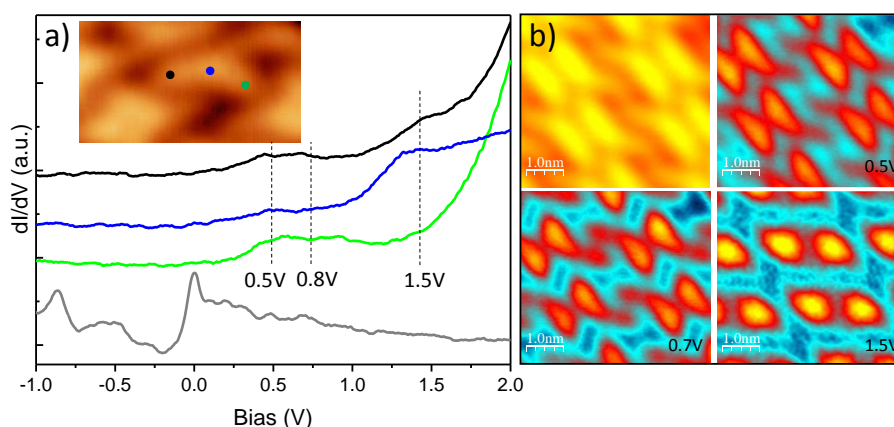
Figure 4.4: Electronic structure of the island. a) dI/dV spectra acquired with open feedback (set point: I = 50 pA and V = 2.0 V) at different locations of the molecule in an island as indicated inset (I = 16 pA and V = 0.8 V). Energetic positions of the resonances in the dI/dV spectra are highlighted by black dash vertical lines. All the spectra are offset for clarity. b) Constant current STM image (left upper panel: I = 14 pA and V = 0.56 V) and corresponding constant height dI/dV maps (the other three panels) recorded at indicated biases (50 pA).

Qualitatively, the behaviors of molecular islands on Ag(111) are the same as on Au(111). However, the exact values of orbital energies differ by 0.6 ± 0.2 V, as shown in table 4.2. The difference in quantity can be interpreted by considering the work function of surfaces. The work function of Ag(111) is lower by 0.57 V than that of Au(111) [159], which is in a good agreement with the down-shifted values of orbital energies. It means that organic islands physically adsorb on both substrates without significant hybridization at interfaces, resulting in only a rigid shift of orbital alignment [38].

4.3 DCV5T-Me$_2$ on Cu(111)

4.3.1 Adsorption and Assembly

The free molecular properties are not strongly modified by both the Au(111) and Ag(111) substrates. However, a copper surface is expected to induce drastic disturbance to the organic material through strong metal-ligand hybridization. It is found that the self-assembly of DCV5T-Me$_2$ on Cu(111) strongly depends on the substrate's temperature. At low temperature (180 K), single molecules or small clusters randomly disperse on the surface, as shown in figure 4.5 a. The high resolution STM image in figure 4.5 b shows that molecules adopt various configurations, due to lack of thermal-activated relaxation upon adsorption. Moreover, the two sides exhibit much lower apparent height than the small central part. It is probable that the end DCV groups and the thiophene backbone strongly interact with the surface pulling the two methyl groups in the center ring bent upward. Molecules
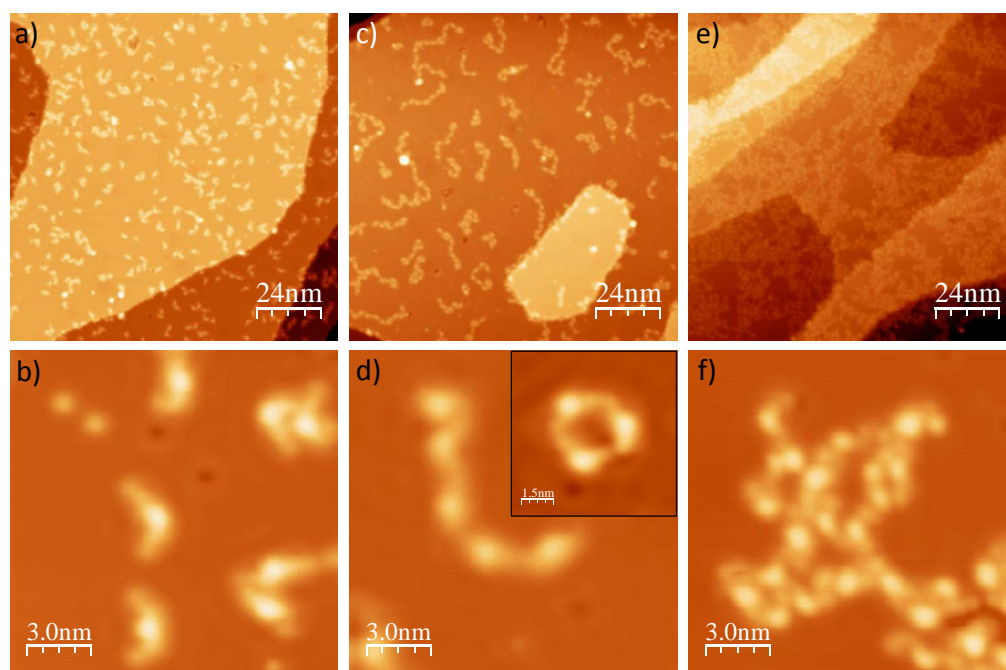
Figure 4.5: Adsorption and assembly of DCV5T-Me$_2$ on Cu(111). a), c) and e) Overview STM images (I = 23 pA and V = 0.33 V for a; I = 12 pA and V = 0.1 V for c; I = 100 pA and V = 0.62 V for e) of deposition of DCV5T-Me$_2$ on sample with different temperatures, 180 K, 230 K and 300K, respectively. b), d) and f) Corresponding high resolution STM images (I = 7.7 pA and V = 0.32 V in b; I = 8.1 pA and V = 0.1 V in d; I = 210 pA and V = 0.74 V for f). The inset in b shows a pore (I = 14 pA and V = 0.11 V) consisting of three molecules.

assemble into chains and pores when deposited on the substrate with higher temperature (230 K), as shown in figure 4.5 c. In these structures, adjacent molecules connect with each other *via* their ends (figure 4.5 d). Therefore, we propose that Cu adatoms are incorporated for bridging the electronegative end cyano groups [122, 172, 173, 174, 175, 176]. Differently from pure organic islands on Ag(111), the formation of pure metal-organic motifs on Cu(111) means that the interaction between Cu adatoms and cyano groups is much stronger than intermolecular interactions. Disordered clusters are formed when depositing molecules on room temperature sample (300 K), as shown in figure 4.5 e. The high resolution STM image in figure 4.5 f reveals that most of molecules are not intact. The decomposition can be attributed to bond dissociation probably catalyzed by Cu adatoms on the Cu surface [177].

Lateral manipulations were performed to get more insight into the adsorption and assembly behaviors of DCV5T-Me$_2$ on Cu(111). Figure 4.6 a - c show a lateral manipulation sequence of a single molecule on cold sample (180 K). One can identify that after manipulation two small dots stay on their original positions, while the molecular backbone (figure 4.6 d) are moved away by the tip. It demonstrates that the end cyano groups are pinned at the surface upon adsorption due to strong
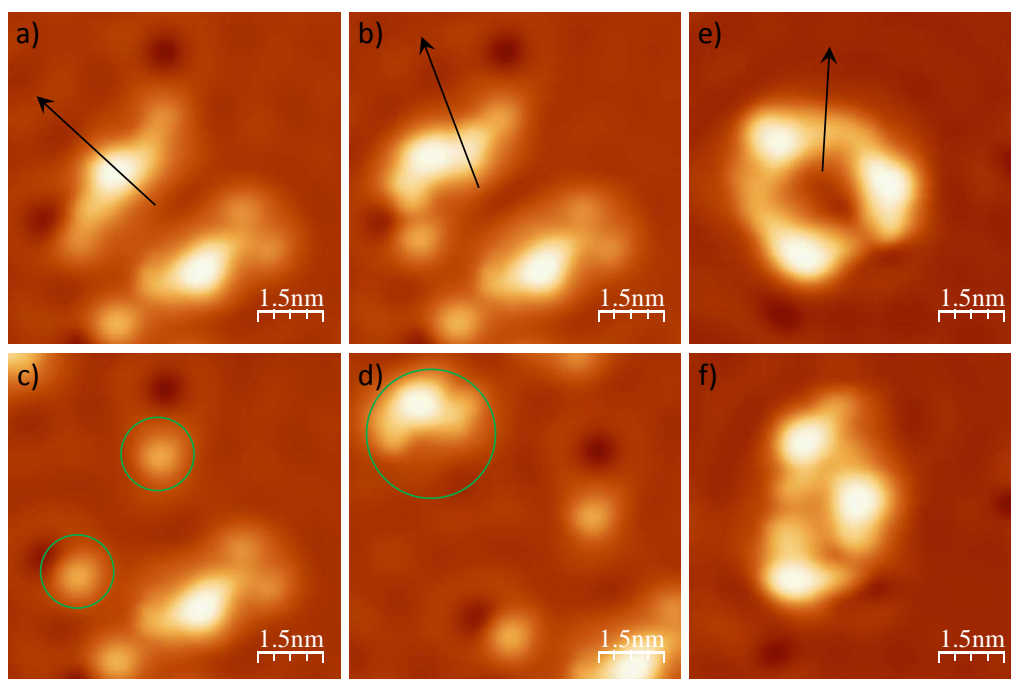
Figure 4.6: Lateral manipulation. a) - c) STM images (I = 100 pA and V = 0.1 V) of a lateral manipulation sequence on a single DCV5T-Me$_2$. d) STM image (I = 100 pA and V = 0.1 V) of the dissociated molecule after manipulation. Green circles in c and d highlight the DCV groups and the backbone of the molecule, respectively. e) and f) STM images (I = 14 pA and V = 0.11 V) before and after a lateral manipulation on a three-molecule pore. During lateral manipulation the movement trace of the tip is indicated by black arrows in the STM images.

interaction with the Cu atoms underneath. The interaction is even stronger than the covalent bonds within DCV5T-Me$_2$, thereby dissociating the molecule during lateral manipulation. In contrast, lateral manipulation on a pore consisting of three molecules shows different phenomenon. The whole structure is dragged to another position by the tip. Although configurations are changed, molecules keep intact and are still connected *via* ends. It further certifies the incorporation of Cu adatoms by ligands due to thermal activation at moderate temperature (230 K) sample. As a result, lateral coordination bonding dominates over vertical interactions, which is so robust that the metal-organic motif can be lateral manipulated as a whole without dissociation. Note that the same phenomenon happens when manipulating the chain, indicating its combination of molecules with Cu adatoms.

We performed STS at DCV5T-Me$_2$ on Cu(111) to inspect its electronic structure. In contrast to the rich spectral information obtained when adsorbed on Au(111) and Ag(111), there is no feature in the bias range from -1.3 V to +2.0 V (figure 4.7) due to the strong hybridization with Cu surface [24]. Note that the absence of resonances is ubiquitous for spectra recorded at molecules in different assemblies and different positions of a same molecule.
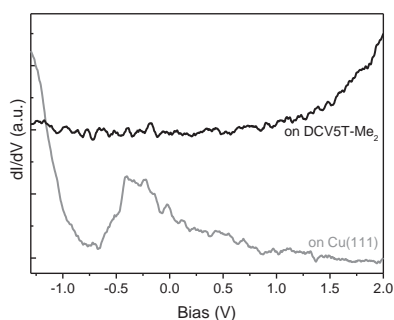
Figure 4.7: dI/dV spectra acquired with open feedback (set point: I = 20 pA and V = 2.0 V) at DCV5T-Me$_2$ showing no feature from -1.3 V to +2.0 V.

4.3.2 Scattering and Confinement of Surface Electrons

The strong interaction between molecules and substrates enables scattering of surface electrons [103, 178]. Figure 4.8 a shows standing waves surrounding a single molecule. The oscillation period is around 15 Å (figure 4.8 b) corresponding to half the Fermi wavelength (λ_F) of the Cu(111) surface. Similarly, the metal-organic chains also can serve as a scattering center, as shown in figure 4.8 c and d. This behavior is absent on Au(111) and Ag(111) because of weaker interactions between surfaces and ligands.
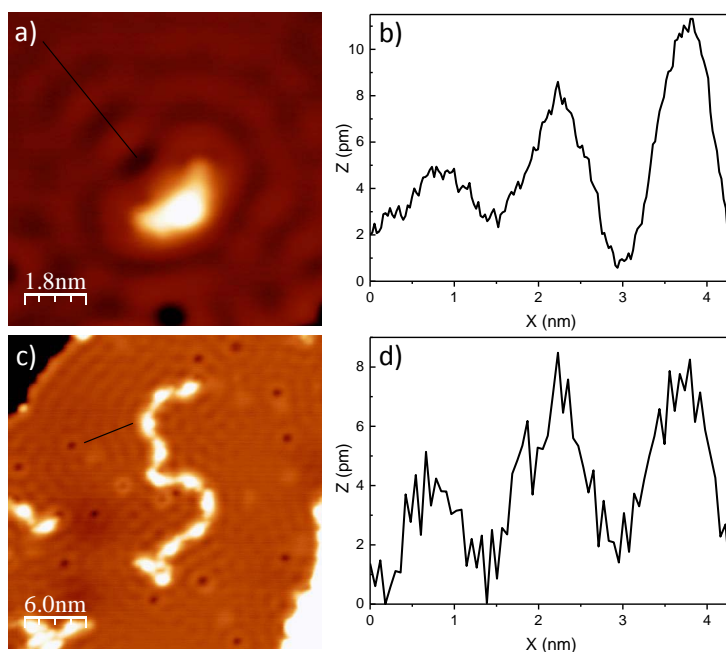
Figure 4.8: Scattering surface electrons. a) and c) STM images (I = 16 pA and V = 0.14 V for a; I = 74 pA and V = 0.1 V for c) of standing waves formed through scattering surface electrons by a single molecule and a chain, respectively. b) and d) Linescans (indicated by the black line in a and c) showing the wavelength (15 Å) of the standing waves.

Consequently, surface electrons will be confined within the corresponding sealed structures [102, 162, 179, 180, 181], for example, the metal-organic pores. As shown in figure 4.9 a - c, electrons are localized at pores consisting of three and four molecules, respectively. Pores with different size have different eigenstates. dI/dV spectra were recorded at the center of pores, with sizes ranging from three to six molecules (figure 4.9 a, d and e), to inspect the energy shift of confined surface electrons. The first eigenstate is monotonously shifted down from -130 meV to -360 meV as the pore size increases, as shown in figure 4.9 f. This phenomenon can be interpreted by the quantum mechanism of particle in two dimentional circular box [102, 182]. The eigenstate of order (m, n_r+1) of electron gas confined in a box, can be described as $E = [\hbar^2/2m_e R^2][a_{(m,n_r)}]^2 + E_s$ [183], where m_e is the electron effective mass, R is the radius of the circle, $a_{(m,n_r)}$ can be calculated from the Bessel function and E_s is the natural onset of the surface state (-450 meV for Cu(111)). Therefore, in energy the ground state of confined electrons is gradually shifted down to the surface state from the pore with smaller radius to that with bigger radius [1], associated with weaker confinement effect. The self-assembly of different size of sealed nano-structures on metal surfaces offers a way to fabricate tunable surface electron states.
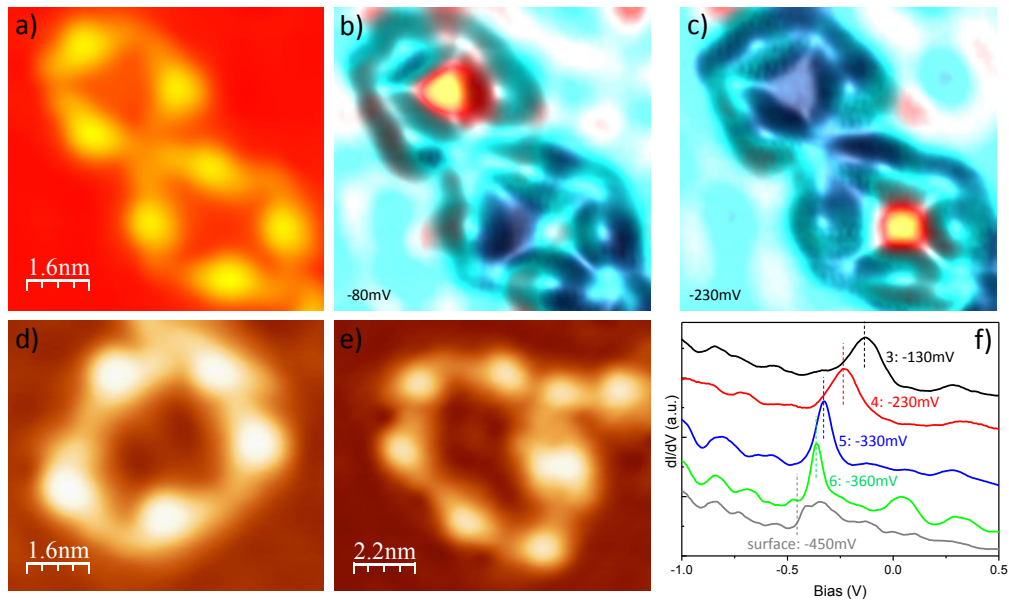
Figure 4.9: Confinement of the surface electrons in the metal-organic pores. a) STM image of two pores consisting of three and four molecules (I = 80 pA and V = -0.23 V). b) and c) Corresponding constant current dI/dV maps recorded at indicated biases (80 pA). The dI/dV signals (yellow and red) are superimposed over the topography (cyan). d) and e) STM images of two pores consisting of five and six molecules, respectively. f) dI/dV spectra acquired with open feedback (set point: I = 80 pA and V = 1.0 V) at the center of pores consisting of different number of molecules, from three to six. The energetic positions of the resonances in the dI/dV spectra are highlighted by the dash vertical lines. All the spectra are offset for clarity.

---

[1]Here we treat the pores as circles.

4.4 Conclusions

DCV5T-Me$_2$ exhibits different self-assembly behaviors on Au(111), Ag(111) and Cu(111) as the result of competition of lateral interactions between molecules, and between molecules and adatoms on surfaces, as summarized in table 4.1. Pure organic islands and metal-organic chains are formed on the Au(111) substrate simultaneously, because intermolecular interactions are comparable with the molecule/Au-adatom coordination bonding. In contrast, only organic islands are assembled on Ag(111), where coordination involving Ag adatoms is always absent. Differently, molecule/Cu-adatom coordination dominates the structure formation when deposited on Cu(111), inducing homogenous metal-organic motifs on the surface.

Vertical interactions between molecules and surfaces vary as well. DCV5T-Me$_2$ physically adsorbs on Au(111) and Ag(111), while chemisorption occurs on Cu(111), inducing scattering and confinement of surface electrons. Molecular electronic properties evolve accordingly, as summarized in table 4.2. Molecular orbital alignment is rigidly shifted down on Ag(111) with respect to on Au(111) due to lower work function. In contrast, molecular resonances vanish on Cu(111) owing to strong organic/metal hybridization. The changes of structural and electronic properties of DCV5T-Me$_2$ assemblies on different metal substrates should draw our attention when building corresponding organic electronics.
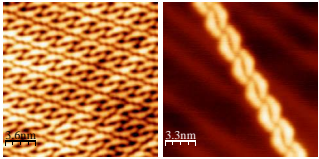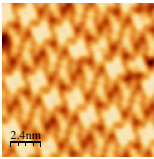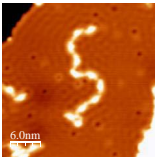
Au(111)	Ag(111)	Cu(111)
intermolecular interactions are similar with molecule/Au-adatom interaction in strength	intermolecular interactions are stronger than molecule/Ag-adatom interaction in strength	intermolecular interactions are weaker than molecule/Cu-adatom interaction in strength

Table 4.1: Evolution of self-assembly structure of DCV5T-Me$_2$ on Au(111), Ag(111) and Cu(111): the competition of lateral interactions.

Surface	Adsorption	Work function (eV)	L$_{single}$ (V)	L+1$_{single}$ (V)	L$_{island}$ (V)	L+1$_{island}$ (V)	L+2$_{island}$ (V)
Au(111)	physisorption	5.31	2.0	>2.6	1.3	1.6	2.3
Ag(111)	physisorption	4.74	1.4	2.2	0.5	0.8	1.5
		0.57	0.6	>0.4	0.8	0.8	0.8
Cu(111)	chemisorption	4.94	no feature from -1 V to +2 V at either single molecules or chains				

Table 4.2: Energy alignment of unoccupied molecular resonances of DCV5T-Me$_2$ on Au(111), Ag(111) and Cu(111). Values in the fourth row (red) are the differences of molecular orbitals in voltage between on Au(111) and Ag(111).

5 Structural and Electronic Properties of DCV6T on Au(111)

5.1 Introduction

Molecular recognition plays a crucial role in the biological systems, for example in DNA binding and enzyme catalyzing. Inspired by the nature, scientists utilize it to design and fabricate artificial supramolecular architectures [3]. Molecular recognition can be classified into static mode and dynamic mode [184]. In static recognition, the structures of bonding sites at reactant molecules are directly complementary, which is interpreted by the lock-and-key theory [10, 11, 12]. In the case of dynamic recognition, the configuration of one molecule is changed to fit best with the partner molecule in bonding structure and obtain the maximum bonding strength. Since the change of configuration is induced by the presence of the partner, this mechanism is termed "induced fit theory" [10, 11, 12].

Recently, the lock-and-key effect has been studied with sub-molecular resolution using STM [3]. It dominates the intermolecular bonding structure in the supramolecular architectures [185] and even the adsorption of individual molecules on metal surfaces [186]. However, a real-space investigation and microscopic understanding of the induced fit effect is rarely reported so far, because molecules trend to stick on metal surfaces becoming not flexible enough for deformation during recognition.

The first part of this thesis has shown that the overwhelming majority of DCV5T-Me$_2$ adopt a same configuration upon adsorption on the Au(111) surface, even when incorporated within different types of architectures. The uniformity of configuration of DCV5T-Me$_2$ is attributed to the attachment of side methyl groups, which hinder the rotation of the central thiophene rings reducing the degree of freedom of the molecular geometry. In contrast to DCV5T-Me$_2$, DCV6T is more flexible benefiting from the longer thiophene backbone and absence of side-groups. Therefore, it is expected that DCV6T molecules will exhibit diverse configurations within different kinds of self-assemblies on the Au(111) surface. Based on the measurement of DCV5T-Me$_2$, it is reasonable to estimate that hydrogen bonding and electrostatic interactions exist in the assemblies of DCV6T as well. These strong intermolecular interactions may cause significant deformation to the flexible organic molecules. Therefore, DCV6T should be a good candidate to study the induce fit effect.

In the first part of this chapter, we investigated how the intermolecular interactions determine the self-assembly of DCV6T molecules on Au(111) by using STM/AFM imaging combined with DFT calculations. DCV6T molecules self-assemble into organic islands, organic chains and metal-organic chains with Au adatoms simultaneously on the surface with different configurations. AFM imaging reveals that the formation of islands is in response by the lock-and-key effect, while induced fit effect dominates the assembly of molecules in chains with an energetically unfavored bent configuration.

In the second part of this chapter, STS is utilized to investigate the electronic properties of DCV6T assemblies. It is found that intermolecular interactions and Au-CN hybridization induce modifications to molecular orbitals, like in the Au-DCV5T-Me$_2$ case.

3d transition metal atoms can form metal-organic nanostructures through coordination bonding with molecules [8, 134, 135, 171], which exhibit fascinating perspectives for future nanoscale devices [9, 187]. In the third part of this chapter, metal-organic chains consisting of Co atoms and DCV6T are fabricated. Lower-lying states in positive polarity are localized at the sides of molecules, which are attributed to hybridization between the Co 3d states and molecular orbitals. Surprisingly, both the spatial distribution and energetic alignment of the unoccupied molecular orbitals are not influenced by the formation of coordination. The intactness of conduction bands of organic semiconductor DCV6T after contacting with metallic leads would benefit its application in organic electronics.

5.2 Molecular Recognition: from Static to Dynamic

5.2.1 Self-assembled Motifs of DCV6T

With respect to DCV5T-Me$_2$, the assembly of DCV6T on Au(111) is more complicated due to the bigger degree of freedom of the molecular backbone. Large islands and two different types of chains are formed on the surface simultaneously (figure 5.1 a). High resolution STM image (figure 5.1 b) reveals that molecules within the islands adopt a straight and anti-symmetric configuration, which nicely fits with the most stable geometry from DFT calculations of the isolated molecule in gas phase. This structure is formed by alternating orientation of thiophene rings and intra-molecular CN-S interactions. Similarly with the DCV5T-Me$_2$ islands, DCV6T molecules connect to adjacent molecules in the same row end-to-end and from the neighboring rows end-to-center. Therefore, we believe that the formation of DCV6T islands should be attributed to the intermolecular hydrogen-bonds and electrostatic interaction as well. The surface reconstruction underneath the islands appears intact, indicating a weak interaction between the DCV6T and the metal surface [28].
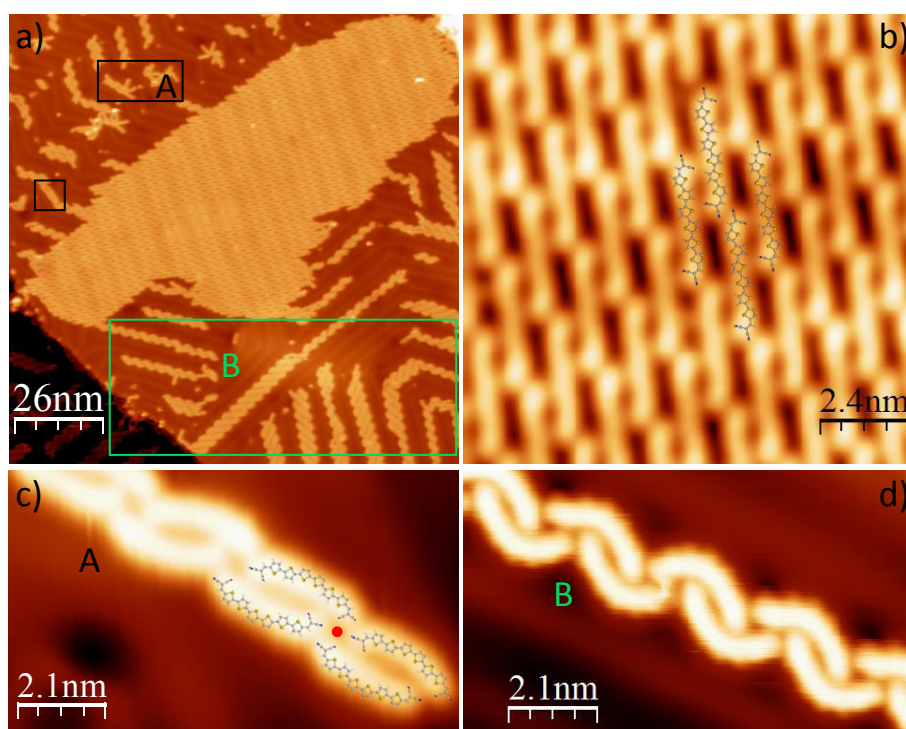
Figure 5.1: Self-assembly of DCV6T on Au(111). a) An overview STM image (I = 72 pA, V = 0.82 V) of the self-assembled structures. Molecular islands and chains exist on the surface simultaneously. The herringbone underneath the islands survives. The short chains (tpye A) in the black squares grow across the herringbone, while the long chains (type B) in the green square grow in the fcc region of the surface reconstruction. b) A high resolution STM image (I = 47 pA, V = 0.85 V) of the island. Molecules within the island adopt straight and anti-symmetric configuration. c) A high resolution STM image (I = 87 pA, V = 1.13 V) of the type A chain. Molecules within the chain are straight and symmetric. The model suggests that Au adatoms (red circle) are incorporated inside. d) A high resolution STM image (I = 110 pA, V = 0.85 V) of the type B chain. It is difficult to determine the exact configurations and bonding structures of molecules within the chain from the STM image alone.

Both types of chains are composed of two parallel rows of molecules. One of them aligns across the Au(111) herringbone reconstruction (in the black rectangles in figure 5.1 a), labeled as type A chain. While the other type grows in the fcc region of the surface reconstruction (in the green rectangle in figure 5.1 a), which is labeled as type B chain. Contrary to the case of DCV5T-Me$_2$ on Au(111), here DCV6T within both types of chains adopts completely different configurations than within islands. Molecules within the type A chain adopt straight and (almost) symmetric configuration. DFT calculations suggest that the two central thiophene rings are oriented to the same direction in this configuration (figure 5.1 c). The fact that the cyano groups from adjacent four molecules point to one site implies the existence of a metal bridge. Based on the studies on DCV5T-Me$_2$ chains, we propose that Au adatoms are also incorporated within the type A chain forming four-fold metal-organic motifs. Molecules within the type B chain are bent and asymmetric

(figure 5.1 d). In contrast to the bonding structure in the type A chain, here the molecular ends avoid each other, and instead appear to connect to other parts of the neighboring molecules rather than the CN ends. This fact implies that the type B chain is a pure organic motif without incorporation of Au adatoms. However, it is difficult to determine from STM images its exact bonding structure, even the configuration of the molecules themselves. Therefore, AFM was employed. Since the metal-organic chains (type A) hold very few DCV6T molecules, in this chapter we focus on imaging the type B chain and compare it with the molecular island.

5.2.2 Static Molecular Recognition in DCV6T Islands

Figure 5.2 a and b show the STM image of an island recorded with a Xe functionalized tip and the corresponding (constant height Laplace filtered) AFM image, respectively. The thiophene rings and DCV groups of DCV6T are resolved at atomic resolution, showing nitrogen atoms and sulfur atoms with brighter contrast. This is due to the abundance of electrons at these two elements, inducing stronger Pauli repulsive interaction with the closely-approached tip. We find that the six thiophene rings are oriented alternately and one of the cyano groups in the DCV is located in the vicinity of the sulfur atom from the adjacent thiophene ring. The DFT optimized geometry of the free molecule can fit with the configuration imaged by the AFM very well, as shown in figure 5.2 b (in copper color). It means that the configuration of the DCV6T molecules is not perturbed upon adsorption and assembly by the surface mediation and the intermolecular interactions. This is further demonstrated by the fact that optimized geometry of a pair of DCV6T molecules in gas phase (calculation details are following) also matches with the experimental data (figure 5.2 b in normal color code).

AFM also resolves bright lines at positions where intermolecular interactions are expected [17, 89, 90]. Based on these contrast and the molecular chemical structure, the bonding model of the island can be determined, shown in figure 5.2 c. The intermolecular interactions can be classified as: out-of-direction hydrogen-bonds (red dash lines), directional hydrogen-bond (red solid line) and CN-S interaction (green dash line). The DFT calculated charge distribution over a molecular pair with optimized geometry reveals that the nitrogen atoms at the cyano groups are negatively charged, while the sulfur atoms at the thiophene rings are positively charged, as shown in figure 5.3 b. Therefore, the CN-S interaction is electrostatic in nature. This electrostatic interaction also exists between the cyano group and its neighbor thiophene ring within individual molecules (blue dash line), which locks the orientation of the DCV group in the DCV6T molecules.

DFT calculations offer deeper insight for understanding and characterizing the intermolecular bonding. To simulate the chain, we optimize the bonding geometry of a pair of molecules by placing two optimized free molecules close to each other to generate the input configuration followed with being relaxed to a global energy
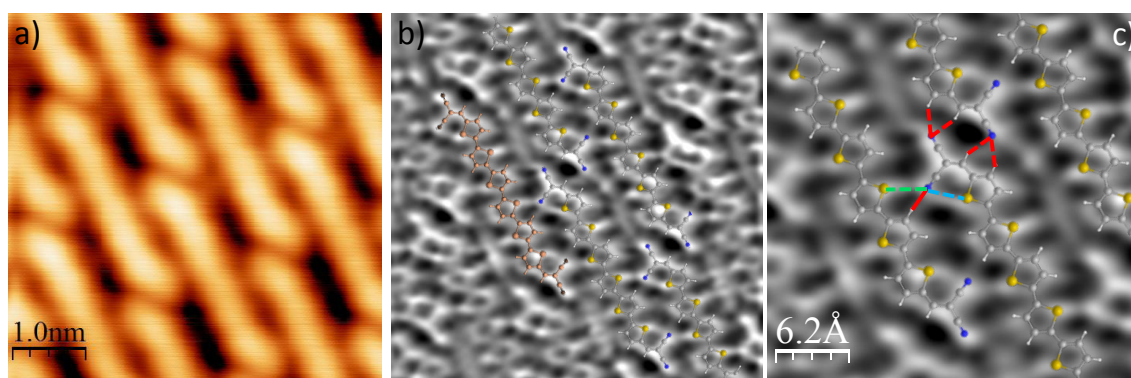
Figure 5.2: AFM imaging DCV6T molecular island. a) STM topography (I = 12 pA and V = 0.1 V) of an island. b) Corresponding Laplace filtered frequency shift image measured with a Xe functionalized tip and acquired in constant height mode. The tip is approached by 1.9 Å to the sample from the current set point of 12 pA and 0.1 V over the molecule. The DFT calculated configurations of a single molecule (in copper color) and a molecular dimmer (in normal color code) are superimposed. c) AFM image superimposed with the bonding model: out-of-direction hydrogen-bonds (red dash lines), directional hydrogen-bond (red solid line) and CN-S electrostatic interaction (green dash line). The blue dash line indicates intramolecular electrostatic interaction.
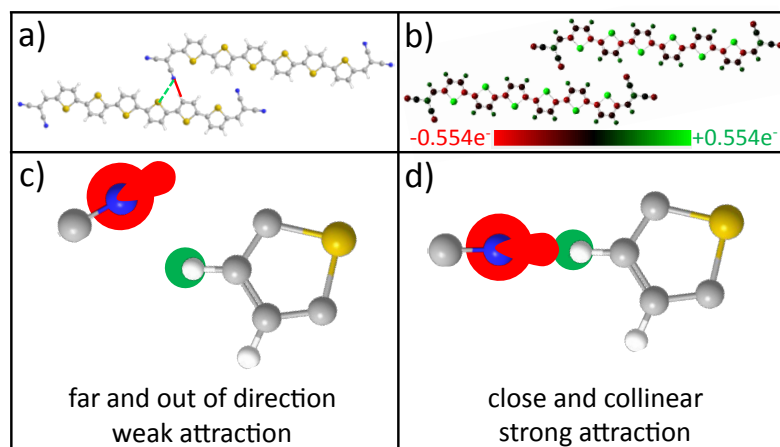
Figure 5.3: Directivity of the intermolecular hydrogen-bonds. a) The optimized configuration of a pair of molecules from DFT calculation. b) The DFT calculated charge distribution of a DCV6T dimmer. c) - d) Models showing the shape of electron clouds localized at the cyano ligand and CH group. The red color represents electron accumulation and the dark blue stands for electron depletion.

minimum [1]. In the optimized molecular pair (figure 5.3 a), the cyano group approaches the CH at the thiophene ring in such a way that they are located in line.

---

[1]The relaxed structure is independent on the relative positions of two molecules in the input configuration.

The distribution of the electron cloud over the cyano ligand and the CH group is employed to understand this bonding configuration. The nitrogen atom possesses one pair of lone-pair electrons, which are located at the extension of the C≡N bond (figure 5.3 c). The hydrogen atom has more positive charge at the side pointing away from the C-H bond (figure 5.3 c). Therefore, only when the CH and the C≡N are placed collinearly can the bonding strength be maximized (figure 5.3 d). This result demonstrates that the bond angle is also significant for the formation of hydrogen-bonds in addition to bond length.

The above chemical feature of hydrogen bonding facilitates the self-assembly of the island. According to the lock-and-key theory (figure 5.4 a), the intermolecular recognition is based on the match of specific patterns of two reacting sites. For the case of DCV6T, one pair of CN-HC bonding (figure 5.4 b: lock 1 - key 1) locks the relative positions of two adjacent molecules. Moreover, benefiting from the anti-symmetric shape of the molecule, the linear alignment is simultaneously satisfied at other bonding sites (figure 5.4 b: lock 2 - key 2). Therefore, the optimized bonding geometry can be obtained without influencing the intramolecular configuration of individual molecules and the lock-and-key effect extends. So here DCV6T molecules optimize their assembly structure in the island through static molecular recognition, dominated by directional intermolecular hydrogen bonding.
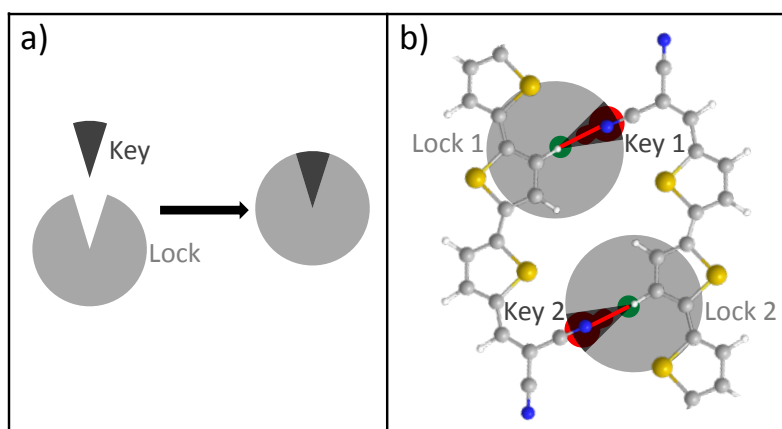
Figure 5.4: a) Model of the lock-and-key theory. b) Application of the lock-and-key theory to the self-assembly of DCV6T within islands.

5.2.3 Dynamic Molecular Recognition in DCV6T Chains

AFM is also utilized to determine the chemical configuration and bonding geometry of the type B chain. Figure 5.5 a and b show the STM image of a chain acquired with a Xe functionalized tip and the corresponding Laplace filtered AFM image, respectively. The chemical structure of the molecules within the chain is resolved with atomic resolution. The cyano groups and the sulfur atoms exhibit stronger contrast as well. Note that adjacent cyano groups point to different directions
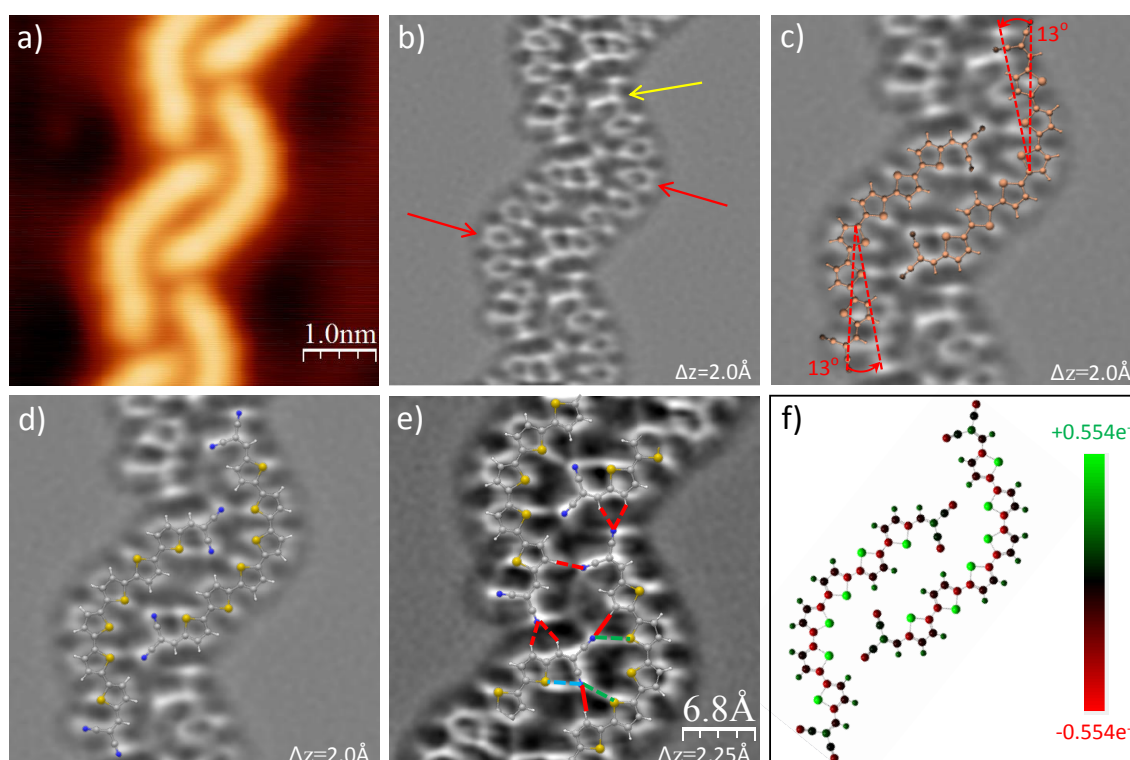
Figure 5.5: AFM imaging DCV6T molecular chain. a) STM topography (I = 12 pA and V = 0.1 V) of a type B chain measured with a Xe functionalized tip. b) Corresponding Laplace filtered AFM image acquired in constant height mode. The tip was approached by 2.0 Å to the sample from the current set point of 12 pA and 0.1 V over the molecule. The red arrows and the yellow arrow highlight the rotated thiophene rings and DCV group, respectively. c) DFT calculated configurations of single molecules in gas phase can not fit with the AFM image. d) DFT calculated configuration of a pair of molecules in gas phase can fit with the AFM image very well. e) Laplace filtered AFM image measured with the same Xe functionalized tip approached by 2.25 Å from the current set point of 12 pA and 0.1 V over the molecule. The bonding model is superimposed: out-of-direction hydrogen-bonds (red dash lines), directional hydrogen-bonds (red solid lines) and CN-S electrostatic interaction (green dash lines). The blue dash line indicates intramolecular electrostatic interaction. f) Calculated total charge distribution of a pair of molecules.

indicating that no Au atoms are incorporated. Hence, the type B chains are pure organic architectures. Here molecules exhibit asymmetric configuration with a large curvature compared with those in the islands. AFM imaging resolves that this is induced by the rotation of one central thiophene ring (red arrows in figure 5.5 b) to the same orientation as its two neighbor rings. In addition, a rotation of one DCV group (yellow arrow in figure 5.5 b) of the molecules at the right row introduces difference in geometry with respect to the molecules at the left row. From the AFM data, we know that molecules within the type B chains adopt bent, asymmetric and two different types of configurations.

By using the orientation of the thiophene rings and DCV groups from AFM images, we calculate the DCV6T geometry. Figure 5.5 c shows the DFT optimized configurations of the single molecules in gas phase. Such bent configuration also has a stable minimum energy structure. By superimposing them over the AFM image, one can identify that the calculated configurations can not fit with the experimental data. The comparison reveals that the molecules bend themselves about 13° more upon adsorption and self-assembly with respect to calculated single molecules. The larger bending could be induced by either the interaction with the metal surface or by the intermolecular interactions, or both.

We place the two optimized single molecules near each other in calculations to inspect the effect of intermolecular binding on the molecular configuration. As shown in figure 5.5 d, the optimized geometry of the molecule pair in gas phase fits with the measurement very well. This fact demonstrates that the bigger bending angle of DCV6T in the chain is induced by the intermolecular interactions.

The molecular packing structure also can be determined based on the AFM imaging, shown in figure 5.5 e. As in the islands, directional and out-of-direction hydrogen-bonds and electrostatic interactions (figure 5.5 f) are responsible to the formation of chains.
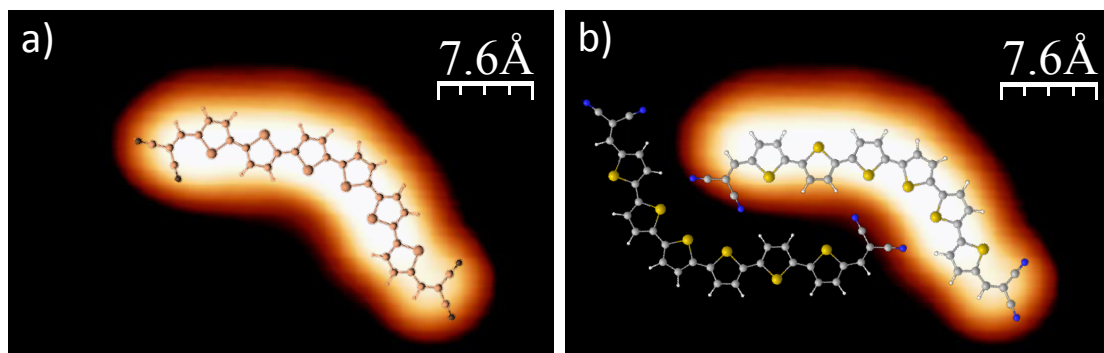
Figure 5.6: a) and b) The same STM images of a single molecule with a rotated thiophene ring (I = 100 pA, V = 0.8 V). The calculated configuration of the free molecule in gas phase fit with the STM image very well (a), while the calculated geometry of a pair of molecules can not fit (b).

To study the influence of substrate on the molecule configuration, we image the isolated bent DCV6T on Au(111) with STM [2]. The calculated configuration of the free molecule with one rotated thiophene ring in gas phase fits with the STM image very well (Figure 5.6 a), whereas the calculated geometry after taking intermolecular interactions into account can not fit (Figure 5.6 b). This fact confirms that the more bending of molecules within chains is indeed induced by the intermolecular interactions rather than the surface mediation.

---

[2]It is impossible to image the isolated molecules with AFM, since the strong forces between the AFM tip and the molecule induce lateral diffusion.
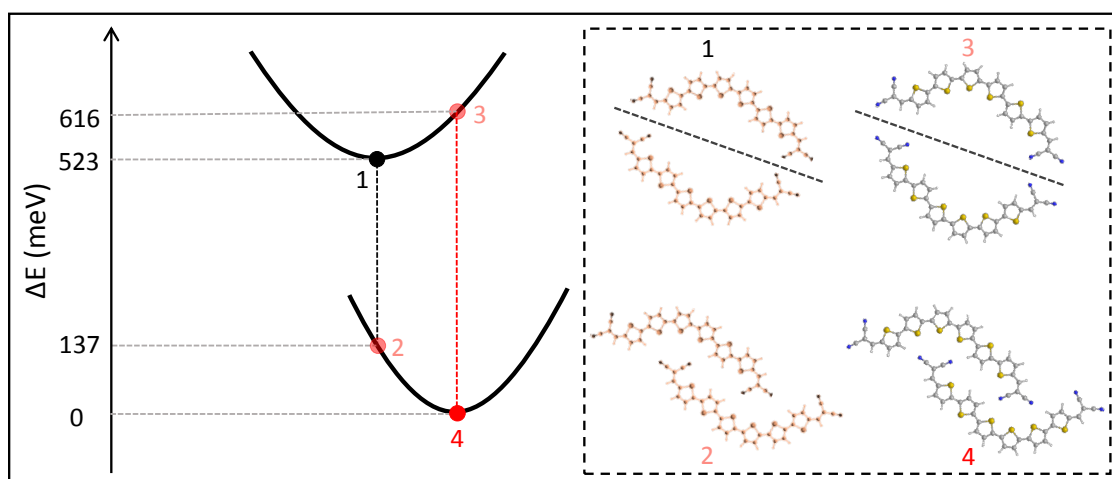
Figure 5.7: Quantifying energies of molecules with different configuration and bonding geometry. In particular, we calculated energies for four different binding structures: two optimized isolated molecules without bonding (1), two optimized molecules with bonding (2), two deformed isolated molecules without bonding (3), two deformed molecules with bonding (4) whose total energy is set as the zero point for comparing. In all the calculations, the surface is not considered due to its negligible influence on the system relaxation.

In order to get more insight into the molecular deformation upon binding, we calculate the energies corresponding to different bonding geometry with different molecular configuration, shown in figure 5.7. The system with two optimized molecules can relax to an energy minimum status with a binding energy of 386 meV (from 1 to 2), while the intramolecular deformation is forbidden during binding. If the change of molecular configuration is allowed, these two molecules will adapt themselves to a more bent geometry (as observed in our AFM data) for optimal intermolecular interaction with a total energy of 93 meV stored in the backbones (from 1 to 3). However, the bending enables the system to gain a binding energy of 616 meV (from 3 to 4). Therefore, in the end the whole system is relaxed to a more stable state (137 meV) than the case without change of molecular configuration (from 2 to 4).

The deformation of DCV6T upon self-assembly in chains can be interpreted with the induced fit theory (figure 5.8 a). For the initial configuration (copper color), the CN ligand aligns collinearly with the CH group at the bonding position 1 (figure 5.8 b: lock 1 - key 1) forming a directional hydrogen-bond. Whereas, the binding between lock 2 and key 2 (orange dash line in figure 5.8 b) is not optimized due to the large distance between CN and CH accompanied with a small alignment angle. Therefore, the backbone of the molecule has to be bended more so that the optimal bonding geometry can be realized there. Although the state of individual molecules is unfavorable energetically, the whole system is relaxed to the energy minimum due to the optimized intermolecular bonding. In this dynamic way, the bent DCV6T molecules recognize each other and form the type B chains.
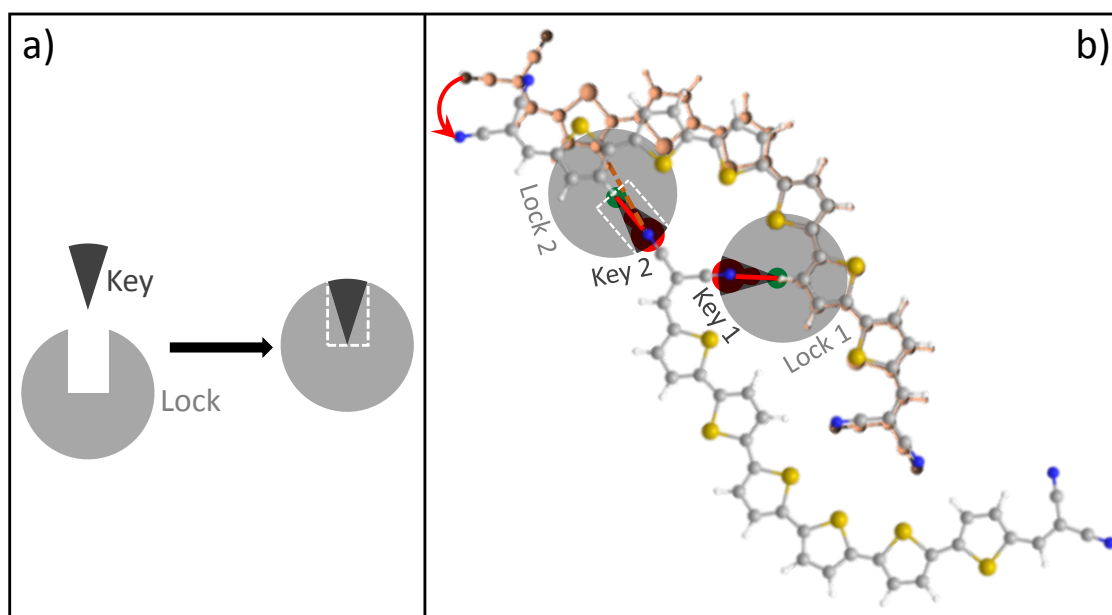
Figure 5.8: a) The model of induced fit theory: the configuration of the lock is changed by the presence of the key for obtaining maximum bonding. b) Application of the induced fit theory to the self-assembly of DCV6T within chains. A DCV6T is bended more to get the best fit with the adjacent molecule.

5.3 Electronic Properties of DCV6T Assemblies

We have characterized the chemical and packing structure of DCV6T on Au(111) using combined STM/AFM and DFT calculations. Since the molecular electronic features determine the performance of corresponding organic devices, it is also significant to evaluate its orbital structure (energy alignment and spatial distribution) in various assemblies through STS measurements.

5.3.1 The Single Molecules

Before molecular islands and chains, single molecules are investigated first as a reference for comparison. Figure 5.9 a shows the STM image of a single DCV6T, which adopts a bent configuration due to the big molecular flexibility. The corresponding dI/dV spectra (figure 5.9 b) reveal that the LUMO at 2.0 V is distributed over the whole molecule with higher weight at the center, while the LUMO+1 at 2.6 V is only localized at its two sides. This spatial distribution of the LUMO and LUMO+1 can be further imaged by dI/dV mapping, as shown in figure 5.9 c. Figure 5.9 d represents the structure of unoccupied molecular orbitals from DFT calculations in gas phase, which is in good agreement with the experimental observation. It indicates that the orbital structure of DCV6T is not strongly modified upon adsorption on the Au(111) surface.
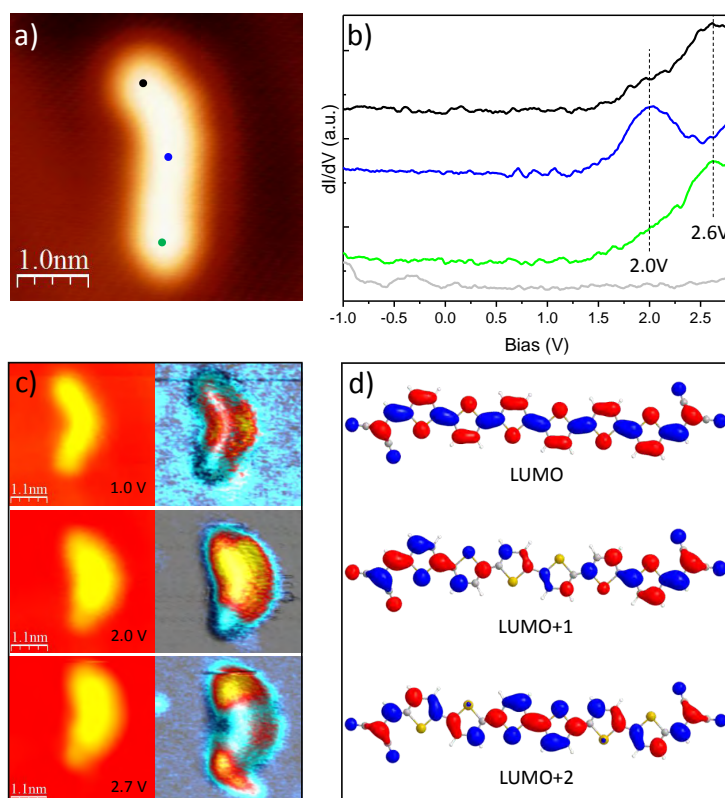
Figure 5.9: Electronic structure of the single DCV6T. a) STM image (I = 61 pA and V = 0.56 V) of a single molecule on Au(111). b) dI/dV spectra acquired with open feedback (set point: I = 35 pA and V = 2.8 V) at different locations of the single molecule as indicated in a. The energetic positions of the resonances in the dI/dV spectra are highlighted by the black dash vertical lines, and all the spectra are offset for clarity. c) Constant current STM images (left panel) and corresponding dI/dV maps (right panel) of a single molecule recorded at biases of 1.0 V, 2.0 V and 2.7 V (I = 20 pA), respectively. The dI/dV signals (yellow and red colors) are superimposed over the topography (cyan). d) The DFT calculated orbital structure of the LUMO, LUMO+1 and LUMO+2.

5.3.2 The Pure Organic Assemblies

Figure 5.10 a shows dI/dV spectra recorded on an organic island. Three resonances are observed with different distribution over the molecule. The two sides possess two states at 1.3 V and 1.6 V, while the center has the state at 1.3 V and a higher-lying state at 2.3 V. The bias-dependent STM images further reveal the spatial distribution of these three resonances, as shown in figure 5.10 b. By comparing with the molecular orbital structure in gas phase (figure 5.9 d), we assign the resonances at 1.3 V, 1.6 V and 2.3 V to the LUMO, LUMO+1 and LUMO+2 of the molecule, respectively. The unoccupied orbitals are shifted down in energy compared with single molecules, similar with results in DCV5T-Me$_2$ islands. Thus, this downshift is ascribed to intermolecular interactions as well [19, 108], since the same types of bonding exist in DCV6T islands and DCV5T-Me$_2$ islands determined by AFM.

Figure 5.10: Electronic structure of DCV6T island. a) dI/dV spectra acquired with open feedback (set point: I = 70 pA and V = 3.0 V) at different locations at the molecule as indicated inset (I = 120 pA and V = 0.75 V). The energetic positions of the resonances in the dI/dV spectra are highlighted by the black dash vertical lines, and all the spectra are offset for clarity. b) Constant current STM images of an island recorded at biases of 1.3 V, 1.6 V and 2.2 V (I = 50 pA), respectively, which reveal the distribution of the unoccupied molecular orbitals.
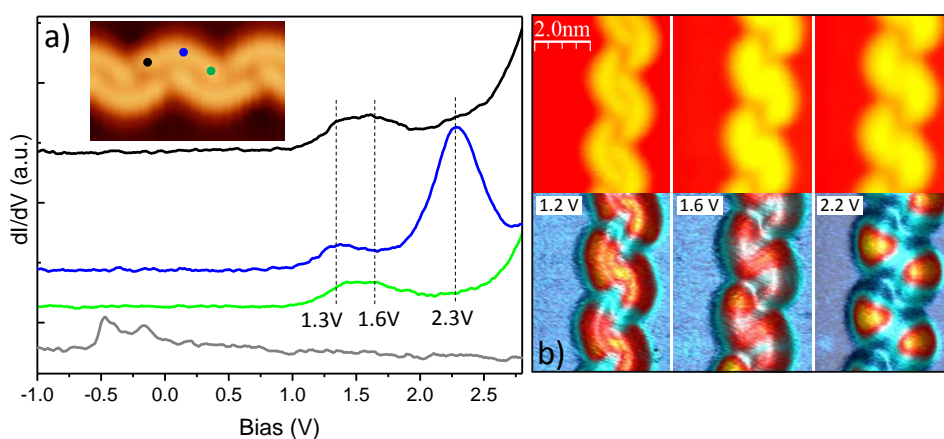
Figure 5.11: Electronic structure of the DCV6T chain. a) dI/dV spectra acquired with open feedback (set point: I = 45 pA and V = 3.0 V) at different locations of the molecule as indicated inset (I = 11 pA and V = 0.85 V). The energetic positions of the resonances in the dI/dV spectra are highlighted by the black dash vertical lines, and all the spectra are offset for clarity. b) Constant current STM images (top panel) and corresponding dI/dV maps (bottom panel) of a chain recorded at biases of 1.2 V, 1.6 V and 2.2 V (I = 15 pA), respectively. The dI/dV signals (yellow and red colors) are superimposed over the topography (cyan).

The organic chains (type B) with bent molecules exhibit the same orbital features as islands, in both spatial distribution and energetic alignment, shown in figure 5.11. It demonstrates that intermolecular interactions determine electronic properties of DCVnTs assemblies, while the molecular geometry does not play a crucial role. The corresponding devices would take advantage of the negligible effect of configuration

on molecular electronic properties. For example, although molecules adopt various configurations in films of organic solar cells, their useful characters keep the same.

5.3.3 The Au-organic Assemblies

Electronic properties of metal-organic chains (type A) with incorporation of Au adatoms are also investigated. Molecules within chains, with two sides coordinated to Au atoms, possess lower-lying unoccupied orbitals compared with single molecules, as shown in figure 5.12 a and b. This downshift in energy is induced by metal-ligand hybridization [39, 129], while the orbital spatial structure is not modified.
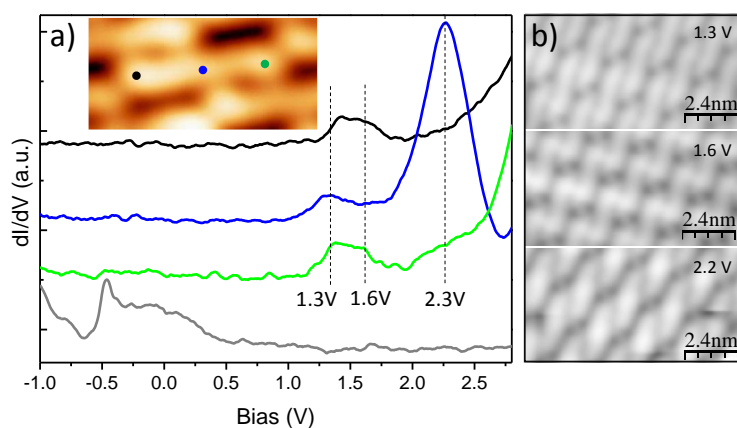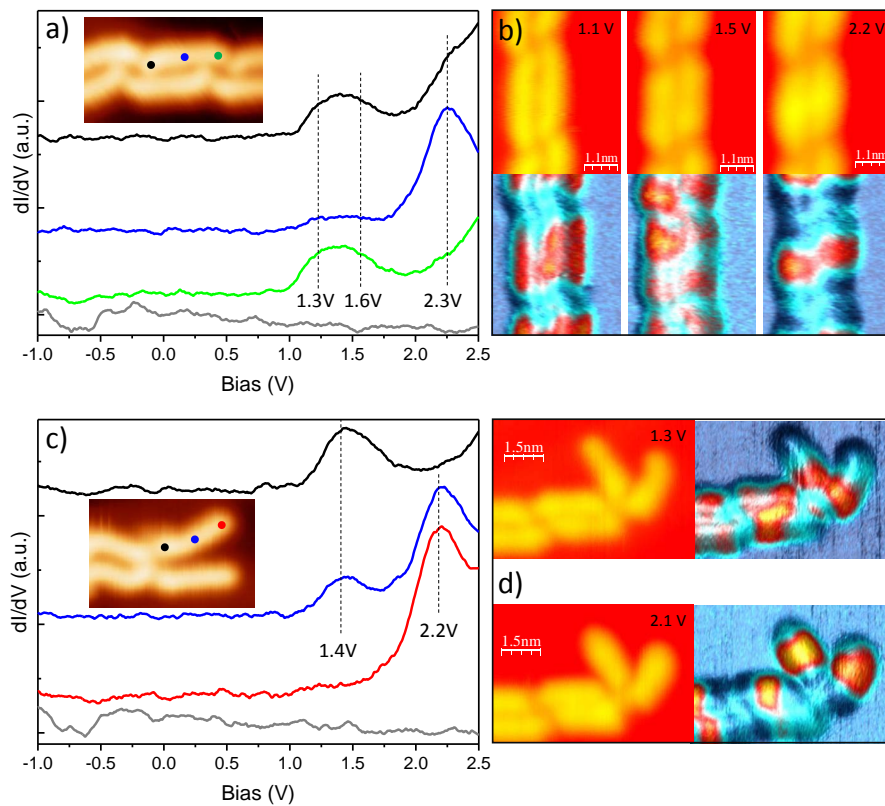

Figure 5.12: Electronic structure of the Au-DCV6T chain. a) and c) dI/dV spectra acquired with open feedback (set point: I = 120 pA and V = 2.5 V) at different locations of the two-side-coordinated molecule and the one-side-coordinated molecule as indicated inset (I = 87 pA and V = 1.13 V for a; I = 18 pA and V = 0.75 V for c), respectively. The energetic positions of the resonances in the dI/dV spectra are highlighted by the black dash vertical lines, and all the spectra are offset for clarity. b) and d) Constant current STM images (top and left panels) and corresponding dI/dV maps (bottom and right panels) of two-side-coordinated molecules and one-side-coordinated molecules recorded at indicated biases (15 pA), respectively. The dI/dV signals (yellow and red colors) are superimposed over the topography (cyan).

Orbital redistribution occurs when only one side is coordinated: the down-shifted

LUMO is localized at the coordinated side, while the down-shifted LUMO+1 is localized at the uncoordinated side, as shown in figure 5.12 c and d. It can be interpreted with the quantum chemical model: linear combination of the LUMO and LUMO+1 molecular orbitals [40]. Due to the symmetric (anti-symmetric) nodal plane of the original LUMO (LUMO+1) (figure 5.9 d), the two new orbitals are localized at opposite sides of the molecule after mixing. Here, the presence of one Au atom at only one side breaks the geometric symmetry and promotes the orbital mixing. Since both the 5T and 6T, with odd and even number of thiophene rings, exhibit the spatial orbital redistribution upon asymmetric coordination to Au atoms, this mechanism should be applicable to the whole family of DCVnTs.

5.4 Metal-organic Chains of DCV6T and Co atoms

In addition to the intrinsic adatoms on substrates, external metal atoms can be evaporated onto the surface to combine with organic ligands and form artificial nanostructures. In particular, Co atoms are widely used to coordinate with cyano functionalized molecules [135]. The corresponding metal-organic assemblies are expected to show different electronic features with respect to Au-atom-based complexes, because 3d orbitals of Co atoms are involved in the coordination instead of s states. To study the influence of different species of metal atoms on properties of the metal-organic motifs, in this section we co-deposit Co atoms and DCV6T molecules on the Au(111) surface and investigate the resulting assemblies with STM/STS.

5.4.1 Bonding Structure of the Metal-organic Chains

Figure 5.13 a shows the STM image of co-deposition of DCV6T with Co atoms at room temperature followed by post-annealing to 373 K to thermally active their mixing. Only long chains are formed on the surface. The growth direction of chains follows mostly the surface reconstruction, and the excess Co atoms aggregate into clusters at the elbows of the herringbone. The high resolution STM image in figure 5.13 b reveals that chains are located at the fcc area of the surface reconstruction. Moreover, one can identify that three cyano groups from three adjacent molecules assemble into a three-fold bonding node. It indicates that Co atoms are incorporated for bridging the electronegative cyano ligands. Although molecules do not adopt homogenous configuration due to the flexible DCV6T backbone, the three-fold coordination is ubiquitous. From the bonding model in figure 5.13 b, one can find that the two sides of one molecule are not symmetrically coordinated: one side (side A) bonds with two Co atoms, whereas the other side (side B) interacts with only one atom. This asymmetric bonding geometry is imaged by a functionalized tip (figure 5.13 c). It should induce different electronic features at the two sides of individual molecules. Note that there are no Au-DCV6T chains on the surface, since the more active Co atoms substitute for the inert Au atoms during bonding.
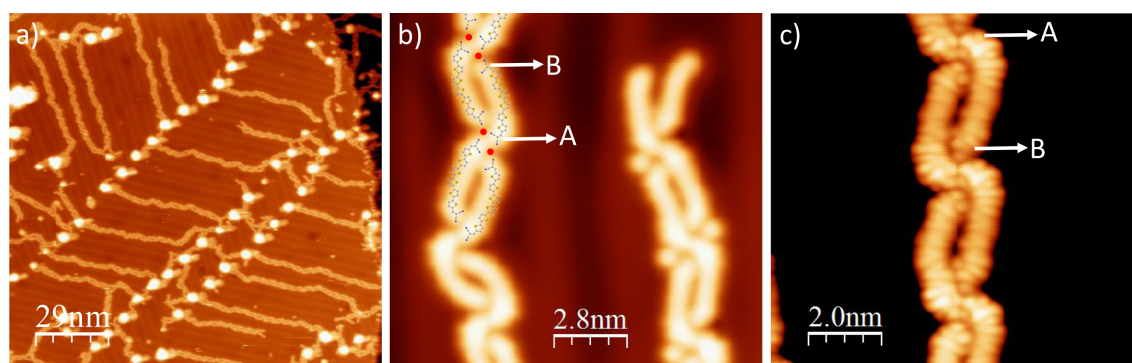
Figure 5.13: Structure of Co/DCV6T metal-organic chains on Au(111). a) STM image (I = 49 pA and V = 0.79 V) of the co-deposition of DCV6T and Co atoms at room temperature followed by annealing to 373K to activate the mixing. Long chains and Co clusters are formed mostly at the fcc region and at the elbows of the surface reconstruction, respectively. b) High resolution STM image (I = 100 pA and V = 0.75 V) of chains with bonding model superimposed. The assembly of cyano groups indicates incorporation of Co atoms (the red circles). For individual molecules, side A bonds with two Co atoms, while side B interacts with only one Co atom. c) High resolution STM image (I = 94 pA and V = 0.8 V) acquired with a functionalized tip revealing the asymmetric bonding geometry of individual molecules.

5.4.2 Electronic Properties of the Metal-organic Chains

STS is utilized to study the electronic properties of Co-DCV6T chains. Figure 5.14 a shows dI/dV spectra at a molecule within a chain. Four peaks, centered at 0.8 V, 1.1 V, 2.0 V and 2.6 V, are observed. They are located at different positions over the molecule. In particular, the two states at 2.0 V and 2.6 V are distributed at the whole molecular backbone and both sides of the molecule, respectively. This spatial distribution, which is further resolved by the dI/dV maps in figure 5.14 b, enables us to assign them to the molecular LUMO and LUMO+1 orbitals.

Spectra in figure 5.14 c exhibit higher energy resolution of the two lower-lying peaks. One can identify that the state at 0.8 V (1.1 V) is only localized at the side A (B) of the molecule (figure 5.14 d) [3]. Whereas they have the same intensity at the position of the Co atom (red dash spectrum in figure 5.14 c). This distribution indicates that these states are derived by the metal-ligand coordination. The interaction is expected to happen between the Co 3d states and lone pair orbitals at the cyano groups [135]. Moreover, the hybridization at side A relates to interactions between two cyano groups and two Co atoms, while at side B only one cyano ligand and one Co atom are involved. This different bonding geometry induces asymmetric electronic properties over individual molecules. In general, more hybridization with metal atoms results in lower energy of the states at molecules [146].

Control measurements are performed at molecules with only one side coordinated.

---

[3]The dI/dV signal is still visible at the side A at 1.1 V, which is due to the large width of the peak. However, its intensity at 1.1 V is lower at side B than at side A.

Figure 5.14: Electronic structure of the two-side-coordinated molecule in Co-DCV6T chain. a) and c) dI/dV spectra acquired with open feedback (set point: I = 120 pA and V = 2.85 V for a; I = 120 pA and V = 1.5 V for c) at different locations of the two-side-coordinated molecule as indicated inset (I = 99 pA and V = 0.72 V). The energetic positions of the resonances in the dI/dV spectra are highlighted by the black dash vertical lines. The spectra in a are offset for clarity. The red dash spectrum in c is recorded at the position of Co atom. b) and d) Constant current STM images (top panels: I = 110 pA and V = 0.79 V) and corresponding constant height dI/dV maps (central and bottom panels) of two-side-coordinated molecules recorded at indicated biases (50 pA).

The lower-lying peaks vanish at the free side with respect to the two-side coordinated molecule, while all the other features maintain, as shown in the dI/dV spectra and maps in figure 5.15. It further confirms the metal-ligand hybridization origin of the peaks at 0.8 V and 1.1 V and demonstrates the local character of the Co-CN coordination.

It is widely reported that metal-ligand hybridization induces downshift of unoccupied molecular orbitals in energy [39, 129, 135, 138, 146, 188]. Surprisingly, here the energetic alignment of the LUMO and LUMO+1 is not modified by the Co-CN coordination, in opposite to results in Au-DCV6T chains. The difference should be attributed to the different atomic structure of Co atom and Au atom, for which 6s state and 3d state contribute to the coordination, respectively. Theoretical calculations should be carried out to gain more insight into the physics behind. Nevertheless,
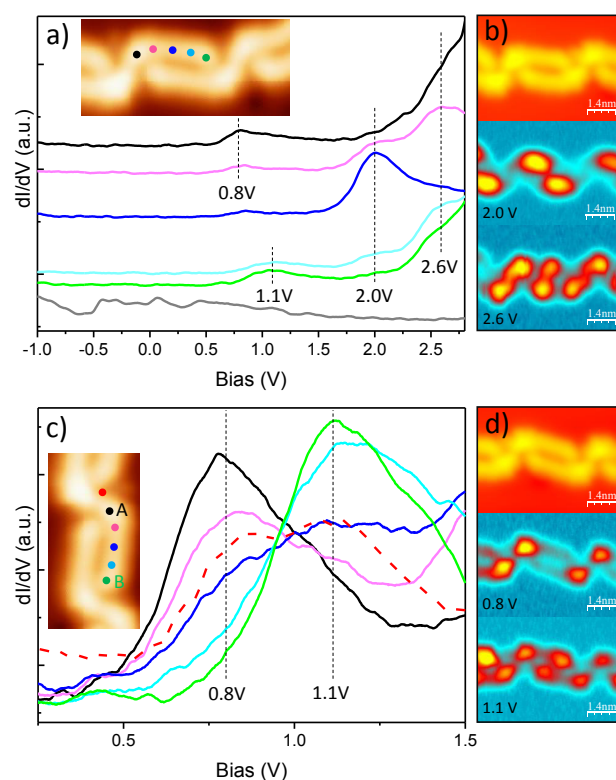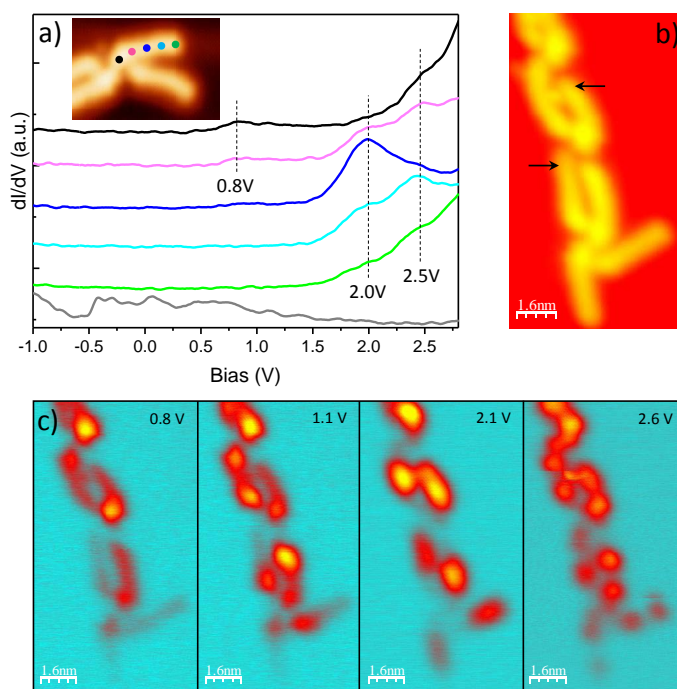
Figure 5.15: Electronic structure of the one-side-coordinated molecule in Co-DCV6T chain. a) dI/dV spectra acquired with open feedback (set point: I = 120 pA and V = 2.85 V) at different locations of the one-side-coordinated molecule as indicated inset (I = 99 pA and V = 0.72 V). The energetic positions of the resonances in the dI/dV spectra are highlighted by the black dash vertical lines. All the spectra are offset for clarity. b) Constant current STM (I = 80 pA and V = 0.8 V) of a chain with one-side-coordinated molecules at the end. The black arrows highlight two molecules with the coordination dissociated at one side. c) Corresponding constant height dI/dV maps recorded at indicated biases.

the organic electronics based on DCVnTs will benefit from this behavior. Molecules can be connected through Co atoms to build organic circuits [36] on surfaces, while the conduction bands of the organic semiconductor for charge transport are not perturbed. Recently, the same phenomenon was reported on graphene nanoribbons [189]. A chemical bond is created between the nanoribbon and a Au atom without modification to its bulk electronic structure. Here, we observe an analogue in functional organic molecules.

5.5 Conclusions

In this chapter both the lock-and-key effect and the induced fit effect in molecular recognition of DCV6T are resolved and understood with atomic resolution by using combined STM/AFM imaging and DFT calculations. DCV6T molecules self-assemble in large organic islands and long organic chains through hydrogen bonding and electrostatic interactions on Au(111). The formation of islands is the result of

lock-and-key effect in the static molecular recognition, while the formation of chains is regulated by the induced fit effect *via* the dynamic molecular recognition. DCV6T in chains undergoes two steps of deformation with respect to molecules in islands. The rotation of one thiophene ring results in bent configuration of the molecules, which is slightly off the optimal bonding geometry. Thus, the specificity of the hydrogen-bonds induces further bending of around 13° more of the molecules. Although individual molecules are not in the energy minimum configuration, the whole chain structure relaxes to a more stable state in energy. These results demonstrate that one type of molecules can undergo complex deformation processes and form completely different nanostructures on the surface, which can be imaged and quantified accurately with combined STM/AFM measurements and DFT calculations.

Electronic properties of various assemblies of DCV6T on Au(111) are studied with STS. Molecules exhibit the same energetically down-shifted unoccupied orbitals in organic islands and chains with different configurations. It demonstrates that intermolecular interactions rather than the molecular geometry determine the electronic properties of DCV6T assemblies. The electronics composed of molecular films take advantage of this mechanism, where molecules adopt different configurations. In Au-DCV6T chains, spatial redistribution of the LUMO and LUMO+1 occurs at the one-side coordinated molecule due to breaking of symmetry, the same mechanism as that in Au-DCV5T-Me$_2$ complex.

Three-fold metal-organic chains are formed by co-deposition of Co atoms and DCV6T on Au(111). The fingerprint of coordination bonding is two lower-layer peaks located at the end-DCV groups. Differently from the widely reported results in metal-organic complexes, in Co-DCV6T chains both the spatial distribution and energetic alignment of the unoccupied molecular orbitals are not influence by the Co-CN hybridization. The intactness of conduction bands after contacting with a metallic lead sheds new light on the fabrication of organic circuits on surfaces.

6 Summary

In this thesis, we investigated supramolecular architectures based on dicyanovinylene-substituted oligothiophenes, DCV5T-Me$_2$ and DCV6T, on metal surfaces. A microscopic understanding of their structural and electronic properties at the organic/organic and organic/metal interfaces, is obtained by utilizing low temperature STM and AFM.

Upon adsorption on Au(111), DCV5T-Me$_2$ lays on the surface in a planar geometry corresponding to the DFT calculated global minimum configuration in gas phase. The majority of molecules self-assembly into extended organic islands. Intermolecular electrostatic interaction (S-CN) and hydrogen bonding stabilize the two-dimensional domains. In particular, the electrostatic interaction enhances the thermal stability of the organic assembly on the surface. These strong intermolecular interactions energetically shift down the unoccupied molecular states in islands with respect to the isolated molecule on the surface. The resulting energy level shift is of great importance for designing organic electronics based on these molecules.

A double layer film is formed with the increase of coverage. Molecules in the second layer pack in a similar way with that in the molecular islands on the Au(111) surface. Differential conductance spectra exhibit sharper and higher-lying resonances in the second layer than in the first layer due to a decoupling from the metal. This allowed for the observation of a vibrational state coupled with both the LUMO and LUMO+1, with energy around 0.18 eV. The mode corresponds to the stretching of C=C and C-C bonds over the whole molecular backbone. This vibration mode plays a crucial role in the charge transfer in blends of oligothiophenes and C$_{60}$ [110].

Metal-organic chains are formed on Au(111), simultaneously with the organic islands, through incorporation of Au adatoms by cyano groups. The metal center and bonding geometry are imaged with AFM. The fingerprint of metal-ligand hybridization is an energetic downshift of the LUMO orbital compared with the single, isolated molecule. Interestingly, the LUMO and LUMO+1 are spatially redistributed over the molecule, when only one side is coordinated to a Au atom. Supported by DFT calculations, we interpreted this renormalization with the linear combination of molecular orbitals. The asymmetric attachment of a Au atom triggers the mixing of the original LUMO and LUMO+1 orbitals, hence, adapt the new orbital structure to the bonding geometry. Moreover, the different electronic properties of molecules with zero, one and two coordination bonds depicts a tuning strategy to manipulate the orbital character of molecular films by site-specific doping with metal atoms.

It has been reported that bridging two molecules with a metal atom can induce an overlap of orbitals from each molecule [40], while attachment of metal atoms to one molecule usually only leads to a downshift of unoccupied orbitals in energy [39]. Here we demonstrate that two different orbitals close in energy within an individual molecule also can mix by a linear combination triggered by an asymmetric coordination to a metal atom. Our results complement the physical picture of the metal-organic contact.

Co-deposition of NaCl and DCV5T-Me$_2$ on Au(111) results in the formation of metal-organic chains stabilized by Na-CN bonding. These chains keep the maximum separation consistent with the coverage. The statistics on the inter-chain distance distribution reveals an inter-chain repulsive force generating an electrostatic potential well, which induces the formation of the one-dimensional super-lattice. It is demonstrated that the charged methyl groups within individual molecules serve as positively charged points and are responsible for the inter-chain Coulomb repulsion. These results indicate that the long-range interaction on surfaces not only can influence the adsorption of individual adsorbates, but also could mediate the growth of self-assembled nanostructures, as for example gratings composed of metal-organic chains.

One drawback of the coordination with Au atoms and strong interactions between DCV5T-Me$_2$ molecules themselves is that the formation of ordered hybrid molecular structures on Au(111) is inhibited. The induced orbital energy realignment suppresses the electron donor character of DCVnTs when mixing with acceptor molecules.

DCV5T-Me$_2$ exhibits different features on Ag(111) and Cu(111) with respect to on Au(111) due to the difference of surface work function and reactivity. Organic islands are assembled on Ag(111) with similar structural and electronic properties as those on Au(111). The only difference is a rigid downshift of orbital energies by the lower work function of Ag(111) than Au(111). However, no metal-organic motifs are formed on Ag(111) because of the inertness of Ag atoms when interacting with ligands. DCV5T-Me$_2$ chemically adsorbs on Cu(111) and forms metal-organic chains with the combination of Cu adatoms at a temperature of 230 K. The strong hybridization with the surface eliminates the molecular states and, accordingly, enables scattering and confinement of surface electrons by the molecular structures. Surprisingly, at room temperature DCV5T-Me$_2$ molecules are dissociated, which should draw attention when designing organic devices with Cu leads.

DCV6T self-assembles into metal-organic chains with Au adatoms, organic islands and purely organic chains on Au(111), adopting different configurations due to its flexibility. AFM imaging reveals that molecules in islands have the energetic minimum geometry and self-recognize through the lock-and-key effect. DCV6T within organic chains undergoes two steps of deformation with respect to that in islands. The rotation of one thiophene ring results in a metastable bent configuration, which

is slightly off the optimal bonding geometry. Thus, the specificity of the intermolecular hydrogen-bonds induces further bending of around $13°$ more to the molecules. Although the individual molecules are not in the energy minimum configuration, the whole chain structure relaxes to a more stable state in energy, as confirmed with DFT calculations. This induced fit effect regulates the formation of organic chains. These results demonstrate that one type of molecules can undergo complex deformation processes and form completely different nanostructures on the surface, which can be imaged and quantified accurately with combined STM/AFM measurements and DFT calculations.

DCV6T exhibits the same energetically down-shifted unoccupied orbitals in organic islands and organic chains with different configurations. It means that intermolecular interactions rather than the molecular geometry determine electronic properties of DCV6T assemblies. The electronics composed of molecular films take advantage of this mechanism, where molecules adopt different configurations.

In Au-DCV6T chains, site-specific modification to molecular orbitals occurs, the same as in the Au-DCV5T-Me$_2$ chains. This behavior should exist in the whole DCVnTs family, due to their symmetric LUMO and anti-symmetric LUMO+1 viewed from point of the sign of electron wave functions.

Homogenous three-fold metal-organic chains are formed by co-deposition of Co atoms and DCV6T on Au(111). The fingerprint of coordination bonding is two lower-lying peaks in the positive polarity, localized at the end-DCV groups. Differently from the results in metal-organic complexes with Au atoms, in Co-DCV6T chains both the spatial distribution and energetic alignment of the unoccupied molecular orbitals are not influenced by the Co-CN hybridization. The intactness of conduction bands after contacting with a metallic lead sheds new light on the fabrication of organic circuits on surfaces.

The combined STM and AFM study on organic molecules, specially designed for organic solar cell, provides a good insight into their structural and electronic properties at the organic/organic and organic/metal interfaces with atomic resolution. This knowledge should help in improving the functionality of corresponding organic electronics.

As an outlook, the STM study can go closer to the real organic solar cell devices. The interaction between DCVnTs and C$_{60}$ may be enhanced by co-depositing them on an insulating layer. Moreover, growing DCVnTs on top of a C$_{60}$ layer should maintain their desirable orbital energy alignment, therefore, electrons can transfer from DCVnTs to the fullerenes. Furthermore, a study on electroluminescence of oligothiophenes suspended between the STM tip and the metal surface has been reported recently [190]. It should be of great interest to investigate the modification of DCV groups to the electroluminescence properties of DCVnTs in the same way.

Abbreviations

DCV5T-Me$_2$: dicyanovinyl-quinquethiophenes

DCV6T: dicyanovinyl-hexathiophenes

(LT-)STM: (low temperature) scanning tunneling microscopy

(nc-)AFM: (no-contact) atomic force microscopy

LUMO: lowest unoccupied molecular orbital

LCMO: linear combination of molecule orbitals

STS: scanning tunneling spectroscopy

vdW: van der Waals

CPD: contact potential difference

UHV: ultra high vacuum

PLL: phase locked loop

DFT: density functional theory

fcc: face centered cubic

LDOS: local density of states

TCNQ: tetracyanoquinodimethane

8T: octithiophene

FWHM: full width half maximum

SOMO: single occupied molecular orbital

HOMO: highest occupied molecular orbital

PDOS: projected density of states

A-D-A: acceptor-donor-acceptor

ML: monolayer

SCF: self-consistent field

Bibliography

[1] Takashi Ito and Shinji Okazaki. Pushing the limits of lithography. *Nature*, 406:1027–1031, 2000.

[2] Richard P. Feynman. There's plenty of room at the bottom. *Caltech Engineering and Science*, 23:5:22–36, 1960.

[3] Johannes V. Barth. Molecular architectonic on metal surfaces. *Annual Review of Physical Chemistry*, 58(1):375–407, 2007.

[4] C. Rogero, J. I. Pascual, J. Gómez-Herrero, and A. M. Baró. Resolution of site-specific bonding properties of C_{60} adsorbed on Au(111). *The Journal of Chemical Physics*, 116(2):832–836, 2002.

[5] James A. Theobald, Neil S. Oxtoby, Michael A. Phillips, Neil R. Champness, and Peter H. Beton. Controlling molecular deposition and layer structure with supramolecular surface assemblies. *Nature*, 424:1029–1031, 2003.

[6] Leonhard Grill, Matthew Dyer, Leif Lafferentz, Mats Persson, Maike V. Peters, and Stefan Hecht. Nano-architectures by covalent assembly of molecular building blocks. *Nat. Nano.*, 2:687–691, 2007.

[7] Nikolas A. A. Zwaneveld, Rémy Pawlak, Mathieu Abel, Daniel Catalin, Didier Gigmes, Denis Bertin, and Louis Porte. Organized formation of 2D extended covalent organic frameworks at surfaces. *Journal of the American Chemical Society*, 130(21):6678–6679, 2008.

[8] U. Schlickum, R. Decker, F. Klappenberger, G. Zoppellaro, S. Klyatskaya, M. Ruben, I. Silanes, A. Arnau, K. Kern, H. Brune, and J. V. Barth. Metal-organic honeycomb nanomeshes with tunable cavity size. *Nano Letters*, 7(12):3813–3817, 2007.

[9] Pietro Gambardella, Sebastian Stepanow, Alexandre Dmitriev, Jan Honolka, Frank M. F. de Groot, Magalí Lingenfelder, Subhra Sen Gupta, D. D. Sarma, Peter Bencok, Stefan Stanescu, Sylvain Clair, Stéphane Pons, Nian Lin, Ari P. Seitsonen, Harald Brune, Johannes V. Barth, and Klaus Kern. Supramolecular control of the magnetic anisotropy in two-dimensional high-spin fe arrays at a metal interface. *Nat. Mater.*, 8:189–193, 2009.

[10] D. E. Koshland. Application of a theory of enzyme specificity to protein synthesis. *Proceedings of the National Academy of Sciences*, 44(2):98–104, 1958.

[11] Daniel E. Koshland. The key-lock theory and the induced fit theory. *Angewandte Chemie International Edition*, 33:2375–2378, 1995.

[12] Yonatan Savir and Tsvi Tlusty. Conformational proofreading: The impact of conformational changes on the specificity of molecular recognition. *PLoS ONE*, 2(5):e468, 2007.

[13] Takashi Yokoyama, Shiyoshi Yokoyama, Toshiya Kamikado, Yoshishige Okuno, and Shinro Mashiko. Selective assembly on a surface of supramolecular aggregates with controlled size and shape. *Nature*, 413:619–621, 2001.

[14] Chi-lun Chiang, Chen Xu, Zhumin Han, and W. Ho. Real-space imaging of molecular structure and chemical bonding by single-molecule inelastic tunneling probe. *Science*, 344(6186):885–888, 2014.

[15] Franz J. Giessibl. Advances in atomic force microscopy. *Rev. Mod. Phys.*, 75:949–983, 2003.

[16] Leo Gross, Fabian Mohn, Nikolaj Moll, Peter Liljeroth, and Gerhard Meyer. The chemical structure of a molecule resolved by atomic force microscopy. *Science*, 325(5944):1110–1114, 2009.

[17] Jun Zhang, Pengcheng Chen, Bingkai Yuan, Wei Ji, Zhihai Cheng, and Xiaohui Qiu. Real-space identification of intermolecular bonding with atomic force microscopy. *Science*, 342(6158):611–614, 2013.

[18] F. Jäckel, U. G. E. Perera, V. Iancu, K.-F. Braun, N. Koch, J. P. Rabe, and S.-W. Hla. Investigating molecular charge transfer complexes with a low temperature scanning tunneling microscope. *Phys. Rev. Lett.*, 100:126102, 2008.

[19] J. Kröger, H. Jensen, R. Berndt, R. Rurali, and N. Lorente. Molecular orbital shift of perylenetetracarboxylic-dianhydride on gold. *Chemical Physics Letters*, 438(46):249–253, 2007.

[20] Xinghua Lu, M. Grobis, K. H. Khoo, Steven G. Louie, and M. F. Crommie. Spatially mapping the spectral density of a single C_{60} molecule. *Phys. Rev. Lett.*, 90:096802, 2003.

[21] Xinghua Lu, M. Grobis, K. H. Khoo, Steven G. Louie, and M. F. Crommie. Charge transfer and screening in individual C_{60} molecules on metal substrates: A scanning tunneling spectroscopy and theoretical study. *Phys. Rev. B*, 70:115418, 2004.

[22] I. Fernandez-Torrente, S. Monturet, K. J. Franke, J. Fraxedas, N. Lorente, and J. I. Pascual. Long-range repulsive interaction between molecules on a metal surface induced by charge transfer. *Phys. Rev. Lett.*, 99:176103, 2007.

[23] N. Henningsen, R. Rurali, K.J. Franke, I. Fernández-Torrente, and J.I. Pascual. Trans to cis isomerization of an azobenzene derivative on aCu(100) surface. *Appl. Phys. A*, 93(2):241–246, 2008.

[24] Daniel Wegner, Ryan Yamachika, Yayu Wang, Victor W. Brar, Bart M. Bartlett, Jeffrey R. Long, and Michael F. Crommie. Single-molecule charge transfer and bonding at an organic/inorganic interface: Tetracyanoethylene on noble metals. *Nano Letters*, 8(1):131–135, 2008.

[25] Hasmik Harutyunyan, Martin Callsen, Tobias Allmers, Vasile Caciuc, Stefan Blugel, Nicolae Atodiresei, and Daniel Wegner. Hybridisation at the organic-metal interface: a surface-scientific analogue of Hückel's rule? *Chem. Commun.*, 49:5993–5995, 2013.

[26] G. Heimel, S. Duhm, I. Salzmann, A. Gerlach, A. Strozecka, J. Niederhausen, C. Bürker, T. Hosokai, I. Fernandez-Torrente, G. Schulze, S. Winkler, A. Wilke, R. Schlesinger, J. Frisch, B. Bröker, A. Vollmer, B. Detlefs, J. Pflaum, S. Kera, K. J. Franke, N. Ueno, J. I. Pascual, F. Schreiber, and N. Koch. Charged and metallic molecular monolayers through surface-induced aromatic stabilisation. *Nat. Chem.*, 5:187–194, 2013.

[27] X. H. Qiu, G. V. Nazin, and W. Ho. Vibronic states in single molecule electron transport. *Phys. Rev. Lett.*, 92:206102, 2004.

[28] Isabel Fernández Torrente, Katharina J. Franke, and Jose Ignacio Pascual. Structure and electronic configuration of tetracyanoquinodimethane layers on a Au(111) surface. *International Journal of Mass Spectrometry*, 277(13):269–273, 2008.

[29] Erwan Varene, Yan Pennec, and Petra Tegeder. Assembly and electronic structure of octithiophene on Au(111). *Chemical Physics Letters*, 515(13):141–145, 2011.

[30] Hisao Ishii, Kiyoshi Sugiyama, Eisuke Ito, and Kazuhiko Seki. Energy level alignment and interfacial electronic structures at organic/metal and organic/organic interfaces. *Adv. Mater.*, 11(8):605–625, 1999.

[31] D. Cahen and A. Kahn. Electron energetics at surfaces and interfaces: Concepts and experiments. *Adv. Mater.*, 15(4):271–277, 2003.

[32] G. Binnig, H. Rohrer, Ch. Gerber, and E. Weibel. Surface studies by scanning tunneling microscopy. *Phys. Rev. Lett.*, 49:57–61, 1982.

[33] I. Díez-Pérez, J. Hihath, Y. Lee, L. Yu, L. Adamska, M. A. Kozhushner, I. I. Oleynik, and N. Tao. Rectification and stability of a single molecular diode with controlled orientation. *Nature Chemistry*, 1:635 – 641, 2009.

[34] H. Song, Y. Kim, Y. H. Jang, H. Jeong, M. A. Reed, and T. Lee. Observation of molecular orbital gating. *Nature*, 462:1039–1043, 2009.

[35] Peter Liljeroth, Jascha Repp, and Gerhard Meyer. Current-induced hydrogen tautomerization and conductance switching of naphthalocyanine molecules. *Science*, 317(5842):1203–1206, 2007.

[36] Mark A. Reed and Takhee Lee, editors. *Molecular Nanoelectronics*. Department of Electrical Engineering, Yale University, USA, 2003.

[37] Katharina J. Franke and Jose I. Pascual. Effects of electron-vibration coupling in transport through single molecules. *Journal of Physics: Condensed Matter*, 24(39):394002, 2012.

[38] Jascha Repp, Gerhard Meyer, Sladjana M. Stojković, André Gourdon, and Christian Joachim. Molecules on insulating films: Scanning-tunneling microscopy imaging of individual molecular orbitals. *Phys. Rev. Lett.*, 94:026803, Jan 2005.

[39] Weihua Wang, Xingqiang Shi, Chensheng Lin, Rui Qin Zhang, Christian Minot, Michel A. Van Hove, Yuning Hong, Ben Zhong Tang, and Nian Lin. Manipulating localized molecular orbitals by single-atom contacts. *Phys. Rev. Lett.*, 105:126801, 2010.

[40] Florian Albrecht, Mathias Neu, Christina Quest, Ingmar Swart, and Jascha Repp. Formation and characterization of a molecule-metal-molecule bridge in real space. *Journal of the American Chemical Society*, 135(24):9200–9203, 2013.

[41] JOSEPH A. STROSCIO and D. M. EIGLER. Atomic and molecular manipulation with the scanning tunneling microscope. *Science*, 254(5036):1319–1326, 1991.

[42] Frédéric Demanze, Jérome Cornil, Francis Garnier, Gilles Horowitz, Pierre Valat, Abderrahim Yassar, Roberto Lazzaroni, and Jean-Luc Brédas. Tuning of the electronic and optical properties of oligothiophenes via cyano substitution: A joint experimental and theoretical study. *The Journal of Physical Chemistry B*, 101(23):4553–4558, 1997.

[43] Juan Casado, Ted M. Pappenfus, Kent R. Mann, Enrique Ortí, Pedro M. Viruela, Begona Milián, Víctor Hernández, and Juan T. López Navarrete. Spectroscopic and theoretical study of the molecular and electronic structures of a terthiophene-based quinodimethane. *ChemPhysChem*, 5(4):529–539, 2004.

[44] K. Schulze, C. Uhrich, R. Schüppel, K. Leo, M. Pfeiffer, E. Brier, E. Reinold, and P. Bäuerle. Efficient vacuum-deposited organic solar cells based on a new low-bandgap oligothiophene and fullerene C_{60}. *Advanced Materials*, 18(21):2872–2875, 2006.

[45] R. Schueppel, K. Schmidt, C. Uhrich, K. Schulze, D. Wynands, J. L. Brédas, E. Brier, E. Reinold, H.-B. Bu, P. Baeuerle, B. Maennig, M. Pfeiffer, and K. Leo. Optimizing organic photovoltaics using tailored heterojunctions: A photoinduced absorption study of oligothiophenes with low band gaps. *Phys. Rev. B*, 77:085311, Feb 2008.

[46] D. Wynands, M. Levichkova, M. Riede, M. Pfeiffer, P. Baeuerle, R. Rentenberger, P. Denner, and K. Leo. Correlation between morphology and performance of low bandgap oligothiophene: C_{60} mixed heterojunctions in organic solar cells. *Journal of Applied Physics*, 107(1):014517–014517–6, Jan 2010.

[47] Amaresh Mishra, Christian Uhrich, Egon Reinold, Martin Pfeiffer, and Peter Bäuerle. Synthesis and characterization of acceptor-substituted oligothiophenes for solar cell applications. *Advanced Energy Materials*, 1(2):265–273, 2011.

[48] Roland Fitzner, Egon Reinold, Amaresh Mishra, Elena Mena-Osteritz, Hannah Ziehlke, Christian Körner, Karl Leo, Moritz Riede, Matthias Weil, Olga Tsaryova, André Weiß, Christian Uhrich, Martin Pfeiffer, and Peter Bäuerle. Dicyanovinylsubstituted oligothiophenes: Structure-property relationships and application in vacuum-processed small molecule organic solar cells. *Advanced Functional Materials*, 21(5):897–910, 2011.

[49] Stefan Haid, Amaresh Mishra, Christian Uhrich, Martin Pfeiffer, and Peter Bäuerle. Dicyanovinylene-substituted selenophenethiophene co-oligomers for small-molecule organic solar cells. *Chemistry of Materials*, 23(20):4435–4444, 2011.

[50] Manuel Schrader, Roland Fitzner, Moritz Hein, Chris Elschner, Björn Baumeier, Karl Leo, Moritz Riede, Peter Bäuerle, and Denis Andrienko. Comparative study of microscopic charge dynamics in crystalline acceptor-substituted oligothiophenes. *J. Am. Chem. Soc.*, 134(13):6052–6056, 2012.

[51] G. Binnig, H. Rohrer, Ch. Gerber, and E. Weibel. Tunneling through a controllable vacuum gap. *Applied Physics Letters*, 40(2):178–180, 1982.

[52] G. Binnig, H. Rohrer, Ch. Gerber, and E. Weibel. 7×7 reconstruction on Si(111) resolved in real space. *Phys. Rev. Lett.*, 50:120–123, 1983.

[53] J. Bardeen. Tunnelling from a many-particle point of view. *Phys. Rev. Lett.*, 6:57–59, 1961.

[54] J. Klein, A. Léger, M. Belin, D. Défourneau, and M. J. L. Sangster. Inelastic-electron-tunneling spectroscopy of metal-insulator-metal junctions. *Phys. Rev. B*, 7:2336–2348, 1973.

[55] http://en.wikipedia.org/wiki/scanning_tunneling_microscope.

[56] Isabel Fernández Torrente. Doctoral thesis at FU Berlin. 2008.

[57] J. Tersoff and D. R. Hamann. Theory and application for the scanning tunneling microscope. *Phys. Rev. Lett.*, 50:1998–2001, 1983.

[58] J. Tersoff and D. R. Hamann. Theory of the scanning tunneling microscope. *Phys. Rev. B*, 31:805–813, 1985.

[59] A. Selloni, P. Carnevali, E. Tosatti, and C. D. Chen. Voltage-dependent scanning-tunneling microscopy of a crystal surface: Graphite. *Phys. Rev. B*, 31:2602–2605, 1985.

[60] N. D. Lang. Spectroscopy of single atoms in the scanning tunneling microscope. *Phys. Rev. B*, 34:5947–5950, 1986.

[61] Lucia Vitali, Giacomo Levita, Robin Ohmann, Alessio Comisso, Alessandro De Vita, and Klaus Kern. Portrait of the potential barrier at metal-organic nanocontacts. *Nat. Mater.*, 9:320–323, 2010.

[62] Joseph A. Stroscio, R. M. Feenstra, and A. P. Fein. Electronic structure of the Si(111)2 × 1 surface by scanning-tunneling microscopy. *Phys. Rev. Lett.*, 57:2579–2582, 1986.

[63] C. Wagner, R. Franke, and T. Fritz. Evaluation of I(V) curves in scanning tunneling spectroscopy of organic nanolayers. *Phys. Rev. B*, 75:235432, 2007.

[64] M. Ziegler, N. Néel, A. Sperl, J. Kröger, and R. Berndt. Local density of states from constant-current tunneling spectra. *Phys. Rev. B*, 80:125402, 2009.

[65] G. Binnig, C. F. Quate, and Ch. Gerber. Atomic force microscope. *Phys. Rev. Lett.*, 56:930–933, 1986.

[66] Franz J. Giessibl. Atomic resolution of the silicon (111)-(7×7) surface by atomic force microscopy. *Science*, 267:68–71, 1995.

[67] Y. Martin, C. C. Williams, and H. K. Wickramasinghe. Atomic force microscope-force mapping and profiling on a sub 100-å scale. *Journal of Applied Physics*, 61:4723–4729, 1987.

[68] T. R. Albrecht, P. Grtter, D. Horne, and D. Rugar. Frequency modulation detection using high-Q cantilevers for enhanced force microscope sensitivity. *Journal of Applied Physics*, 69:668–673, 1991.

[69] Christian Lotze. Doctoral thesis at FU Berlin. 2013.

[70] Franz J. Giessibl. Forces and frequency shifts in atomic-resolution dynamic-force microscopy. *Phys. Rev. B*, 56:16010–16015, 1997.

[71] John E. Sader and Suzanne P. Jarvis. Accurate formulas for interaction force and energy in frequency modulation force spectroscopy. *Applied Physics Letters*, 84(10):1801–1803, 2004.

[72] J. E. Jones. On the determination of molecular fields. II. from the equation of state of a gas. *Proceedings of the Royal Society of London. Series A*, 106(738):463–477, 1924.

[73] H.C. Hamaker. The london-van der Waals attraction between spherical particles. *Physica*, 4(10):1058 – 1072, 1937.

[74] Lord Kelvin. V. contact electricity of metals. *Philosophical Magazine Series 5*, 46(278):82–120, 1898.

[75] Wilhelm Melitz, Jian Shen, Andrew C. Kummel, and Sangyeob Lee. Kelvin probe force microscopy and its application. *Surface Science Reports*, 66(1):1–27, 2011.

[76] M. Nonnenmacher, M. P. OBoyle, and H. K. Wickramasinghe. Kelvin probe force microscopy. *Applied Physics Letters*, 58(25):2921–2923, 1991.

[77] Ch. Sommerhalter, Th. W. Matthes, Th. Glatzel, A. Jäger-Waldau, and M. Ch. Lux-Steiner. High-sensitivity quantitative kelvin probe microscopy by noncontact ultra-high-vacuum atomic force microscopy. *Applied Physics Letters*, 75:286–288, 1999.

[78] Clemens Barth and Claude R. Henry. Surface double layer on (001) surfaces of alkali halide crystals: A scanning force microscopy study. *Phys. Rev. Lett.*, 98:136804, 2007.

[79] Leo Gross, Fabian Mohn, Peter Liljeroth, Jascha Repp, Franz J. Giessibl, and Gerhard Meyer. Measuring the charge state of an adatom with noncontact atomic force microscopy. *Science*, 324(5933):1428–1431, 2009.

[80] Fabian Mohn, Leo Gross, Nikolaj Moll, and Gerhard Meyer. Imaging the charge distribution within a single molecule. *Nat. Nano.*, 7:227231, 2012.

[81] Leo Gross, Nikolaj Moll, Fabian Mohn, Alessandro Curioni, Gerhard Meyer, Felix Hanke, and Mats Persson. High-resolution molecular orbital imaging using a p-wave STM tip. *Phys. Rev. Lett.*, 107:086101, Aug 2011.

[82] Christian Weiss, Christian Wagner, Ruslan Temirov, and F. Stefan Tautz. Direct imaging of intermolecular bonds in scanning tunneling microscopy. *Journal of the American Chemical Society*, 132(34):11864–11865, 2010.

[83] Leo Gross, Fabian Mohn, Nikolaj Moll, Gerhard Meyer, Rainer Ebel, Wael M. Abdel-Mageed, and Marcel Jaspars. Organic structure determination using atomic-resolution scanning probe microscopy. *Nat. Chem.*, 2:821–825, 2010.

[84] Leo Gross, Fabian Mohn, Nikolaj Moll, Bruno Schuler, Alejandro Criado, Enrique Guitián, Diego Pena, André Gourdon, and Gerhard Meyer. Bond-order discrimination by atomic force microscopy. *Science*, 337(6100):1326–1329, 2012.

[85] Bruno Schuler, Wei Liu, Alexandre Tkatchenko, Nikolaj Moll, Gerhard Meyer, Anish Mistry, David Fox, and Leo Gross. Adsorption geometry determination of single molecules by atomic force microscopy. *Phys. Rev. Lett.*, 111:106103, Sep 2013.

[86] Dimas G. de Oteyza, Patrick Gorman, Yen-Chia Chen, Sebastian Wickenburg, Alexander Riss, Duncan J. Mowbray, Grisha Etkin, Zahra Pedramrazi, Hsin-Zon Tsai, Angel Rubio, Michael F. Crommie, and Felix R. Fischer. Direct imaging of covalent bond structure in single-molecule chemical reactions. *Science*, 340(6139):1434–1437, 2013.

[87] Niko Pavliček, Benoit Fleury, Mathias Neu, Judith Niedenführ, Coral Herranz-Lancho, Mario Ruben, and Jascha Repp. Atomic force microscopy reveals bistable configurations of dibenzo[a,h]thianthrene and their interconversion pathway. *Phys. Rev. Lett.*, 108:086101, Feb 2012.

[88] Niko Pavliček, Coral Herranz-Lancho, Benoit Fleury, Mathias Neu, Judith Niedenführ, Mario Ruben, and Jascha Repp. High-resolution scanning tunneling and atomic force microscopy of stereochemically resolved dibenzo[a,h]thianthrene molecules. *physica status solidi (b)*, 250(11):2424–2430, 2013.

[89] Prokop Hapala, Georgy Kichin, Christian Wagner, F. Stefan Tautz, Ruslan Temirov, and Pavel Jelínek. Mechanism of high-resolution STM/AFM imaging with functionalized tips. *Phys. Rev. B*, 90:085421, 2014.

[90] A.M. Sweetman, S.P. Jarvis, Hongqian Sang, I. Lekkas, P. Rahe, Yu Wang, Jianbo Wang, N.R. Champness, L. Kantorovich, and P. Moriarty. Mapping the force field of a hydrogen-bonded assembly. *Nat. Commun.*, 5, 2014.

[91] Gerhard Meyer. A simple low-temperature ultrahigh-vacuum scanning tunneling microscope capable of atomic manipulation. *Review of Scientific Instruments*, 67(8):2960–2965, 1996.

[92] K. Besocke. An easily operable scanning tunneling microscope. *Surface Science*, 181(12):145–153, 1987.

[93] J. Frohn, J. F. Wolf, K. Besocke, and M. Teske. Coarse tip distance adjustment and positioner for a scanning tunneling microscope. *Review of Scientific Instruments*, 60(6):1200–1201, 1989.

[94] I. Horcas, R. Fernández, J. M. Gómez-Rodríguez, J. Colchero, J. Gómez-Herrero, and A. M. Baro. WSXM: A software for scanning probe microscopy and a tool for nanotechnology. *Review of Scientific Instruments*, 78:013705, 2007.

[95] Michael Ruby. http://spectrafox.com/.

[96] M. J. Frisch et al. Gaussian 09 Revision D.01. *Gaussian Inc. Wallingford CT 2009*.

[97] Robin Ohmann, Giacomo Levita, Lucia Vitali, Alessandro De Vita, and Klaus Kern. Influence of subsurface layers on the adsorption of large organic molecules on close-packed metal surfaces. *ACS Nano*, 5(2):1360–1365, 2011.

[98] J. V. Barth, H. Brune, G. Ertl, and R. J. Behm. Scanning tunneling microscopy observations on the reconstructed Au(111) surface: Atomic structure, long-range superstructure, rotational domains, and surface defects. *Phys. Rev. B*, 42:9307–9318, 1990.

[99] W. Chen, V. Madhavan, T. Jamneala, and M. F. Crommie. Scanning tunneling microscopy observation of an electronic superlattice at the surface of clean gold. *Phys. Rev. Lett.*, 80:1469–1472, 1998.

[100] M. J. Comstock, Jongweon Cho, A. Kirakosian, and M. F. Crommie. Manipulation of azobenzene molecules on Au(111) using scanning tunneling microscopy. *Phys. Rev. B*, 72:153414, 2005.

[101] Jiutao Li, Wolf-Dieter Schneider, and Richard Berndt. Local density of states from spectroscopic scanning-tunneling-microscope images: Ag(111). *Phys. Rev. B*, 56:7656–7659, 1997.

[102] Y. Pennec, W. Auwärter, A. Schiffrin, A. Weber-Bargioni, A. Riemann, and J. V. Barth. Supramolecular gratings for tuneable confinement of electrons on metal surfaces. *Nat. Nano.*, 2:99–103, 2007.

[103] M. F. Crommie, C. P. Lutz, and D. M. Eigler. Imaging standing waves in a two-dimensional electron gas. *Nature*, 363:524–527, 1993.

[104] Roland Fitzner, Chris Elschner, Matthias Weil, Christian Uhrich, Christian Körner, Moritz Riede, Karl Leo, Martin Pfeiffer, Egon Reinold, Elena Mena-Osteritz, and Peter Bäuerle. Interrelation between crystal packing and small-molecule organic solar cell performance. *Advanced Materials*, 24(5):675–680, 2012.

[105] Roland Fitzner, Elena Mena-Osteritz, Amaresh Mishra, Gisela Schulz, Egon Reinold, Matthias Weil, Christian Körner, Hannah Ziehlke, Chris Elschner, Karl Leo, Moritz Riede, Martin Pfeiffer, Christian Uhrich, and Peter Bäuerle. Correlation of π-conjugated oligomer structure with film morphology and

organic solar cell performance. *Journal of the American Chemical Society*, 134(27):11064–11067, 2012.

[106] Amaresh Mishra and Peter Bäuerle. Small molecule organic semiconductors on the move: promises for future solar energy technology. *Angewandte Chemie International Edition*, 51(9):2020–2067, 2012.

[107] Fabian Mohn, Bruno Schuler, Leo Gross, and Gerhard Meyer. Different tips for high-resolution atomic force microscopy and scanning tunneling microscopy of single molecules. *Applied Physics Letters*, 102(7):073109, 2013.

[108] Nora Gonzalez-Lakunza, Marta E. Canas-Ventura, Pascal Ruffieux, Ralph Rieger, Klaus Müllen, Roman Fasel, and Andrés Arnau. Hydrogen-bonding fingerprints in electronic states of two-dimensional supramolecular assemblies. *ChemPhysChem*, 10(17):2943–2946, 2009.

[109] G. Schulze, K. J. Franke, A. Gagliardi, G. Romano, C. S. Lin, A. L. Rosa, T. A. Niehaus, Th. Frauenheim, A. Di Carlo, A. Pecchia, and J. I. Pascual. Resonant electron heating and molecular phonon cooling in single C_{60} junctions. *Phys. Rev. Lett.*, 100:136801, 2008.

[110] Sarah Maria Falke, Carlo Andrea Rozzi, Daniele Brida, Margherita Maiuri, Michele Amato, Ephraim Sommer, Antonietta De Sio, Angel Rubio, Giulio Cerullo, Elisa Molinari, and Christoph Lienau. Coherent ultrafast charge transfer in an organic photovoltaic blend. *Science*, 344(6187):1001–1005, 2014.

[111] Carlo Andrea Rozzi, Sarah Maria Falke, Nicola Spallanzani, Angel Rubio, Elisa Molinari, Daniele Brida, Margherita Maiuri, Giulio Cerullo, Heiko Schramm, Jens Christoffers, and Christoph Lienau. Quantum coherence controls the charge separation in a prototypical artificial light-harvesting system. *Nat. Commun.*, 4:1602, 2013.

[112] Alexander Riss, Sebastian Wickenburg, Patrick Gorman, Liang Z. Tan, Hsin-Zon Tsai, Dimas G. de Oteyza, Yen-Chia Chen, Aaron J. Bradley, Miguel M. Ugeda, Grisha Etkin, Steven G. Louie, Felix R. Fischer, and Michael F. Crommie. Local electronic and chemical structure of oligo-acetylene derivatives formed through radical cyclizations at a surface. *Nano Letters*, 14(5):2251–2255, 2014.

[113] N. Ogawa, G. Mikaelian, and W. Ho. Spatial variations in submolecular vibronic spectroscopy on a thin insulating film. *Phys. Rev. Lett.*, 98:166103, 2007.

[114] N. Liu, N. A. Pradhan, and W. Ho. Vibronic states in single molecules: C_{60} and C_{70} on ultrathin Al_2O_3 films. *The Journal of Chemical Physics*, 120(24):11371–11375, 2004.

[115] Nilay A. Pradhan, Ning Liu, and Wilson Ho. Vibronic spectroscopy of single C_{60} molecules and monolayers with the STM. *The Journal of Physical Chemistry B*, 109(17):8513–8518, 2005.

[116] Yongfeng Wang, Jörg Kröger, Richard Berndt, and Hao Tang. Molecular nanocrystals on ultrathin NaCl films on Au(111). *Journal of the American Chemical Society*, 132(36):12546–12547, 2010.

[117] Naoka Ohta, Ryuichi Arafune, Noriyuki Tsukahara, Maki Kawai, and Noriaki Takagi. Enhancement of inelastic electron tunneling conductance caused by electronic decoupling in iron phthalocyanine bilayer on Ag(111). *The Journal of Physical Chemistry C*, 117(42):21832–21837, 2013.

[118] Alexander Riss, Sebastian Wickenburg, Liang Z. Tan, Hsin-Zon Tsai, Youngkyou Kim, Jiong Lu, Aaron J. Bradley, Miguel M. Ugeda, Kacey L. Meaker, Kenji Watanabe, Takashi Taniguchi, Alex Zettl, Felix R. Fischer, Steven G. Louie, and Michael F. Crommie. Imaging and tuning molecular levels at the surface of a gated graphene device. *ACS Nano*, 8(6):5395–5401, 2014.

[119] Jascha Repp, Peter Liljeroth, and Gerhard Meyer. Coherent electron-nuclear coupling in oligothiophene molecular wires. *Nat. Phys.*, 6:975979, 2010.

[120] Greg Pawin, Kin L. Wong, Daeho Kim, Dezheng Sun, Ludwig Bartels, Sampyo Hong, Talat S. Rahman, Robert Carp, and Michael Marsella. A surface coordination network based on substrate-derived metal adatoms with local charge excess. *Angewandte Chemie International Edition*, 47(44):8442–8445, 2008.

[121] Ziliang Shi and Nian Lin. Porphyrin-based two-dimensional coordination kagome lattice self-assembled on a Au(111) surface. *Journal of the American Chemical Society*, 131(15):5376–5377, 2009.

[122] Jonas Björk, Manfred Matena, Matthew S. Dyer, Mihaela Enache, Jorge Lobo-Checa, Lutz H. Gade, Thomas A. Jung, Meike Stöhr, and Mats Persson. STM fingerprint of molecule-adatom interactions in a self-assembled metal-organic surface coordination network on Cu(111). *Phys. Chem. Chem. Phys.*, 12:8815–8821, 2010.

[123] Marisa N. Faraggi, Nan Jiang, Nora Gonzalez-Lakunza, Alexander Langner, Sebastian Stepanow, Klaus Kern, and Andres Arnau. Bonding and charge transfer in metal-organic coordination networks on Au(111) with strong acceptor molecules. *The Journal of Physical Chemistry C*, 116(46):24558–24565, 2012.

[124] Peter Maksymovych, Dan C. Sorescu, and John T. Yates. Gold-adatom-mediated bonding in self-assembled short-chain alkanethiolate species on the Au(111) surface. *Phys. Rev. Lett.*, 97:146103, Oct 2006.

[125] Stephen M. Driver, Tianfu Zhang, and David A. King. Massively cooperative adsorbate-induced surface restructuring and nanocluster formation. *Angewandte Chemie International Edition*, 46(5):700–703, 2007.

[126] Peter Maksymovych and John T. Yates. Au adatoms in self-assembly of benzenethiol on the Au(111) surface. *Journal of the American Chemical Society*, 130(24):7518–7519, 2008.

[127] Frédéric Rossel, Pierre Brodard, Frans Patthey, Neville V. Richardson, and Wolf-Dieter Schneider. Modified herringbone reconstruction on Au(111) induced by self-assembled Azure A islands. *Surf. Sci.*, 602(14):L115–L117, 2008.

[128] J. T. Sun, L. Gao, X. B. He, Z. H. Cheng, Z. T. Deng, X. Lin, H. Hu, S. X. Du, Feng Liu, and H.-J. Gao. Surface reconstruction transition of metals induced by molecular adsorption. *Phys. Rev. B*, 83:115419, Mar 2011.

[129] G. V. Nazin, X. H. Qiu, and W. Ho. Visualization and spectroscopy of a metal-molecule-metal bridge. *Science*, 302(5642):77–81, 2003.

[130] Jascha Repp, Gerhard Meyer, Sami Paavilainen, Fredrik E. Olsson, and Mats Persson. Imaging bond formation between a gold atom and pentacene on an insulating surface. *Science*, 312(5777):1196–1199, 2006.

[131] Peter Liljeroth, Ingmar Swart, Sami Paavilainen, Jascha Repp, and Gerhard Meyer. Single-molecule synthesis and characterization of metal-ligand complexes by low-temperature stm. *Nano Letters*, 10(7):2475–2479, 2010.

[132] Fabio Cicoira, Clara Santato, and Federico Rosei. Two-dimensional nanotemplates as surface cues for the controlled assembly of organic molecules. In Paolo Samorditor, *STM and AFM Studies on (Bio)molecular Systems: Unravelling the Nanoworld*, volume 285 of *Topics in Current Chemistry*, pages 203–267. Springer Berlin Heidelberg, 2008.

[133] Hailin Liang, Yang He, Yingchun Ye, Xiaoguang Xu, Fang Cheng, Wei Sun, Xiang Shao, Yongfeng Wang, Jianlong Li, and Kai Wu. Two-dimensional molecular porous networks constructed by surface assembling. *Coordination Chemistry Reviews*, 253(2324):2959–2979, 2009. Functional Hybrid Nanomaterials: Design, Synthesis, Structure, Properties and Applications.

[134] Sebastian Stepanow, Nian Lin, Dietmar Payer, Uta Schlickum, Florian Klappenberger, Giorgio Zoppellaro, Mario Ruben, Harald Brune, Johannes V. Barth, and Klaus Kern. Surface-assisted assembly of 2D metalorganic networks that exhibit unusual threefold coordination symmetry. *Angewandte Chemie International Edition*, 46(5):710–713, 2007.

[135] N. Henningsen, R. Rurali, C. Limbach, R. Drost, J. I. Pascual, and K. J. Franke. Site-dependent coordination bonding in self-assembled metal-organic networks. *The Journal of Physical Chemistry Letters*, 2(2):55–61, 2011.

[136] Tzu-Chun Tseng, Nasiba Abdurakhmanova, Sebastian Stepanow, and Klaus Kern. Hierarchical assembly and reticulation of two-dimensional Mn- and Ni-TCNQ$_x$ (x = 1, 2, 4) coordination structures on a metal surface. *J. Phys. Chem. C*, 115(20):10211–10217, 2011.

[137] Jun Liu, Tao Lin, Ziliang Shi, Fei Xia, Lei Dong, Pei Nian Liu, and Nian Lin. Structural transformation of two-dimensional meta-organic coordination networks driven by intrinsic in-plane compression. *Journal of the American Chemical Society*, 133(46):18760–18766, 2011.

[138] R. Yamachika, M. Grobis, A. Wachowiak, and M. F. Crommie. Controlled atomic doping of a single C$_{60}$ molecule. *Science*, 304(5668):281–284, 2004.

[139] Christian Wäckerlin, Cristian Iacovita, Dorota Chylarecka, Petra Fesser, Thomas A. Jung, and Nirmalya Ballav. Assembly of 2D ionic layers by reaction of alkali halides with the organic electrophile 7,7,8,8-tetracyano-p-quinodimethane (TCNQ). *Chem. Commun.*, 47:9146–9148, 2011.

[140] T R Umbach, I Fernández-Torrente, M Ruby, F Schulz, C Lotze, R Rurali, M Persson, JI Pascual, and KJ Franke. Atypical charge redistribution over a charge-transfer monolayer on a metal. *New Journal of Physics*, 15(8):083048, 2013.

[141] N. Gonzalez-Lakunza, I. Fernández-Torrente, K. J. Franke, N. Lorente, A. Arnau, and J. I. Pascual. Formation of dispersive hybrid bands at an organic-metal interface. *Phys. Rev. Lett.*, 100:156805, 2008.

[142] I. Fernández-Torrente, K. J. Franke, and J. I. Pascual. Vibrational kondo effect in pure organic charge-transfer assemblies. *Phys. Rev. Lett.*, 101:217203, 2008.

[143] T R Umbach, I Fernandez-Torrente, J N Ladenthin, J I Pascual, and K J Franke. Enhanced charge transfer in a monolayer of the organic charge transfer complex TTF-TNAP on Au(111). *Journal of Physics: Condensed Matter*, 24(35):354003, 2012.

[144] Ashleigh E. Baber, Stephen C. Jensen, Erin V. Iski, and E. Charles H. Sykes. Extraordinary atomic mobility of Au(111) at 80 kelvin: Effect of styrene adsorption. *Journal of the American Chemical Society*, 128(48):15384–15385, 2006.

[145] Ying Jiang, Qing Huan, Laura Fabris, Guillermo C. Bazan, and Wilson Ho. Submolecular control, spectroscopy and imaging of bond-selective chemistry in single functionalized molecules. *Nat. Chem.*, 5:36–41, 2013.

[146] Weihua Wang, Xingqiang Shi, Shiyong Wang, Jun Liu, Michel A. Van Hove, Pei Nian Liu, Rui-Qin Zhang, and Nian Lin. Cooperative modulation of electronic structures of aromatic molecules coupled to multiple metal contacts. *Phys. Rev. Lett.*, 110:046802, 2013.

[147] N. Knorr, H. Brune, M. Epple, A. Hirstein, M. A. Schneider, and K. Kern. Long-range adsorbate interactions mediated by a two-dimensional electron gas. *Phys. Rev. B*, 65:115420, 2002.

[148] S. Lukas, G. Witte, and Ch. Wöll. Novel mechanism for molecular self-assembly on metal substrates: Unidirectional rows of pentacene on Cu(110) produced by a substrate-mediated repulsion. *Phys. Rev. Lett.*, 88:028301, 2001.

[149] Fabien Silly, Marina Pivetta, Markus Ternes, Frans Patthey, Jonathan P. Pelz, and Wolf-Dieter Schneider. Creation of an atomic superlattice by immersing metallic adatoms in a two-dimensional electron sea. *Phys. Rev. Lett.*, 92:016101, 2004.

[150] Jascha Repp, Francesca Moresco, Gerhard Meyer, Karl-Heinz Rieder, Per Hyldgaard, and Mats Persson. Substrate mediated long-range oscillatory interaction between adatoms: Cu/Cu(111). *Phys. Rev. Lett.*, 85:2981–2984, 2000.

[151] Per Hyldgaard and Mats Persson. Long-ranged adsorbate-adsorbate interactions mediated by a surface-state band. *Journal of Physics: Condensed Matter*, 12(1):L13, 2000.

[152] Takashi Yokoyama, Tomonori Takahashi, Kazuteru Shinozaki, and Masakuni Okamoto. Quantitative analysis of long-range interactions between adsorbed dipolar molecules on cu(111). *Phys. Rev. Lett.*, 98:206102, 2007.

[153] Matthias Marschall, Joachim Reichert, Alexander Weber-Bargioni, Knud Seufert, Willi Auwärter, Svetlana Klyatskaya, Giorgio Zoppellaro, Mario Ruben, and Johannes V. Barth. Random two-dimensional string networks based on divergent coordination assembly. *Nat. Chem.*, 2:131–137, 2010.

[154] David Ecija, Saranyan Vijayaraghavan, Willi Auwärter, Sushobhan Joshi, Knud Seufert, Claudia Aurisicchio, Davide Bonifazi, and Johannes V. Barth. Two-dimensional short-range disordered crystalline networks from flexible molecular modules. *ACS Nano*, 6(5):4258–4265, 2012.

[155] G. Schull and R. Berndt. Orientationally ordered (7×7) superstructure of C_{60} on Au(111). *Phys. Rev. Lett.*, 99:226105, 2007.

[156] K. J. Franke, G. Schulze, N. Henningsen, I. Fernández-Torrente, J. I. Pascual, S. Zarwell, K. Rück-Braun, M. Cobian, and N. Lorente. Reducing the molecule-substrate coupling in C_{60}-based nanostructures by molecular interactions. *Phys. Rev. Lett.*, 100:036807, Jan 2008.

[157] Markus Lackinger, Stefan Griessl, Wolfgang M. Heckl, and Michael Hietschold. Coronene on Ag(111) investigated by LEED and STM in UHV. *The Journal of Physical Chemistry B*, 106(17):4482–4485, 2002.

[158] I. Fernández-Torrente, D. Kreikemeyer-Lorenzo, A. Stróżecka, K. J. Franke, and J. I. Pascual. Gating the charge state of single molecules by local electric fields. *Phys. Rev. Lett.*, 108:036801, 2012.

[159] H. L. Skriver and N. M. Rosengaard. Surface energy and work function of elemental metals. *Phys. Rev. B*, 46:7157–7168, 1992.

[160] D. M. Eigler and E. K. Schweizer. Positioning single atoms with a scanning tunnelling microscope. *Nature*, 344:524–526, 1990.

[161] D. M. Eigler, C. P. Lutz, and W. E. Rudge. An atomic switch realized with the scanning tunnelling microscope. *Nature*, 352:600–603, 1991.

[162] M. F. Crommie, C. P. Lutz, and D. M. Eigler. Confinement of electrons to quantum corrals on a metal surface. *Science*, 262(5131):218–220, 1993.

[163] A. J. Heinrich, C. P. Lutz, J. A. Gupta, and D. M. Eigler. Molecule cascades. *Science*, 298(5597):1381–1387, 2002.

[164] H. C. Manoharan, C. P. Lutz, and D. M. Eigler. Quantum mirages formed by coherent projection of electronic structure. *Nature*, 403:512–515, 2000.

[165] Saw-Wai Hla, Ludwig Bartels, Gerhard Meyer, and Karl-Heinz Rieder. Inducing all steps of a chemical reaction with the scanning tunneling microscope tip: Towards single molecule engineering. *Phys. Rev. Lett.*, 85:2777–2780, 2000.

[166] Phaedon Avouris. Manipulation of matter at the atomic and molecular levels. *Accounts of Chemical Research*, 28(3):95–102, 1995.

[167] T. A. Jung, R. R. Schlittler, J. K. Gimzewski, H. Tang, and C. Joachim. Controlled room-temperature positioning of individual molecules: Molecular flexure and motion. *Science*, 271(5246):181–184, 1996.

[168] James K. Gimzewski and Christian Joachim. Nanoscale science of single molecules using local probes. *Science*, 283(5408):1683–1688, 1999.

[169] L. Bartels, G. Meyer, and K.-H. Rieder. Basic steps of lateral manipulation of single atoms and diatomic clusters with a scanning tunneling microscope tip. *Phys. Rev. Lett.*, 79:697–700, Jul 1997.

[170] Hendrik Glowatzki, Benjamin Bröker, Ralf-Peter Blum, Oliver T. Hofmann, Antje Vollmer, Ralph Rieger, Klaus Müllen, Egbert Zojer, Jürgen P. Rabe, and Norbert Koch. "Soft" metallic contact to isolated C_{60} molecules. *Nano Letters*, 8(11):3825–3829, 2008.

[171] Dirk Kühne, Florian Klappenberger, Régis Decker, Uta Schlickum, Harald Brune, Svetlana Klyatskaya, Mario Ruben, and Johannes V. Barth. High-quality 2D metal-organic coordination network providing giant cavities within mesoscale domains. *Journal of the American Chemical Society*, 131(11):3881–3883, 2009.

[172] Steven L. Tait, Alexander Langner, Nian Lin, Rajadurai Chandrasekar, Olaf Fuhr, Mario Ruben, and Klaus Kern. Assembling isostructural metal-organic coordination architectures on Cu(100), Ag(100) and Ag(111) substrates. *ChemPhysChem*, 9(17):2495–2499, 2008.

[173] Thomas Classen, Guido Fratesi, Giovanni Costantini, Stefano Fabris, Frank Louis Stadler, Cheolkyu Kim, Stefano de Gironcoli, Stefano Baroni, and Klaus Kern. Templated growth of metal-organic coordination chains at surfaces. *Angewandte Chemie*, 117(38):6298–6301, 2005.

[174] Hermann Walch, Jürgen Dienstmaier, Georg Eder, Rico Gutzler, Stefan Schlögl, Thomas Sirtl, Kalpataru Das, Michael Schmittel, and Markus Lackinger. Extended two-dimensional metalorganic frameworks based on thiolate-copper coordination bonds. *Journal of the American Chemical Society*, 133(20):7909–7915, 2011.

[175] Lucia Vitali, Lucia Vitali, Robin Ohmann, Alessio Comisso, Alessandro De Vita, and Klaus Kern. Portrait of the potential barrier at metal-organic nanocontacts. *Nat. Mater.*, 9:320–323, 2010.

[176] Emily A. Lewis, Colin J. Murphy, Melissa L. Liriano, and E. Charles H. Sykes. Atomic-scale insight into the formation, mobility and reaction of ullmann coupling intermediates. *Chem. Commun.*, 50:1006–1008, 2014.

[177] Georgios Kyriakou, Matthew B. Boucher, April D. Jewell, Emily A. Lewis, Timothy J. Lawton, Ashleigh E. Baber, Heather L. Tierney, Maria Flytzani-Stephanopoulos, and E. Charles H. Sykes. Isolated metal atom geometries as a strategy for selective heterogeneous hydrogenations. *Science*, 335(6073):1209–1212, 2012.

[178] Leo Gross, Francesca Moresco, Letizia Savio, André Gourdon, Christian Joachim, and Karl-Heinz Rieder. Scattering of surface state electrons at large organic molecules. *Phys. Rev. Lett.*, 93:056103, 2004.

[179] E. J. Heller, M. F. Crommie, C. P. Lutz, and D. M. Eigler. Scattering and absorption of surface electron waves in quantum corrals. *Nature*, 369:464–466, 1994.

[180] F. Klappenberger, D. Kühne, W. Krenner, I. Silanes, A. Arnau, F. J. García de Abajo, S. Klyatskaya, M. Ruben, and J. V. Barth. Tunable quantum dot arrays formed from self-assembled metal-organic networks. *Phys. Rev. Lett.*, 106:026802, 2011.

[181] Marina Pivetta, Giulia E. Pacchioni, Uta Schlickum, Johannes V. Barth, and Harald Brune. Formation of fe cluster superlattice in a metal-organic quantum-box network. *Phys. Rev. Lett.*, 110:086102, 2013.

[182] Knud Seufert, Willi Auwärter, F. J. García de Abajo, David Ecija, Saranyan
      Vijayaraghavan, Sushobhan Joshi, and Johannes V. Barth. Controlled interac-
      tion of surface quantum-well electronic states. *Nano Letters*, 13(12):6130–6135,
      2013.

[183] R. W. Robinett. Visualizing the solutions for the circular infinite well in
      quantum and classical mechanics. *American Journal of Physics*, 64(4):440–
      446, 1996.

[184] Katsuhiko Ariga, Takashi Nakanishi, and Jonathan P. Hill. A paradigm shift
      in the field of molecular recognition at the air-water interface: from static to
      dynamic. *Soft Matter*, 2:465–477, 2006.

[185] Davide Bonifazi, Stefan Mohnani, and Anna Llanes-Pallas. Supramolecular
      chemistry at interfaces: Molecular recognition on nanopatterned porous sur-
      faces. *Chemistry-A European Journal*, 15(29):7004–7025, 2009.

[186] Roberto Otero, Frauke Hümmelink, Fernando Sato, Sergio B. Legoas, Peter
      Thostrup, Erik Laegsgaard, Ivan Stensgaard, Douglas S. Galvao, and Flem-
      ming Besenbacher. Lock-and-key effect in the surface diffusion of large organic
      molecules probed by STM. *Nat. Mater.*, 3:779, 2004.

[187] T. R. Umbach, M. Bernien, C. F. Hermanns, A. Krüger, V. Sessi, I. Fernandez-
      Torrente, P. Stoll, J. I. Pascual, K. J. Franke, and W. Kuch. Ferromagnetic
      coupling of mononuclear Fe centers in a self-assembled metal-organic network
      on Au(111). *Phys. Rev. Lett.*, 109:267207, 2012.

[188] Weihua Wang, Yuning Hong, Xingqiang Shi, Christian Minot, Michel A.
      Van Hove, Ben Zhong Tang, and Nian Lin. Inspecting metal-coordination-
      induced perturbation of molecular ligand orbitals at a submolecular resolution.
      The Journal of Physical Chemistry Letters, 1(15):2295–2298, 2010.

[189] Joost Jvan der Lit, Mark P. Boneschanscher, Daniël Vanmaekelbergh, Mari
      ljäs, Andreas Uppstu, Mikko Ervasti, Ari Harju, Peter Liljeroth, and Ingmar
      Swart. Suppression of electron-vibron coupling in graphene nanoribbons con-
      tacted via a single atom. *Nat. Commun.*, 4:2023, 2013.

[190] Gaël Reecht, Fabrice Scheurer, Virginie Speisser, Yannick J. Dappe, Fab-
      rice Mathevet, and Guillaume Schull. Electroluminescence of a polythiophene
      molecular wire suspended between a metallic surface and the tip of a scanning
      tunneling microscope. *Phys. Rev. Lett.*, 112:047403, 2014.

Acknowledgments

First of all, I would like to thank Prof. J. I. Pascual for giving me the opportunity to work in his group. He gave me a lot of help on both physics and life.

I also thank Prof. Wolfgang Kuch for agreeing to be my second supervisor.

I want to express my special thanks to Prof. Katharina Franke for her hosting me in the last two years and always being patient to any stupid questions from me.

A lot of thanks to the Chemists in AG Bäuerle in Ulm Universität. This work is impossible without their interesting molecules.

I also want to thank Dr. Roberto Robles from Campus UAB, Spain. He helps calculate the projected density of states in the Au/DCV5T-Me$_2$ complexes.

My thanks also go to Martina Corso for her motivation and help in the beginning of this work. I owe a lot to Christian Lotze, Michael Kleinert and Tobias Umbach. They resolved various problems in my computer and help me make a lot of boring phone-calls in German. I also want to thank my Chinese colleagues Jingcheng Li, Bo Chen and Xianwen Chen. I had the pleasure to chat with them in the daily life. I thank all the present and former members in AG Pascual and AG Franke for the great working atmosphere, the cakes, the barbeques and ....

Last but not least, I want to express all my gratitude to my parents and sisters for their supporting even with a separation of thousands of kilometers. I thanks all my friends and specially to Chenying. Without their accompanition, I can not survive in a foreign country.

It is gratefully acknowledged the financial support from the Chinese Scholarship Council.

Curriculum Vitae